



Minnesota State University, Mankato  
Cornerstone: A Collection of Scholarly  
and Creative Works for Minnesota  
State University, Mankato

---

All Graduate Theses, Dissertations, and Other  
Capstone Projects

Graduate Theses, Dissertations, and Other  
Capstone Projects

---

2016

## Early Detection of Mountain Pine Beetle Damage in Ponderosa Pine Forests of the Black Hills Using Hyperspectral and WorldView-2 Data

Kyle Edward Mullen  
*Minnesota State University, Mankato*

Follow this and additional works at: <https://cornerstone.lib.mnsu.edu/etds>



Part of the [Natural Resources and Conservation Commons](#), [Other Environmental Sciences Commons](#), and the [Remote Sensing Commons](#)

---

### Recommended Citation

Mullen, K. E. (2017). Early Detection of Mountain Pine Beetle Damage in Ponderosa Pine Forests of the Black Hills Using Hyperspectral and WorldView-2 Data [Master's thesis, Minnesota State University, Mankato]. Cornerstone: A Collection of Scholarly and Creative Works for Minnesota State University, Mankato. <https://cornerstone.lib.mnsu.edu/etds/665/>

This Thesis is brought to you for free and open access by the Graduate Theses, Dissertations, and Other Capstone Projects at Cornerstone: A Collection of Scholarly and Creative Works for Minnesota State University, Mankato. It has been accepted for inclusion in All Graduate Theses, Dissertations, and Other Capstone Projects by an authorized administrator of Cornerstone: A Collection of Scholarly and Creative Works for Minnesota State University, Mankato.

Early Detection of Mountain Pine Beetle Damage in Ponderosa Pine Forests of the Black Hills Using Hyperspectral and WorldView-2 Data

By

Kyle Mullen

A Thesis Submitted in Partial Fulfillment of the

Requirements for the Degree of

Master of Science

In

Geography

Minnesota State University, Mankato

Mankato, Minnesota

December 2016

November 21, 2016

Early Detection of Mountain Pine Beetle Damage in Ponderosa Pine Forests of the Black Hills Using Hyperspectral and WorldView-2 Data

Kyle Mullen

This thesis has been examined and approved by the following members of the student's committee.

---

Dr. Martin Mitchell

---

Dr. Fei Yuan

---

Dr. Christopher Ruhland

## **Abstract**

A leading cause for mortality in the pine forests of western North America, the mountain pine beetle, has impacted over 400,000 acres of ponderosa pine forest in the Black Hills of South Dakota since 1996. Methods aimed at earlier detection, prior to visual manifestation of a mountain pine beetle damage in the tree crown, have not been successful because of the overlap and variability of spectral response between the initial stages of attack (green-attacked) and non-attacked tree crowns. Needle-level reflectance spectra was measured from green-attack and non-attack ponderosa pine trees in early spring following an infestation and analyzed using a multi-statistical approach to determine which spectral features best discriminate green-attack needles. Green-attack reflectance was significantly higher than non-attack from 424-717 nm and 1151-2400 nm. Bands in the shortwave-infrared had increased measures of separation between classes compared to visible and near-infrared bands. Peaks in separation related to moisture absorption features, from 1451-1540 nm and 1973-2103 nm, and pigment absorption features from 462-520 nm and 663-689 nm, were consistently observed over multiple statistical analyses. While these features show promise for operational canopy-level detection, it is unknown if they can be scaled up due to large within-class variability and spectral overlap between classes.

To examine the potential for canopy-level detection, in-situ training data was collected for green-attack and non-attack trees from known locations within the Black Hills at a similar time a WorldView-2 image was acquired of the study area. Along with eight WV-2 bands, all possible normalized two-band indices were calculated to examine

the suitability of WV-2 data for detecting green-attack damage. The performance of three different classifiers, logistic regression, linear discriminant analysis, Random Forest, was evaluated. Normalized two-band indices using a combination of a near-infrared band and visible band increased separation compared to single WV-2 bands. Random Forest classifiers using the eight WV-2 bands as predictors yielded an independently validated accuracy of 70.6%. Compared to non-attack, green-attack class accuracies were lower, likely due to the high within-class variance and spectral overlap between classes observed. Even with these limitations, the methods presented offer improvements over existing green-attack detection methods.

## **Acknowledgments**

I would like to thank my advisor, Dr. Martin Mitchell, for encouraging me to pursue a degree in Geography and for his constant backing and enthusiasm. I would also like to thank my other committee members, Dr. Fei Yuan and Dr. Christopher Ruhland. Both of you have been integral to the positive experience I have had at MSU and I consider myself lucky to have such great mentors. I would also like to thank the faculty and staff of the Geography Department and my fellow graduate students for the friendly and supportive atmosphere they have fostered.

For their financial support during my time at MSU, I want to thank the James F. Goff Geography Graduate Research Endowment, the MSU College of Graduate Studies and Research, the Dr. Mary T. Dooley Map Library, the Creating a Strong and Vibrant Graduate Community Project, and the MSU Department of Geography.

I would like to thank my friends and family for their encouragement and support, especially my parents who have always been enthusiastic about my educational endeavors. Finally, I am extremely grateful for the support my wife has giving me during this process. Between sacrificing spring break to collect field data, putting up with my long nights, and countless hours helping me edit, her positivity, love, and support has been unwavering and true.

## TABLE OF CONTENTS

ABSTRACT.....	i
ACKNOWLEDGEMENTS.....	iii
LIST OF TABLES.....	viii
LIST OF FIGURES.....	ix
LIST OF ABBREVIATIONS.....	xii
INTRODUCTION.....	1
Problem Statement.....	1
Research Objectives.....	4
Study Site Selection.....	4
LITERATURE REVIEW.....	8
Introduction.....	8
Mountain Pine Beetle Epidemics.....	9
MPB Epidemics in Western North America and the Black Hills.....	9
Impacts of Infestations.....	10
Mountain Pine Beetle Biology.....	12
Life History.....	12
MPB Infestation Epidemiology.....	14
Factors Controlling Beetle Populations.....	14
Population Dynamics.....	16
Pine Host and Beetle Interaction.....	18
Host Colonization and Interaction.....	18
Pine Stand Susceptibility.....	20
Biophysical Response of Pine Crowns to MPB Attack.....	23
Mitigation, Detection and Remote Sensing MPB Infestations.....	24
Mitigation and Detection.....	24
Factors Influencing Remote Sensing Approaches.....	27
Spectral Response of Stressed Vegetation.....	28
Mountain Pine Beetle Detection and Mapping.....	31
Red Attack Detection.....	31
Green Attack Detection and Mapping.....	33

SPECTRAL CHARACTERISTICS OF GREEN-ATTACKED AND NON-ATTACKED PONDEROSA PINE NEEDLES USING HAND-HELD HYPERSPECTRAL MEASUREMENTS .....	38
Introduction .....	38
Methodology.....	39
Needle Collection.....	39
Spectral Measurements .....	41
Data Pre-Processing .....	43
Spectral Reflectance Curves .....	45
Statistical Analysis and Best Band Selection.....	46
Group Separation and Effect Size.....	47
Discriminant Analysis .....	49
Logistic Regression .....	51
Random Forest.....	53
Results .....	56
Spectral Reflectance Curves .....	56
Statistical Analysis and Best Band Selection.....	59
Group Differences and Effect Size .....	59
Discrimination Analysis .....	62
Logistic Regression .....	69
Random Forest Results .....	76
Discussion.....	79
Statistical Methods.....	80
Spectral Regions Separation for GA and NA Classes .....	81
Implication for Remote Sensing and Management.....	91
Summation.....	94
EARLY DETECTION OF MOUNTAIN PINE BEETLE ATTACKED TREES USIGN WORLDVIEW-2 IMAGERY AND FIELD DATA .....	96
Introduction .....	96
Study Site .....	99
Methods .....	100
Field Data Collection .....	100

WorldView-2 Image Processing and Segmentation .....	101
Sample Dataset.....	104
Spectral Predictor Variables .....	107
Variable Importance and Data Mining .....	108
Classification and Validation.....	110
Results .....	112
Spectral Reflectance Signatures .....	112
Variable Importance .....	113
Data Mining.....	118
Classification Accuracies .....	120
Cross-Validated Accuracies .....	120
Independent Validation Accuracies.....	121
Discussion .....	123
Spectral Response of GA and NA Trees .....	123
Variable Importance and Discriminating Ability .....	127
Classification Accuracies and Model Performance.....	128
Limitations.....	132
Summation .....	136
CONCLUSIONS.....	137
Final Thoughts .....	141
REFERENCES .....	142
APPENDIX A. HISTORIC WINTER MONTHLY LOWS FOR WEATHER .....	164
APPENDIX B. SHAPIRO-WILK TEST OF NORMALITY FOR EACH WV-27 SPECTRAL VARIABLE .....	167
APPENDIX C. CORRELATION COEFFICIENTS BETWEEN ALL 36 WV-2 SPECTRAL VARIABLES .....	169
APPENDIX D. CROSS-VALIDATION CLASSIFICATION ACCURACIES FOR EACH CLASSIFIER AND PREDICTOR VARIABLE GROUPING .....	175
APPENDIX E. CLASSIFICATION ACCURACIES TESTED USING AN INDEPENDENT DATASET FOR EACH CLASSIFIER AND PREDICTOR VARIABLE GROUPING .....	176

## List of Tables

Table 2.1. Average number of years between winter monthly lows below $-29^{\circ}\text{C}$ ( $-20^{\circ}\text{F}$ ). .....	15
Table 3.1. Descriptions of needle sampling locations. ....	40
Table 3.2. Wavebands selected by stepwise LDA method.....	64
Table 3.3. Band ranges with notable SWIR peaks in LDA accuracies.....	69
Table 3.4 VNIR and SWIR bands with 25 highest overall mean decreases in accuracies .....	78
Table 3.5. Summary of statistical analysis results .....	83-84
Table 4.1. WV-2 image acquisition specifications .....	103
Table 4.2. Spectral resolution of WV-2 bands. ....	103
Table 4.3. Groupings of predictor variables used for classification .....	110
Table 4.4. Predictor variables selected by the final stepwise LR final model separating GA and NA trees .....	119
Table 4.5. Predictor variables selected by stepwise LDA final model separating GA and NA trees .....	119

## List of Figures

Figure 1.1. Mountain Pine Beetle damage in Black Hills. ....	4
Figure 1.2. Location of Black Hills National Forest.....	6
Figure 2.1. MPB Infestations in the United States by counties reporting damage. ....	8
Figure 2.2. Mountain pine beetle image. ....	12
Figure 2.3. Ponderosa pine trunk cross-section with blue-staining. ....	19
Figure 2.4. Typical development of damage stages in pine trees. ....	23
Figure 3.1. Needle collection using extendable tree pruner.....	42
Figure 3.2. Pitch tubes indicating a successful MPB attack .....	42
Figure 3.3. Mountain Pine Beetle Infested Tree Identification on Ponderosa Pine Trees .....	42
Figure 3.4. Effects of three smoothing filter sizes on spectral curves. ....	45
Figure 3.5. Number of significant differences between smoothed spectra and raw data .....	46
Figure 3.6. Random Forest OOB estimation of error with increasing number of individual trees .....	54
Figure 3.7. Random Forest OOB estimation of error for mtry settings from 1 through 100.....	55
Figure 3.8 Mean reflectance spectra curves for GA and NA trees .....	60
Figure 3.9 Reflectance value differences between the mean GA and NA trees .....	61
Figure 3.10. Pearson's r effect size of differences between GA and NA reflectance values .....	63
Figure 3.11. Discriminant analysis structure coefficients for each band .....	67

Figure 3.12. Leave-one-out cross validation classification accuracies for per band linear discriminant analysis.....	68
Figure 3.13. Wald Chi-square values for per-band logistic regression analysis.....	71
Figure 3.14. LOOCV accuracies per waveband LR analysis .....	74
Figure 3.15. Logistic regression per waveband odds ratio .....	75
Figure 3.16. Random Forest out-of-bag estimation of mean decrease in accuracies .....	77
Figure 4.1. Study area and WorldView-2 image footprint. ....	102
Figure 4.2. Flowchart outlining methodology .....	100
Figure 4.3. Example of manual delineation of tree crowns .....	106
Figure 4.4. Mean reflectance values of NA and GA trees in each WV-2 band.....	112
Figure 4.5. Median reflectance values of NA and GA trees in each WV-2 band.....	113
Figure 4.6. GA and NA box-and-whisker plots for each WV-2 band .....	115
Figure 4.7. Pearson's r effect size of differences between GA and NA for WV-2 spectral variables .....	116
Figure 4.8. Per-variable logistic regression LOOCV accuracies .....	116
Figure 4.9. Linear discriminant analysis correlation structure coefficients for WV-2 spectral variables .....	117
Figure 4.10. MDA of spectral variables attributed by Random Forest classification of OOB sample .....	117

Figure 4.11. Cross-validated classification OA for each classifier and predictor variable grouping. ....	120
Figure 4.12. Independent dataset classification OA for each classifier and predictor variable grouping. ....	121
Figure 4.13. Independent dataset classification GA user's accuracies for each model and grouping of predictors. ....	124
Figure 4.14. Independent dataset classification GA producer's accuracies for each model and grouping of predictors. ....	124
Figure 4.15. Independent dataset classification NA user's accuracies for each model and grouping of predictors. ....	124
Figure 4.16. Independent dataset classification GA producer's accuracies for each model and grouping of predictors. ....	124
Figure 4.17. GA tree crowns (red) classified with the RF classifier using only WV-2 bands as predictors.....	133
Figure 4.18. GA tree crowns (red) classified with the LR classifier using all 36 WV-2 spectral variables as predictors.....	134
Figure 4.19. Google Earth™ imagery acquired 09/12/2015 with similar coverage to Figure 4.17 & 4.18 subsets.....	135

## Abbreviations

ASD – Analytical Spectral Devices

dbh – Diameter at Breast Height

DN – Digital Number

GA – Green-Attacked

LDA – Linear Discriminant Analysis

LR – Logistic Regression

MPB – Mountain Pine Beetle

NA – Non-Attacked

NIR – Near-Infrared

RA – Red-Attacked

RF – Random Forest

SD – South Dakota

SWIR – Short-Wave Infrared

U.S. – United States

USDA – United States Department of Agriculture

VNIR – Visible and Near-Infrared

WV-2 – WorldView-2

## **1. Introduction**

### **1.1 Problem Statement**

The mountain pine beetle (*Dendroctonus ponderosae*) is a leading cause of tree mortality in pine forests in western North America. Epidemics in South Dakota's Black Hills region have infested over 400,000 acres of ponderosa pine forest since 1996, which accounts for almost one-third of the Black Hills forested area (Graham et al. 2016). The catalyst for the current outbreak has been warmer winter conditions related to climate change and favorable forest stocking conditions due to historic forest management strategies (Raffa et al. 2008). At epidemic infestation levels, the mountain pine beetle (MPB), can devastate large amounts of forest resources in a single outbreak. Visible damage in tree crowns, known as red-attack (RA) damage, has been mapped using various remote sensing platforms such as Landsat, SPOT, IKONOS, and QuickBird (Rencz and Nemeth 1985; Franklin et al. 2003; Skakun et al. 2003; Coops et al. 2006; White et al. 2006; Dennison et al. 2010). However, visible clues of damage in tree crowns do not onset until after the new brood has emerged and taken flight (Wulder et al. 2006). Early detection of mountain pine beetle (MPB) non-visual damage, referred to as green-attack (GA) damage, would potentially allow forest managers to more effectively reduce the extent of infestations and save resources and valuable timber stands.

Early research focused on GA stage examined spectral bands in the visible and near infrared (NIR) regions of the spectrum and found significant differences between reflectance of GA and non-attacked (NA) trees in the green, red, red edge, and (NIR)

bands (Ahern 1988; Murtha and Wiart 1989; Heath 2001). Even though narrow wavelengths have been identified as sensitive to biophysical changes in GA needles, methods for detecting GA damage have been unsuccessful due to overlap and high variability in spectral signals between GA and NA trees and technological limitations of available sensors (Heath 2001; Sharma 2007; Cheng et al. 2010; Fassnacht et al. 2014; Niemann et al. 2015). An additional hindrance to accurate GA detection is that GA trees usually occur in small patches or as single trees increasing the chance that background elements will occur within the same pixel as GA trees causing their spectral response to be suppressed, especially in higher spatial resolution datasets (Wulder et al. 2009). To date, GA research has relied on data acquisition dates in the late summer to fall following the initial attack, to provide ample time for implementing mitigation strategies. However, the onset of MPB damage between initial attacks and late summer/early fall image acquisition dates may limit the ability to spectrally separate GA from NA trees and reduce classification accuracies. Later acquisition dates would allow for the onset of more severe stress in attacked trees and accentuate spectral differences between damage classes, thus potentially leading to more accurate detection.

Recent advancements in remote sensing technology may provide the means to overcome problems associated with GA detection. As sensors improve, there is a need to better understand how to utilize their unique spectral characteristics in the detection of GA beetle damage. For example, airborne or satellite spectral measurements have been traditionally limited to the visible and NIR spectral regions, but some of the newer sensing systems provide the means to measure a much broader range spectrum, including

channels in the shortwave infrared region (SWIR), which shows promise in the detection of GA moisture damage (Chang et al. 2010; Fassnacht et al 2014; Niemann et al 2015). In addition, analysis of needle-level hyperspectral datasets can be used to determine which spectral regions are most sensitive to biophysical changes in GA damage foliage and potentially provide insight as to which: (1) remote sensing systems are most suitable for GA mapping, and (2) which bands can be utilized to achieve more accurate results. Recent generations of satellite platforms have been fitted with sensors with multiple infrared bands, which could provide useful information for detecting moisture stress of attacked trees. One of these sensors occurs with the WorldView-2 (WV-2) satellite operated by Digital Globe® and offers high spatial and unique spectral capabilities that may successfully detect GA trees. Immtizer and Atzberger (2014) used WV-2 images to detect early stages of damage due to bark beetles in Norway spruce, classifying GA damage with a 76% overall accuracy. Currently, there is no known research utilizing WV-2 data to detect and map GA trees associated with MPB attacks in North America (Carter 1994).

This research aims to determine which spectral bands that best differentiate GA and non-attacked (NA) trees during the late winter/early spring following the initial attack and develop methods to improve GA detection. If successful, the results will provide insight in the management of remote sensing technologies specific to the GA problem and potentially a novel method for earlier detection of infestations. This will allow forest managers to more accurately target mitigation efforts in locations where GA

damage is more likely, saving both time and labor resources. Currently, research utilizing WV-2 imagery to detect and map GA trees within North America remains lacking.

## 1.2 Research Objectives

This study has three main research objectives: (1) Characterize the spectral response of NA and GA trees in the late winter/early spring following initial MPB attacks using field hyperspectral and WV-2 sensing systems; (2) Determine which spectral variables best separate GA and NA tree classes and; (3) Use GIS, statistical modeling, and spatial modeling to predict and map GA trees.

## 1.3 Study Site Selection

The Black Hills area provides a unique and ideal site for this study. Even though many areas in the Western U.S. have experienced MPB infestations, the Black Hills region is one of few that have a widespread MPB epidemic in progress. The current MPB



Figure 1.1. Mountain Pine Beetle damage in Black Hills. Side by Side comparison of damage due to MPB infestations near Harney Peak and the Black Elk Wilderness area in the Black Hills from 2004-2014. Photo courtesy of Ken Marchand, GIS Coordinator, Black Hills National Forest.

epidemic in this area initially manifested around 1996 and has since affected more than 400,000 acres of National Forest Service land (Graham et al. 2016). During this epidemic MPB infestations have damaged or killed large patches of trees, many of which are in popular recreational areas (Figure 1.1).

The Black Hills area is primarily located in southwestern South Dakota with portions in eastern Wyoming (Figure 1.2) and encompasses about 6,000 square miles. Regional uplift during volcanic activity several millions years ago have given the Black Hills unique topographic characteristics that differentiate it from the plains in the surrounding regional area. Volcanic uplift has given the central regions of the Black Hills a granitic Crystalline Core, which is surrounded by steep sedimentary deposits that were uplifted during the mountain building event. Elevation ranges from 975-2207 m going from east to west. The uplift of the Black Hills also influences the temperatures which differ from the surrounding plains area, generally producing lower temperatures with increasing elevation.

Summer mean high temperatures range from 24-26° C (75-79°F) and 29-32° C (84-90° F) and January mean lows range from -16 to -12° C (3-10°F) and -12 to -10°C (10-14°F) for the higher elevations to the lower plains respectfully. Due to orographic effects caused by the uplift, the Black Hills has greater precipitation than the surrounding plains, with an annual precipitation gradient of 77.5 cm (30.5 in) in the northwest hills (Lead, SD) to 44.7 cm (17.6 in) in the southeastern portion (Custer, SD). A majority of the precipitation falls in May through July. However, there is high inter-annual variability in precipitation during the wettest months, with coefficients of variation ranging from

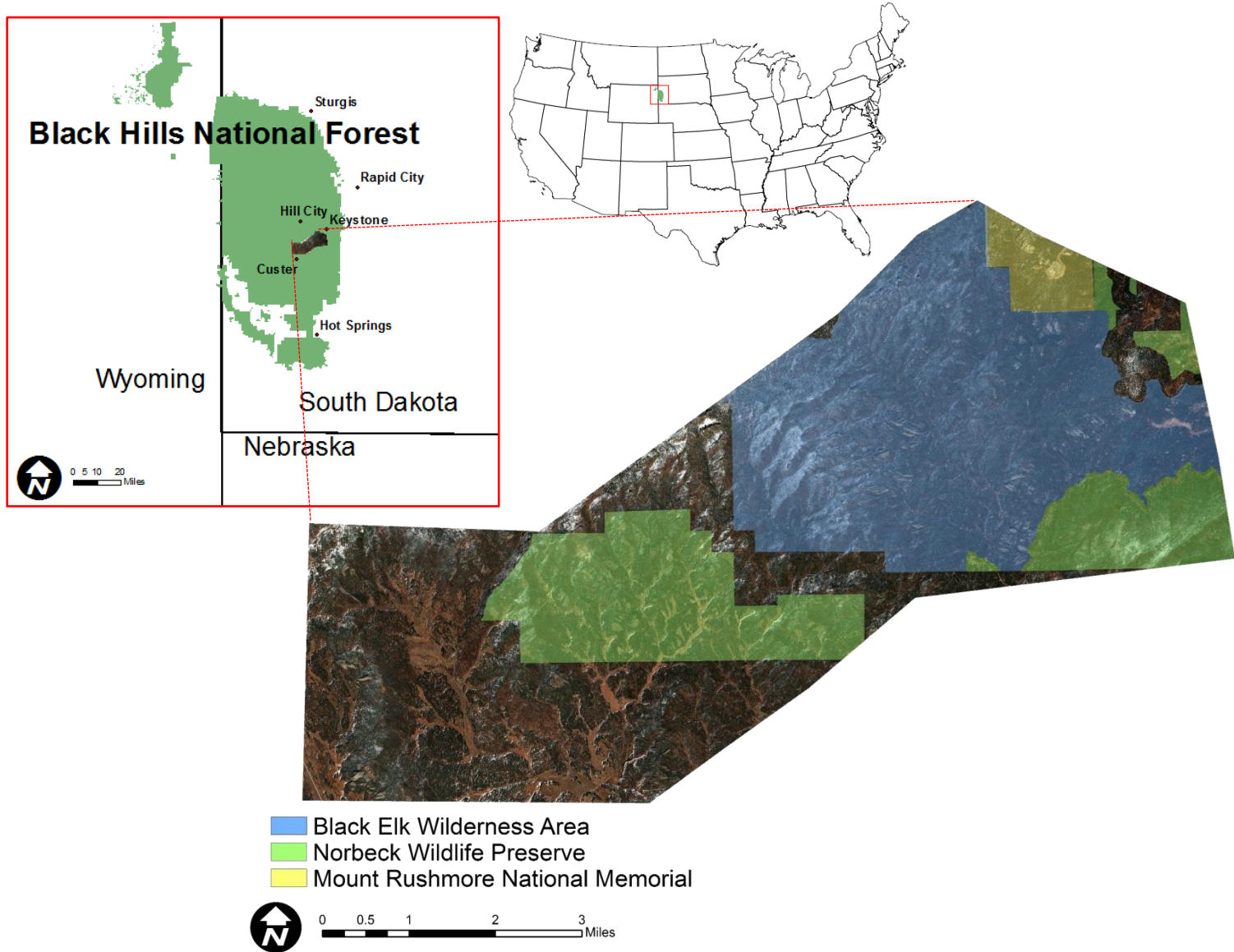


Figure 1.2. Location of Black Hills National Forest. Pansharpener WV-2 image (5,3,2 RGB) of the study area with transparent administrative boundaries overlaid for reference. Inserts provide WV-2 footprint and regional context of the study area.

0.51-0.58 and 0.57-0.70 for the southeastern (Custer) and northwestern (Lead) portions of the Black Hills (Dr. Martin Mitchell, personal communication, October 2016).

Successions of multiple years below annual averages can accentuate tree stress due to competition in high density stands, which along with warmer winter temperatures, increases the susceptibility of the Black Hills to MPB epidemics (Dr. Martin Mitchell, personal communication, October 2016).

The Black Hills forests have an extensive history of commercial use and nearly all of the forest has been cut at some point in its history (Graham et al. 2016). Early surveys in the late 1800's by General Custer and Henry Graves noted the Black Hills possessed great potential as a timber resource (Ludlow 1875; Graves 1899). Until the passing of *Forest Reserve Act of 1897*, unregulated logging associated with gold mining booms, had removed a majority of the old-growth, high value timber (Freeman 2014). Since 1897, the forest has undergone intensive management practices to develop the Black Hills as a timber resource (Freeman 2014). Management strategies such as strict fire suppression and ponderosa pines prolific regeneration abilities following disturbances led to the high density stands that fostered favorable conditions for the current MPB epidemic (Graham et al. 2016). Within the Black Hills region there are multiple stakeholders and government entities that manage the MPB epidemic and employ different mitigation strategies including: United States National Forest Service, Wind Cave National Park, Black Elk Wilderness Area, Mt. Rushmore National Monument, Custer State Park, and private land owners.

## 2. Literature Review

### 2.1 Introduction

The MPB is the most destructive of the bark beetles (Furniss and Carolin 1977) and is a native insect to forested regions of western North America, ranging from Mexico to British Columbia, Canada (Safranyik and Carroll 2006). In recent years, numerous epidemics have caused widespread forest damage (Figure 2.1).

These outbreaks have been attributed to climate change, most notably warmer winters resulting in fewer days below beetle mortality thresholds, and past forest management policies resulting in high density stands that comprise favorable habitat for the MPB (Raffa et al. 2008; Graham et al. 2016). Mitigation measures are necessary to reduce populations below epidemic levels and prevent future outbreaks. Effective management strategies rely on the forest managers connecting proper mitigation strategies to the nature of an outbreak. Detection, mapping, and monitoring the spatial and temporal characteristics of an outbreak are critical for making these connections. Remote sensing offers potentially novel ways to detect MPB infestations earlier. However it is necessary to choose the appropriate remote sensing data, processing techniques, and analysis methods relative to MPB life cycles, epidemiology of an infestation, beetle-host interactions, and the variations of these variables due to local conditions. To better

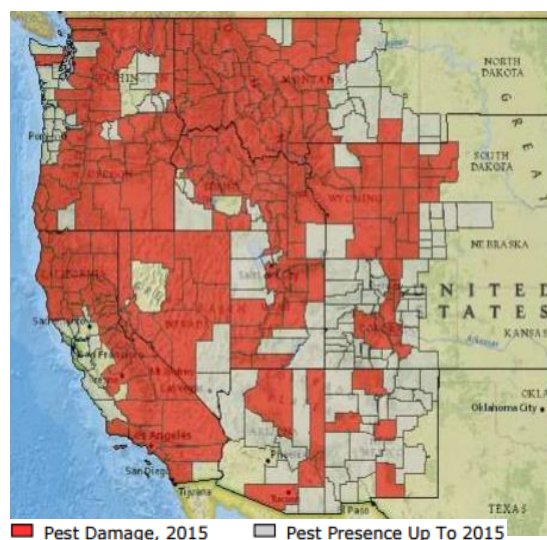


Figure 2.1. MPB Infestations in the United States by counties reporting damage. Image source: USDA Forest Service, Forest Health Protection and its partners (2016).

understand the numerous factors that influence remote sensing detection this review will: (1) provide a biological context for MPB life history, beetle-host interactions, and MPB epidemiology, (2) look at factors effecting population dynamics, (3) provide a review of remote sensing and MPB detection, and (4) review the types of statistical approaches potentially useful for determining which predictor variables best separated and detect vegetation stress.

## **2.2 Mountain Pine Beetle Epidemics**

### **2.1.1 MPB Epidemics in Western North America and the Black Hills**

Historically MPB epidemics have been a regular occurrence in the conifer forests of Western North America. The current epidemic started around the mid- to late '90s and is the largest recorded epidemic in terms of spatial extent, intensity, and its impacts to the environment and the economy, damaging approximately 50.5 million acres of forest in the Western U.S. since 1997 (USDA Forest Service Forest Health Protection 2016). In Canada the MPB has destroyed nearly 50% of all commercial lodgepole pine in British Columbia and has migrated far outside of its historic range into the boreal forest of North-Central Alberta (Natural Resources Canada 2016).

While MPB epidemic in the Black Hills accounts for a relatively small portion of the total acres infested in the United States, it is noted for its intensity and damage relative to the size of the forest. As of 2012 the current MPB epidemic had infested over 400,000 acres, which accounts for just over one-quarter of the entire ponderosa pine stock in the Black Hills. The current epidemic started from 1996-2000 with small

infestations in the northern portions of the Black Hills, south of Sturgis, South Dakota (Graham et al. 2016). By the peak year in 2012, infestations had reached nearly all parts of the Black Hills National Forest except the grassland southern regions, with the heaviest concentrations in the North-Central region and the slopes adjacent to Harney Peak (Graham et al. 2016). While the current infestation is concerning due to the severity, it is not the first occurrence of MPB epidemics in the Black Hills area. Some of the earliest anecdotal evidence of MPB damage in the Black Hills was noted during General Custer's expedition of the area in 1874 (Ludlow 1875), however the first record of an epidemic in the areas was in 1895 (Blackman 1931 as cited by Graham et al. 2016). Since then there have been numerous cycles of endemic and epidemic MPB populations with major epidemic events from 1895-1908, 1968-1981, and the current outbreak and lesser epidemics from 1936-1944, 1946-1945, and 1963-1966 (Graham et al. 2016).

### **2.1.2 Impacts of Infestations**

Negative commercial impacts of MPB infestations include losses in timber sales, manufacturing related to the timber industry, and government revenues from logging contracts and recreation (Abbot et al. 2008). Furthermore, beetle infestations change the management response of forest managers and force sometimes limited resources to be aliquoted away from other needs (Sims et al. 2010). A less obvious impact, but one that is of major concern to forest officials, is the safety hazard infested trees place on the public because extensive stands of dead trees (1) accentuate the fire hazard and (2) are prone to falling down during windy conditions. In some infested areas the US Forest Service

estimates that over a 100,000 trees killed by the MPB fell per day in the years following the peak epidemic (USDA Forest Service 2011). The Forest Service also estimates that around 14,000 miles of roads and trails and 1,400 recreations sites are at risk of falling trees in the Western US interior (USDA Forest Service 2011).

Infestations can have numerous abiotic and biological impacts as well. As trees die off it reduces the amount of photosynthetic activity of a site and stands can go from being carbon sinks to carbon sources as dead litter following an attack decomposes or, as trees become incinerated during a wildfire (Hicke et al. 2012; Edburg et al. 2011; Hansen et al. 2015a). Infestations alter nitrogen cycling by increasing soil nitrogen and vegetation nitrogen in healthy vegetation (Edburg et al. 2011; Griffin et al. 2011; Keville et al. 2013). Increases in moisture and litter depth around dead trees change the soil microclimate (Griffin et al. 2011). MPB infestations can significantly change fuel-loadings and have been linked to increases in wildfire severity and frequency (Page and Jenkins 2007; Jenkins et al. 2014). Drop in moisture content of attacked needles and changes in needle chemistry increase the flammability of MPB attack stands and lower ignition temps (Jolly et al. 2011). The dry and still-attached needles of the red-attack stage provides more crown-fuel leading to hotter and more destructive crown type wildfires, while older infested stands have more ground-fuels (Page and Jenkins 2007; Klutsch et al. 2011; Jenkins et al. 2014; Hansen et al. 2015b).

Reductions in evapotranspiration in infested stands and reduced water uptake from dead trees impacts water cycling of the watershed, leading to increased runoff thus magnifying spring and summer flooding in localities with severe damage (Brown et al.

2014; Mikkelsen et al. 2013a; Bearup et al. 2014). Changes in mineral transportation, nutrient cycling, and flooding can negatively impact the habitat of vegetation and terrestrial, subterranean, aquatic, and/or human life. Infestations can impact wildlife both negatively and positively. Avian species and mammals that are cavity-nesting or forage on beetles see a positive response due to increased habitat, food, and refuge from predators (Saab et al. 2014). Meanwhile, canopy nesting and pine seed consuming wildlife are negatively affected following an attack (Saab et al. 2014). Infestations have been linked to localized contamination of drinking water supplies (Mikkelsen et al. 2013b).

## **2.2 Mountain Pine Beetle Biology**

### **2.2.1 Life History**

The MPB (Figure 2.2) is commonly referred to as bark beetles because they spend a majority of the life under the bark of host trees (Safranyik and Carroll 2006; Gibson et al. 2009). The MPB emerges and flies only during the adult stage otherwise all development and activity take place in the subcortical tissues of their host. New broods emerge



Figure 2.2. Mountain Pine Beetle Image. Actual size ranges from 1/8 to 1/3 inches (Leatherman et al. 2007).

and take flight to select new host trees from July to mid-August, with some variance due to ambient temperatures (Leatherman et al. 2007; Safranyik and Carroll 2006). Attacks are initiated by the females, who seek out suitable host trees and release aggregation

pheromones which attract additional beetles. After mating, females construct vertical tunnels, called egg galleries, in the phloem of the host to lay eggs. Larvae feed on the nutrients within the phloem by constructing feeding tunnels perpendicular to the egg galleries. Larvae overwinter in these tunnels and then develop through four instar larval phases. Transition to the pupae stage takes place in the spring months and development to the adult stage usually happens a couple of weeks before emergence, with variation in emergence times being highly dependent on temperature (Bentz et al. 1991; Safranyik and Carroll 2006).

Temperature plays an important role in beetle mortality, development, and ultimately the spread of infestations and onset of epidemics. Most commonly, the life cycle of the MPB is univoltine, a single generation per year, but life cycles in areas with colder ambient temperatures, higher latitudes and elevations, can become semivoltine, or two years per generation (Amman 1973; Safranyik 1978; Bentz et al. 1991). Bivoltinism, multiple generations per year, has been reported in a number of other bark beetle species (Hansen and Bentz 2003; Safranyik and Carroll 2006) and is a major concern due to climate change as beetles develop faster in warmer temperatures (Raffa et al. 2008; Bentz et al. 2010; Sambaraju et al. 2012). This could lead to larger populations and widespread epidemics.

## **2.2.2 MPB Infestation Epidemiology**

### **2.2.2.1 Factors Controlling Beetle Populations**

Temperature, specifically the temperature of tree phloem, is an important regulator of MPB population dynamics (Amman 1984). Many of the other factors, which will be discussed later in the review, that are correlated with MPB outbreaks and population dynamics are also related to phloem temperature. High mortality rates are only reached when temperatures drop below mortality thresholds for extended periods, which are needed to keep populations at endemic levels (Amman 1984; Bentz et al. 1991; Cole 1981). Air temperature mortality thresholds range from approximately  $-18^{\circ}$  to  $-40^{\circ}$  C ( $\sim 0^{\circ}$  to  $-40^{\circ}$  F); the lower temperatures of this range are needed to kill off later MPB larvae stages which produce and accumulate glycerol that acts as “anti-freeze” (Safranyik and Carroll 2006). In the Black Hills, winter temperatures of approximately  $-29^{\circ}$  C ( $-20^{\circ}$ F) result in significant overwinter kills of MPBs (Greg Brundage, personal communication, July 2011). In recent history, the number of December and January months with days below this threshold has declined in the Black Hills and is likely a contributor to the recent MPB epidemics (Appendix A). For example, in Custer, SD there has been zero January months with days below  $-29^{\circ}$  C since 1985 compared to 22 from 1943-1984. Data from four weather stations with long-term historical records in the Black Hills shows the number of years between December or January days with temperatures below  $-29^{\circ}$  C has increased considerably since 1985 compared to previous years (Table 2.1).

Location	Years	Years between Days Below -29°C (-20°F)		
		December	January	February
Custer	Post-1985	7.8	NA	4.0
	1943 -1984	1.9	1.9	4.2
Mt. Rushmore National Monument	Post-1985	15.5	NA	16.0
	1962 -1984	7.7	11.5	23.0
Lead	Post-1985	10.3	16.0	8.0
	1910 -1984	5.8	3.8	8.3
Pactola Dam	Post-1985	5.2	10.5	1.9
	1956-1984	4.1	2.2	5.8

Table 2.1. Average number of years between winter monthly lows below -29°C (-20°F). Not applicable (NA) indicate that there has been no days during those years in which the temperature was below the threshold. For example there have been zero days below -20°F in Custer since 1985. Data is from National Weather Service (NWS) stations at Custer, SD (NWS ID CUSS2), Mt. Rushmore National Monument (NWS ID RMNS2), Lead, SD (NWS ID LEAS2), and Pactola Dam (NWS ID RAPS2).

While the number of years between February days below this threshold has actually decreased, the impact on MPB mortality is lower than early winter months because beetles have accumulated more glycerol to help them survive cold temps (Safranyik and Carroll 2006).

In addition to mortality, temperature also controls the development rates of the MPB life stages. Bentz et al. (1991) examined the development of the MPB from egg to adult under various constant temperature conditions and found that the optimal temperature range for development was between 23°C (75°F) and 25°C (77°F). However, the optimal developmental temperatures were different for each of the life stages. This life history trait provides a significant advantage for the MPB when faced with varying temperatures. During periods of colder or warmer temperatures, depending on the life stage observed, the beetle will slow or speed up development relative to other life stages. This “catch-up” mechanism synchronizes the emergence for MPB across a landscape regardless of localized differences in temperatures. This synchronized

emergence during epidemics is important for the beetle to successfully carry out “mass-attacks” on large diameter trees but also limits the ability of the MPB to develop bivoltinism (Bentz et al. 2013). Bentz et al. (2013) found that genetic variability across large landscapes shows some differences in developmental rates with MPB populations in warmer climates developing faster than those in colder climates. However, there was not enough genetic variation to develop multiple generations within a year within the current MPB range.

### **2.2.2.2 Population Dynamics**

The MPB population exists in one of four population cycles: endemic, incipient-epidemic, epidemic, and post epidemic (Safranyik and Carroll 2006). Characteristics of these cycles have important implications for the strategies chosen for monitoring and managing outbreaks. Transition between these populations cycles depend on factors such as availability of suitable host trees, stand susceptibility factors, and favorable weather conditions for development and beetle mortality.

The endemic stage is characterized by low populations with attacks limited to small patches or single trees possessing smaller diameters than the stand average and/or large diameter trees that have been weakened by biotic or abiotic factors (Amman 1984; Wulder et al 2006; Safranyik and Carroll 2006). This results in low brood production, high mortality, and thus low populations. During this stage, MPB attacks can be beneficial and improve forest health through attacking and removing weakened unhealthy trees and decreasing inter-specific competition (Safranyik and Carroll 2006).

Populations can go from the endemic to the incipient-epidemic phase with multiple years of warmer winter temperatures and/or when host trees become more susceptible due to increased stress from drought, disease, and/or increased competition (Safranyik and Carroll 2006). The incipient-epidemic phase is defined by a population growth that allows for a successful mass-attack of large diameter, high quality host trees (Safranyik and Carroll 2006). Attacks are still limited to single trees or to clusters of trees within a stand, commonly in areas where moisture fluctuates greatly, disease is more common, and/or more solar radiation is reached (Wulder et al 2006; Safranyik and Carroll 2006).

As these patches coalesce and population densities increase, a shift to an epidemic stage occurs. The epidemic phase is characterized by large populations that are resilient to high mortality rates, and 2- to 8-fold growth rates within a generation (Safranyik and Carroll 2006). During epidemics beetles have the ability to carry out mass attacks on large diameter trees and quickly deplete a stand of these large high vigor trees, causing large amounts of annual damage (Safranyik and Carroll 2006). Spatial characteristics of epidemics include large patches of trees, usually at the landscape level, with progressively large annual increases in the number of trees attacked (Wulder et al 2006; Safranyik and Carroll 2006).

Populations enter a post-epidemic stage as population size decreases due to sustained temperatures below mortality thresholds, a reduction in suitable host trees, or abatement of other stress conditions such as drought (Amman 1984; Safranyik et al. 2002; Safranyik and Carroll 2006). Spatial characteristics of newly attacked trees are

similar to those of the endemic stage, but there are landscape level patches of dead or grey-attack trees (Wulder et al. 2006).

## **2.3 Pine Host and Beetle Interaction**

### **2.3.1 Host colonization and Interaction**

The MPB has been known to attack any type of pine tree in North American and some other species of conifers, but its most common hosts in the Western U.S are lodgepole, ponderosa, and whitebark pines (Gibson et al. 2009; Negron et al. 2008; Taylor et al. 2006). After emergence, dispersal of MPB tends to be short with a majority of new hosts selected within 30 m or less of the initial release point; however, there is a potential for long-range dispersal if beetles are caught in convection currents above the tree canopy (Safranyik et al. 1992). The initial attacking females' select suitable hosts based on numerous factors including tree diameter, odor attraction, and visual cues or interactions between all of these factors in a way that is not fully understood at this time (Safranyik and Carroll 2006). The MPB prefers to select large diameter trees because they generally have a thicker phloem, which provides more nutritional resources and room for egg production (Amman and Cole 1980), and thicker bark, which provides additional protection from predators, such as woodpeckers, and cold temperatures. (Safranyik et al. 2002).

There is a trade off with selecting large diameter trees. These trees tend to be the most vigorous trees and are better suited to defend against attacks. At the site of attack, trees secrete resins that immobilize and push/pitch the MPB out of the tree (Raffa and

Berryman 1983). The resins released by the tree contain chemicals, called monoterpenes, which can be lethal to bark beetles (Raffa and Smalley 1995).

The MPB is able to overcome the tree's defenses in two ways. First, the MPB simply overwhelms a tree's defensive capabilities by coordinating "mass attacks" with the release of aggregation pheromones that attract thousands of beetles to a single tree (Raffa and Berryman 1983). This is only common during epidemic stages where population densities are high enough to successfully carry out mass attacks on multiple trees (Safranyik and Carroll 2006).



Figure 2.3. Ponderosa Pine trunk cross-section with blue-staining.

The second method used to overcome the host tree's defenses stems from a synergistic relationship the beetle has with a blue stain fungus that is attached to the outside of the beetle (Ballard et al. 1984; Gibson et al. 2009). As the beetle bores into the tree, the fungus gets deposited and quickly penetrates the phloem and xylem (Figure 2.3). The fungus alters water flow and transpiration rates within the vascular tissues of the tree, which reduces the production and allocation

of resin to the attack site and the trees' ability "pitch-out" attackers (Ballard et al. 1984).

The fungus inhibits water transport from the roots to the canopy of the tree. This interruption is rapid, within 10 days of an infestation there is a significant decrease in transpiration in trees that have been attacked and a 60% drop by 2 months. The following year, attacked trees no longer transport water and there is no new foliage growth. Until recently, it was believed that the feeding on the phloem by MPB was the ultimate reason

for tree mortality but recent research suggest otherwise. Hubbard et al. (2013) found that the blue stain fungus is the primary cause for tree mortality in MPB infestations.

### **2.3.2 Pine Stand Susceptibility**

The probability of a MPB attack and tree mortality rates within tree stands has been significantly correlated with a number of different stand characteristics (Negron and Popp 2004; Taylor et al. 2006; Negron et al. 2008). High tree basal area, high stand densities, low growth rates, and low tree spacing within a stand influence the susceptibility of attack because they influence competition within a stand. Moisture availability decreases with higher competition, weakening the trees ability to produce the resins used to resist MPB attacks. Tree diameter at breast height (dbh), stand age, and growth rates have also been positively correlated with susceptibility. These factors represent the potential for trees to have thicker phloem tissue, which can support larger broods.

These thresholds are determined from studies that have correlated stand characteristics with tree mortality rates cause by MPB attacks. In ponderosa pine stands basal area, average dbh of trees, stand densities, number of levels of canopies, and tree spacing have all been correlated with increased tree mortality rates (Stevens et al. 1980; Schmid and Mata 1992; Negron and Popp 2004; Negron et al. 2008). Diameter at breast height (dbh) is the diameter of trees at 4.5 ft above their base and basal area is the total area of cross sections of trees in a given area. Early studies have found that ponderosa pine stands with an average dbh of 25.4 cm (10 in) or higher and basal areas of 34.4

m<sup>2</sup>/ha (148.9 ft<sup>2</sup>/ac) have significant increases to susceptibility of MPB attack (Stevens et al. 1980). Schmid and Mata (1992) studied basal area and MPB attacks in even-aged ponderosa stands in Black Hills region of South Dakota. Their results indicated that the basal area threshold for highly susceptibility stands was 27.8 m<sup>2</sup>/ha (121.1 ft<sup>2</sup>/ac), which Schmid and Mata (2005) later suggested lowering the threshold to 23.0 m<sup>2</sup>/ha (101.2 ft<sup>2</sup>/ac). They also found average spacing between trees was a more accurate indicator of susceptibility than basal area because spacing is a better indicator of inter-species competition. Using regression analysis, they determined what the average spacing of trees should be to create low, moderate, and high risk stands. This method provides a practical guide for managers by creating end points for thinning based on the desired susceptibility rating. Negrón et al. (2008) researched stand susceptibility to MPB attack in uneven-aged ponderosa stands in the Black Hills forest and found significant differences between infested and non-infested stands. When comparing infested and non-infested stands both with mean dbh >25.4 cm (10 in) the infested stands had significantly higher stand densities and higher basal areas. Their regression analysis indicated a basal area of 27.8 m<sup>2</sup>/ha (121.1 ft<sup>2</sup>/ac) in highly infested stands, which is similar to the results from Schmid and Mata (1992). These studies indicate that beetles will preferentially select larger diameter trees in stands and in the presence of similar diameter trees. Therefore, there is a positive relationship between stand density and susceptibility to MPB infestations.

Topography of a landscape plays an important role stand susceptibility to MPB infestations, with elevation and slope being of particular importance. Both elevation and

slope aspect can influence the phloem temperature, which in turn influences the mortality and development of beetles. Generally beetles attack stands on south facing slopes that receive more solar radiation (Nelson et al. 2007; Honey-Marie et al. 2011), whereas high elevations tend to be a limiting factor due to colder temperatures (Amman 1973; Safranyik and Carroll 2006). Amman (1973) found that mortality rates and declining populations increase with increasing elevations due to colder temperatures and development rates also slowed with semivoltinism (one generation/two years) developing at 2450 m (8038 ft) and strict semivoltinism at 2573 m (8441 ft). New infestations primarily occur in canyons and valleys before areas that are more open and lesser slope, specifically on southwestern aspects (facing the sun and windward) which are correlated with higher infestation rates (Nelson et al. 2007; Honey-Marie et al. 2011). Topographic features tend to be more influential in the initial phases of outbreaks when suitable stands are available, but not as significant later in epidemic when location of suitable host trees becomes more important in predicting infestation spreads (Chapman et al. 2012; Walter and Platt 2013). Relative to the Black Hills, the elevations mentioned by Amman (1973) are beyond the highest summit in the Black Hills, Harney Peak at 2207 m (7,242 ft), thus MPBs have one brood per year. The southwestern aspect argument by Nelson et al. (2007) and Honey-Marie et al. (2011) would occur on slopes with accentuated evapotranspiration rates in a region possessing strong fluctuations in inter-annual precipitation. During a dry period, southern exposures would magnify the stress on high density stands. Moreover, along the upper slopes of the crystalline cores (above 1828 m

or 6000 ft) the more suitable host trees, ponderosa pines, are dominant on south facing slopes, whereas white spruces will be more abundant on the north facing slopes.

### 2.3.3 Biophysical Response of Pine Crowns to MPB Attack

The biophysical changes in foliage following a successful MPB attack fall into three stages. The initial stage is commonly referred to as green attack (GA) and is characterized by non-visual stress, which lasts anywhere from about 6-10 months (Wulder et al 2006).

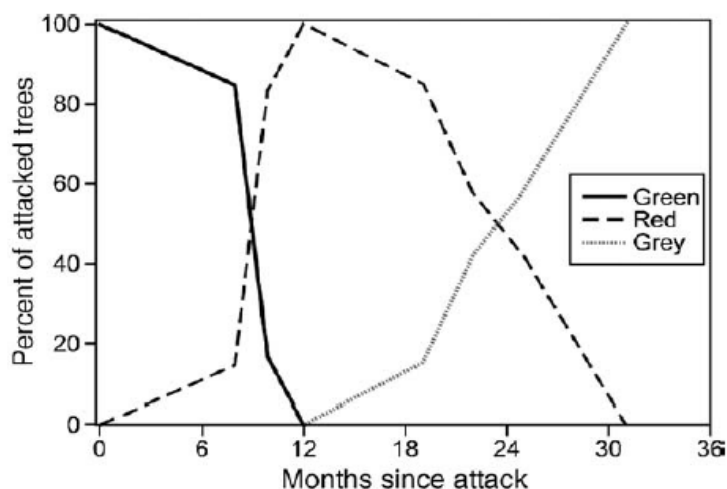


Figure 2.4. Typical development of damage stages in pine trees. Fading rates based on a stand composed of 15 MPB attacked lodgepole pine trees (Wulder, Dymond, White, Leckie, and Carroll 2006). MPB attacked ponderosa pines undergo a similar temporal sequence of stages

The fungus attack on the phloem of the tree causes a drop in the moisture content in the foliage but there is no visible damage in the color of the tree crown (Safranyik and Carroll 2006). After the initial attack, green chlorophyll pigments are lost, due to transpiration loss from the fungus infections, while simultaneously yellow carotenes and red anthocyanins pigments increase in the leaves (Hill et al. as cited in Wulder et al. 2006; Safranyik and Carroll 2006). This change is visible as attacked trees fade from green to yellow in the spring and is sometimes referred to as yellow attack or fading (Wulder et al. 2006). Yellow carotene pigments eventually begin to break down as well

and red anthocyanin concentrations increase in the leaves. This stage of attack, referred to as red-attack, reaches its peak approximately 12 months after the initial green-attack (Wulder et al. 2006). As plant stress continues due to the reduction in phloem functionality as a result of the fungal infection, needles start to desiccate and fall from the tree until host trees are completely defoliated, commonly called grey-attack, which occurs within three years after the initial attack (Wulder et al. 2006). Figure 2.4 illustrates a typical sequence of damage stages in lodgepole pine trees from initial infestation to the point that all attacked trees have lost needles (Grey Attack).

## **2.4 Mitigation, Detection, and Remote Sensing of MPB Infestations**

### **2.4.1 Mitigation and Detection**

Mitigating and managing MPB populations are broken into three main phases. First, direct control measures are used to reduce beetle populations directly and include strategies such as physically removing infested trees, applying insecticides to kill the beetles, or applying pheromones to attract or detract beetles to specific trees (Carroll et al. 2006; Gibson et al. 2009). Second, indirect controls are a type of preventative maintenance commonly applied during endemic MPB populations. These strategies aim to improve tree vigor by reducing stand susceptibility with the goal of reducing conditions that lead to outbreaks. An example would be pre-emptive thinning to reduce stand densities below the threshold of 23.0 m<sup>2</sup>/ha (101.2 ft<sup>2</sup>/ac). Lastly, detection and mapping includes all methods used to detect, map, and analyze the spread of MPB populations. This phase is important because it dictates how and where the control

measures are implemented, especially direct control measures. It can help forest managers coordinate ground labor efforts in a more cost effective and timely manner, choose appropriate control measures, and assess tree-mortality for timber supply forecasting and estimating stand susceptibility for future consideration (Wulder et al. 2006; Coops et al. 2008; Coggins et al. 2011). Coggins et al. (2011) studied the efficacy of direct control methods and found detection rates of nearly 80% are needed to successfully maintain a static MPB population when the expansion rates are high. The ability to mitigate and stabilize a MPB population depends on accurate detection rates.

Traditional methods for surveying MPB damage involved ground- and aerial-based methods. Ground surveys provide the most accurate and reliable information, especially for detecting GA damage. However, ground surveys have high operational and time costs, are limited in the extent they cover by labor costs and traversing mountainous terrain, and require precise placement of ground crews in locations where damage is most likely (Wulder et al. 2006; Coops et al. 2008). Aerial survey methods generally include observer sketch-mapping damage from an aerial platform, helicopter-GPS surveys, and manually digitizing aerial photographs. These methods provide general estimates of the amounts and locations of MPB damage over large areas, but are too inaccurate for precise operational activities because they rely on the subjectivity of the observer, do not allow for accuracy assessments, and commonly suffer from positional inaccuracies on maps (Wulder et al. 2006).

Furthermore, aerial based surveys are limited only to detection of visible RA damage from previous years MPB infestations. This does not allow forest managers to

mitigate the GA trees (current brood) and limits understanding about MPB patterns leading, which leads to less effective and more reactive mitigation instead of proactive strategies (Wulder et al. 2006).

Remotely sensed data sources from airborne and satellite sensors have been used increasingly in MPB research in recent history and provide a number of significant advantages over traditional surveying methods. Numerous platforms provide different spatial, spectral, and temporal options that can meet the various informational needs and variability in MPB outbreaks. Since imagery has higher positional accuracy, it creates the ability to combine images over time and space in an objective repeatable way. Being able to accurately compare images from different time periods provides insight about the spread of outbreaks. Automated classification reduces error due to subjectivity in observers' interpretations. Results can undergo accuracy assessments, which help with assessing the value of data for operational applications. Another advantage of remotely sensed data is the ability to combine it with ancillary data to provide more accurate detection results. This allows users to combine the spectral response of attacked trees with other data that might indicate stand susceptibility, such as forest inventories, digital elevation models, and precipitation maps, to create more accurate modeling and predictions of MPB attacks (Coops et al. 2006; White et al. 2006). Most importantly, remote sensing provides the ability for accurate detection and mapping across larger extents and inaccessible areas.

### 2.4.2 Factors Influencing Remote Sensing Approaches

Successfully detecting and mapping MPB damaged trees relies on the user selecting an appropriate remotely sensed data source to match the spatial, temporal, and spectral characteristics of damaged trees. Endemic MPB populations are characterized by single or small clusters of damaged trees, which require higher spatial resolution data sets to separate the response of attacked trees from surrounding healthy trees (Wulder, et al 2006). Likewise, if the MPB population occurs at an epidemic stage, moderate and low resolution might suffice to map widespread landscape level infestations where high resolution would be “over-kill”.

Temporal characteristics also play a role. The use of remote sensing to detect and map the later onset of RA damage has been the most researched and developed methods to date because the spectral response of red-attack trees is easily differentiated from the spectral response of healthy, non-attacked trees. Due to the difference in spectral responses between red-attack and healthy trees, moderate to low spectral resolution sensors can be effectively used for detection, mapping, and monitoring. The spatial distribution of RA trees also plays a role. Since the grey attack stage does not fully onset until year three following the initial attack, patches of RA trees may consist of multiple years of damage and are commonly found in larger patches which again make moderate spatial resolution imagery more appropriate.

Detection of earlier GA damage is highly sought after because it would allow forest managers to apply direct and indirect controls to infested and adjoining non-infested stands before a new brood emerges. However the spectral characteristics of GA

damage make it difficult to detect because attacked trees do not show any visual cues of attack and are spectrally similar to healthy trees (Wulder et al. 2006). Higher spectral resolution datasets are needed to detect the narrow regions within the spectrum that are responsive to pre-visual biophysical changes, such as reductions in moisture and chlorophyll concentrations, in the needles of MPB GA trees (Wulder et al. 2006). Narrow bands in the visible and infrared spectrum have been used previously to detect changes in moisture and chlorophyll content shortly after initial attack that could potentially maximize differences between GA trees and healthy trees (Ahern 1988, Cheng et al. 2010, Fassnacht et al. 2014). However, normal variability in moisture and chlorophyll content in healthy trees often overlaps with changes in GA trees, thus making it difficult to obtain high classification accuracies (Wulder et al. 2006). Furthermore, the age of needles, their position on the tree, background elements, and environmental differences between stands can influence spectral responses (Ahern 1988, Wulder et al. 2006). The spatial distribution of GA trees also influences which datasets maybe most useful for detection and mapping, as newly attacked trees are usually along the leading edges of an infestation and commonly consists of single or small patches of trees. These patches would require high spatial resolution imagery to separate from surrounding healthy trees.

### **2.4.3 Spectral Response of Stressed Vegetation**

The biophysical changes to pine trees following a MPB are similar to the stress responses observed in many species of plants, thus the changes in spectral response following a MPB attack are also similar. In the visible and red-edge range of the

spectrum vegetative spectral response to stress is primarily controlled by changes in plant pigments (Carter 1993; Filella and Penuelas 1994; Sims and Gamon 2002). The most important of these pigments is total chlorophyll (Chlorophyll *a* + Chlorophyll *b*) which primarily controls most of the solar absorption in the visible range (Sims and Gamon 2002; Blackburn 2007). Reflectance changes due to plant stress are more consistent in the visible spectrum and manifest earlier than other regions of the spectrum, especially in green-peak region from 530-580 nm and the red edge rise from 680-720 nm (Filella and Penuelas 1994; Curran et al. 1990; Carter 1993; Carter and Miller 1994; Lin et al. 2015). The most common red edge response to stress is a shift to the shorter wavelengths (blue shift) caused by increased reflectance at the base of the red, a shortening of the chlorophyll absorption feature in the red region, and a suppression in reflectance in the top of the rise (NIR shoulder) around 750 nm (Curran et al. 1990; Filella and Penuelas 1990). Correlations between reflectance and chlorophyll concentrations are greatest at approximately 700 nm-720 nm, followed by the green-peak around 550-600 nm (Carter 1993, Carter and Knapp 2001). In the visible spectrum, sensitivity to chlorophyll changes is lowest at wavelengths associated with higher absorption, primarily in the violet-blue and red regions and does not become manifest in these regions until severe damage occurs (Carter 2003, Carter and Knapp 2003). The secondary pigments carotenoids and anthocyanins sensitivity are greatest in the blue and green regions respectively (Gitelson et al. 2001, Gilesen et al. 2002, Ustin et al. 2009). Significant relationships between moisture content and reflectance have been observed in the visible range, but these are relatively minor compared to chlorophyll changes and do not onset until more advanced

stages of dehydration (Carter 1993, Foley et al. 2006; Zygielbaum et al. 2009; Zhang et al. 2012; Cao 2015). The influence of chlorophyll is not significant above 750 nm (Carter 1993).

Internal leaf structure and leaf moisture content govern NIR reflectance, especially near the NIR shoulder and plateau (750-900 nm). As plants become stressed and dehydrated leaves shrink and intercellular cavities reduce, cell walls degrade in the spongy mesophyll, and/or there is a reduction air to water interfaces leading to reduced reflection in the NIR (Ceccato et al. 2001; Ustin et al. 2012). Ceccato et al. (2001) found that leaf structure had the greatest influence on variations in reflectance values in the NIR and lower SWIR from approximately 700-1300 nm. While single wavelength reflectance is influenced primarily by internal leaf structure in the NIR, studies looking at water content and spectral derivative analysis have shown that moisture has the largest influence on changes in the slopes of absorption features at 970 nm and 1200 nm (Penuelas et al. 1993; Clevers et al. 2008; 2010).

Decreasing leaf moisture augments reflectance throughout the spectrum but sensitivity is greatest in the SWIR (Hunt and Rock 1989; Carter 1993; Fourty and Baret 1997; Sims and Gamon 2003; Foley et al. 2007; Zygielbaum et al. 2009; Clevers et al. 2010; Zhang et al. 2012; Cao 2015). Carter (1993) found plants suffering from moisture loss had significantly higher reflectance from 1119-2500 nm. Similar results have been observed in the SWIR reflectance of vegetation's under various stress conditions (Hunt and Rock 1989; Carter and Miller 1994; Foley et al. 2007; Cao et al. 2015). Attempts to estimate canopy moisture content have found the best spectral regions for detection are

weak absorption features in the SWIR (Fourty and Baret 1997; Sims and Gamon 2003). Others have noted that the SWIR alone is not enough for estimating moisture content in leaves because internal leaf structure changes can somewhat influence the SWIR reflectance as well and NIR measurements are needed to accurately estimate moisture (Aldakeheel and Danson 1997; Ceccato et al. 2001).

## **2.4.4 Mountain Pine Beetle Detection and Mapping**

### **2.4.4.1 Red Attack Detection**

To date, research into the use of remote sensing to map MPB outbreaks has focused on the detection of RA damage because the spectral response of RA trees is easily differentiated from the spectral response of healthy, non-attacked trees. Commonly found in patches that are the accumulation of multiple generations of beetle infestations, RA trees create large clusters of trees compared to GA damage, making moderate resolution imagery ( $\sim 5\text{-}30\text{ m}^2$ ), such as Landsat, sufficient for detection. Early work with Landsat imagery achieved accuracies above 90% but only for areas with very extensive and large clusters of red-attack trees, with much less accurate results in smaller patches (Rencz and Nemeth 1985). Franklin et al. (2003) further improved classification accuracies in smaller RA patches (73%) by stratifying single-date Landsat imagery based on forest composition and structure to obtain training data for a supervised classification method. Higher spatial resolution imagery, such as SPOT, achieved similar accuracies (71% RA producer's accuracy) using logistic regression models to map large patches of moderate to high RA damage in lodgepole pines. When detecting areas of high level RA

damage, it appears that higher spectral resolution datasets such as Landsat TM provide slight advantages over higher spatial resolution datasets such as SPOT. However, this advantage is vice versa when MPB damage is limited to smaller numbers of trees during early stages of outbreaks or post-epidemic stages. Temporal studies using Landsat imagery find the lowest accuracies during the earliest years of an outbreak, with improvements as areas get larger during the later stages of epidemics (Goodwin et al. 2008; Walter and Platt 2013). While a means for cataloging previous years MPB damage, moderate resolution imagery are not useful for mapping small clusters of RA trees or the current damage (GA trees), thus limiting them as a means for mitigating the problem.

Higher resolution datasets show significant improvements in mapping smaller groups of trees. White et al. (2005) used 4-m pixel IKONOS imagery to detect RA damage at accuracies ranging from 54% to 93% for low density to high density damage areas respectively. They also found that tree crowns smaller than 1.5 m were omitted from detection when co-located with other RA trees at distances greater than 11.3 m. This result has important implications towards GA detection. Since GA trees are more commonly found as small patches or single trees, datasets with higher spatial resolutions (< 4m) may be needed to avoid mixed pixel problems with smaller, isolated GA trees. Coops et al. (2006) used QuickBird imagery with four spectral bands (blue, green, red, NIR) and a 2.4m spatial resolution to map RA damage in lodgepole pines in British Columbia. They found that the green band provided the best separation between NA and RA trees followed by the NIR band. An intermediate fading stage was best discriminated using the blue band. A ratio of red to green bands provided the improved separation

between the NA and RA trees and the best classification accuracies using a binary classification methods based on thresholder values. Hicke and Logan (2009) also used Quickbird imagery and a maximum likelihood classification method to classify MPB RA damage in whitebark pines with low rates of commission and omission errors, 0.9% and 6.5% respectfully.

#### **2.4.4.2 Green Attack Detection and Mapping**

Multiple studies have attempted to characterize the spectral response of GA trees and/or classify GA damage using ground based spectroradiometer, aerial, and space-borne datasets (Murtha and Wiert 1989; Ahern 1989; Heath 2001; Sharma 2007; Cheng et al. 2010, Fassnacht et al. 2014; Niemann et al. 2015). Spectral overlap between healthy and GA trees, background elements, natural variance in reflectance, and variations in environmental conditions of stands have led to inconsistencies in results. Due to these limitations, classification and mapping of GA trees for directing pre-emptive mitigation efforts has not reached accuracies high enough to become operationally reliable. Historically GA detection research has focused on the visible and NIR portions of the spectra and the spectral responses driven by changes in leaf pigment concentrations. More recently sensors providing longer wavelengths bands have been used to examine the spectral response of damaged trees in the SWIR and moisture changes.

Murtha and Wiert (1989) provide an example of an early attempt to use aerial photography to detect GA damage. Using 1:2000 color infrared aerial photographs they extracted green, red, and NIR digital numbers (DN), along with calculating the ratios of

these DNs, from GA and NA lodgepole pines. ANOVA tests showed the DNs of GA pines were significantly higher than NA trees in the green and red regions of the spectrum. They speculated that differences in the green and red regions of GA trees likely resulted from increased reflectance associated with moisture loss in the foliage. Meanwhile, the lack of difference in the NIR might be caused by competing influence of changes in leaf structure causing initial drops in NIR reflectance and subsequent rises as foliage continues to dry out. Even though differences were observed for single trees, the authors concluded that large standard deviations and overlaps in these values would make any attempts to map GA trees on spectral values alone unsuccessful.

Several years later, Heath (2001) used visible-NIR hyperspectral imagery collected from a helicopter to examine GA and NA lodgepole pines. Bands that separated GA trees were primarily located in the blue and blue-green regions, with a couple additional bands in the red and NIR (Heath 2001). Heath used discriminant analysis to classify groups with an overall accuracy of 73%, but again noted considerable variability in healthy trees made detection problematic. Sharma (2007) used the satellite hyperspectral data to detect MPB GA damage in lodgepole pine in British Columbia. The researcher examined the spectral signatures of healthy and GA sites instead of individual trees. Using stepwise discriminant analysis Sharma identified that bands in the NIR (993-1094) were most important for GA discrimination and was able to separate GA and NA sites with an overall accuracy of 81% (Sharma 2007). More recent studies have focused on the use of airborne hyperspectral imagery. Fassnacht et al. (2014) classified various stages of MPB damage with overall accuracies from 76%-85% using HyMap imagery

and support vector machine classification. However accuracies for the GA damage class proved much lower with producers and users accuracies of 57% and 65% respectively, likely due to wide variances in the reflectance of healthy, GA, and fading tree crowns causing large overlaps in the spectral responses. In the same study these researchers used a genetic algorithm to identify spectral regions that best distinguished the damage classes and found the most frequent regions selected were in the green-peak (560 nm), red (680 nm), and red edge (690) portions of the spectrum (Fassnacht et al. 2014). Niemann et al. (2015) used a similar hyperspectral dataset to separate healthy, GA, and RA lodgepole pines, with emphasis on chlorophyll absorption features from 550-710 nm and water absorption features from 900-1000 nm and 1050-1285 nm. They observed two narrow windows exhibiting the greatest differences between healthy and GA from 650-685 nm with a slight blue shift of the red edge and significant but lesser separation from 1145-1210 nm. Using a spectral angle mapper classifier they achieved GA producers and users accuracies of 71.8%-95.0% and 63.4%-86.0%, respectively. Bands in the longer SWIR regions had little separation between GA and healthy samples (Niemann et al. 2015). Attempts to use multispectral imagery have been limited. Immitzer and Atzberger (2014) used 8-band multispectral WorldView-2 imagery to survey early bark beetle damage in European spruce trees and were able to achieve a top overall accuracy of 76% with GA producer's and user's accuracies of 72.7% and 71.5% respectively. They found that bands corresponding to the green, yellow, and red regions were most important for separating damage classes and bands in the violet, red edge, and NIR had large overlaps in variance.

Use of handheld spectroradiometer to measure the spectral response of healthy and GA trees either in the field or lab settings provides benefits that might allow it to better identify spectral regions sensitive to beetle induced stress. These instruments commonly measure the full spectrum, generally at narrower bandwidths than aerial or satellite based sensors, and decreases inconsistencies due to illumination angles, background interference, and atmospheric effects. While these benefits better capture subtle spectral changes, it has limitations in generalizing the results to operational use with existing remote sensing sensors. Ahern (1988) used lab spectroscopy to examine spectral changes in the visible and NIR driving by pigment changes in MPB attacked trees. He reported the greatest differences between GA and NA trees in the NIR shoulder from 730-760 nm with highly significant differences throughout the NIR plateau (730-1050 nm). Ahern also noted significant differences in the green-peak and significant red shift of the red edge for attacked trees. He concluded that bands in the green-peak, red edge, and NIR shoulder have the most potential for GA detection, with bands in the blue and red being insensitive to early damage. Carter and Knapp (2001) measured needle reflectance from clipped GA and healthy needles of loblolly pines attacked by southern pine beetles and the largest differences in the red edge followed by the green-peak. However their results differ from Ahern (1988) in that they observed a blue shift of the red edge and no significant differences in the NIR plateau. Similar research aimed at discriminating conifer species have also found that visible bands were better at separating species than NIR bands (Gong et al. 1997). In a more recent study Cheng et al. (2010) used lab spectroscopy to examine spectral responses of GA and NA trees across the full

spectrum. Unlike other studies that indicated pigment driven features in the visible spectrum as most sensitive damage, using continuous wavelet analysis and correlation analysis these researchers found water absorption features from 953-1390 nm were most sensitive to GA damage.

### **3. Spectral Characteristics of Green-Attacked and Non-Attacked Ponderosa Pine Needles Using Needle-Level Hyperspectral Measurements**

#### **3.1 Introduction**

Successful early detection of MPB damage in trees depends on being able to identify and utilized spectral features that are most sensitive to MPB induced tree stress. However it is difficult to differentiate within-species damage status because the spectral response differences between stressed and healthy plans can be subtle. The spectral resolution of a sensor must be very fine to capture these differences and classify disease stages at high enough accuracies to provide operationally useful information.

Spectroradiometers collect reflectance data that is characterized by many narrow bands and can potentially increase the ability to identify subtle features that are most responsive to plant stress. Better understanding of these features can guide the use of current and future generations of airborne and space-borne sensors for specific applications. With the high diversity of sensors with unique spectral capabilities currently available or planned for the near future, along with the development of more customized spectral sensors for aerial and unmanned aerial systems, it is important that users correctly select the sensor or data that matches the target application at interests.

A number of issues inherently arise with use of hyperspectral sensors. Large data volumes create problems with transferring, storing, and processing files. Moreover, many of the narrow wavebands contain the same information as other bands, thereby creating highly correlated variables that are problematic with statistical analysis. These issues create problems with discriminating between and classifying the GA and NA classes.

Research into the bands that are most sensitive to MPB damage and best separate classes may alleviate some of these issues by allowing an analyst to target specific bands that better distinguish groups and reduce the dimensionality of the data set, and consequently improve the processing time and classification accuracies.

Selecting which bands best discriminate two classes can be problematic due to the previously mentioned multicollinearity between variables in hyperspectral datasets, having a high number of predictor variables relative to the sample size, and non-parametric distributions of reflectance values. These characteristics can lower the robustness and reliability of statistical analysis. To obtain a more comprehensive understanding of which bands best discriminate the GA and NA groups in this research, a multifaceted statistical approach was utilized in this study. Due to the unique characteristics of hyperspectral dataset, no one statistical approach is completely appropriate. Using multiple statistical methods allows an analyst to utilize different advantages a particular method has to address some of these problematic characteristics. Moreover, redundancy in results between these methods can increase the confidence that a particular feature is important for discriminating the two classes.

## **3.2. Methodology**

### **3.2.1 Needle Collection**

Needle samples were collected from GA and NA ponderosa pine trees in the Black Hills National Forest from March 6-11, 2015. Table 3.1 provides a locational description of sampled tree sites. Samples were collected using an extendable tree pruner

Table 3.1. Descriptions of needle sampling locations. Samples were collected from GA and NA trees within the Black Hills National Forest, South Dakota from March 6-11, 2015.

<b>Sample Site Name</b>	<b>Approximate Lat/Long</b>	<b>PLSS Descriptions (South Dakota, Black Hills Meridian)</b>	<b>General Locational Description</b>
Glen Erin Creek	43.7365083, -103.5260811	-NW ¼ and NE ¼ of NE ¼ of S4 T4S R5E	4.25 mi SW of Custer, SD
Norbeck Wildlife Preserve – Iron Creek Trailhead	43.8339281, -103.4364705	-NE ¼ and SW ¼ of NW ¼ of S32 T2S R6E -NW ¼ of SW ¼ of S32 T2S R6E	3 mi SSE of Mt. Rushmore National Monument
Norbeck Wildlife Preserve – Iron Mountain Trailhead	43.8374118, -103.4414761	-SE ¼ of SE ¼ of S30 T2S R6E -NE ¼ of NE ¼ of S31 T2S R6E	2.7 mi SSE of Mt. Rushmore National Monument
Black Elk Wilderness – Centennial Trail	43.8684450, -103.5183491	-SE ¼ of S25 T2S R5E -SW ¼ and SE ¼ of NE ¼ of S25 T2S R5E	2.25 mi SSW of Mt. Rushmore National Monument
Sheridan Lake – South Shore Campground	43.9623061, -103.4886021	-SE ¼ and SW ¼ of NE ¼ of S14 T1S R5E -SE ¼ of S14 T1S R5E	2.25 mi NE of Hill City, SD
Sheridan Lake – Flume Trailhead	43.9660055, -103.4603963	-SE ¼ of NE ¼ of S13 T1S R5E -NE ¼ of NE ¼ of S13 T1S R5E	3.5 mi NE of Hill City, SD
Deerfield Lake – S Rochford Rd and N Shore Trailhead Rd	44.0316916, -103.8250379	-NW ¼ of S24 T1N R2E -NE ¼ and SE ¼ of SW ¼ of S24 T1N R2E -NW ¼ and SW ¼ of SE ¼ of S24 T1N R2E -NE ¼ of NW ¼ of S25 T1N R2E -NW ¼ of NE ¼ of S25 T1N R2E	14.25 mi NW of Hill City, SD
Deerfield Lake – National Forest Rd 188.1C	44.0316639, -103.7648683	-NW ¼ and SW ¼ of NE ¼ of S21 T1N R3E -SE ¼ of NW ¼ of S21 T1N R3E	12.25 mi NW of Hill City, SD
Deerfield Lake – S Rochford RD and National Forest Rd 190	44.0952739, -103.7775677	-NE ¼ of NE ¼ of S32 T2N R3E	3.5 mi SW of Rochford, SD

(Figure 3.1) with a maximum reach of approximately 7 m (23 ft). Stems were pruned from sun-light branches both of GA and NA trees to give enough fascicles to produce an optically thick bed of needles that light could not pass through. Green-attack trees were selected if they had no signs of fading in the visible crown and showed signs of a successful MPB attack indicated by the presence of multiple brownish-red pitch tubes around the circumference of the tree trunk (Figure 3.2 and 3.3). When possible, samples

were also collected from NA and GA trees within the same stand and/or vicinity. Needles were placed into labeled re-sealable polyethylene bags and packed into a cooler with ice to reduce dehydration after clipping and suppress changes in needle spectral reflectance (Foley et al. 2006). A total of 95 and 89 samples were collected for the GA and NA classes respectively. Spectral measurements were taken from samples within 16 hours of the initial clipping.

### **3.2.2 Spectral Measurements**

To obtain GA and NA needle reflectance spectra over the visible and near-infrared (VNIR) and shortwave-infrared spectral regions (325-2500nm), two spectroradiometers were used in this study. Reflectance spectra from 325 nm to 1002 nm were collected using Analytical Spectral Devices Inc (ASD) FieldSpec Pro® with a 1.4 nm sampling interval and total range of 325-1050 nm. Reflectance spectra from 1003-2500 nm were collected using an ASD SWIR1/SWIR2 QualitySpec Pro® with a 2nm sampling interval. In this study, data collected from the FieldSpec Pro® and QualitySpec Pro® will be referred to as the VNIR and SWIR datasets, respectively. Measurements were collected using an ASD Plant Probe accessory with a built-in halogen light source and a spot size of 10 mm. The Plant Probe was placed in direct contact with an optically thick bed of needles to prevent light from passing completely through the sample and reduce impact of external light. Measurements were taken inside a box painted with flat black paint in a room with no ambient light sources to reduce the risk of interference. Prior to spectral measurements and approximately every 20 minutes during use, an



Figure 3.1. Needle collection using extendable tree pruner. In the Norbeck Wildlife Reserve, Black Hills, SD, March 7, 2015.



Figure 3.2. Pitch tubes indicating a successful MPB attack. Reddish pitch tubes around more than one-third the circumference of a ponderosa pine tree in the Black Hills, SD, March 7, 2015.

### MOUNTAIN PINE BEETLE

#### INFESTED TREE IDENTIFICATION ON PONDEROSA PINE TREES

A ponderosa pine tree can be classified as infested if one or more of the following applies:

- Five or more brown/pink pitch tubes between 5ft. and 8ft. above ground level and spanning greater than 1/3 the circumference of tree.
- Brown boring dust in bark crevices and on the ground immediately adjacent to the tree base.
- Evidence of woodpecker feeding on trunk > 3 ft above ground. Patches of bark are removed and bark flakes lie on the ground or snow below tree. (Usually appearing around November or later.)

One of the most visible signs are popcorn-shaped masses of resin, called "pitch tubes," on the trunk where beetle tunneling begins. Pitch tubes may be brown, pink, or white.

White —unsuccessful attack at that point  
 Pink—usually unsuccessful attack at that point  
 Brown—successful attack at that point

Figure 3.3. Mountain Pine Beetle Infested Tree Identification on Ponderosa Pine Trees. Informational card published by the South Dakota Department of Agriculture illustrating the signs of a successful MPB attack on a ponderosa pine tree.

integration time optimization was performed to optimize the sensitivity of the instrument and a dark current measurement was taken to reduce the effects of instrument noise on sample measurements. Reflectance was standardized using a Spectralon® white reference panel prior to any measurements and after every 15-20 samples. Sample reflectance is determined using the following equation (Hatchell 1999):

$$\text{Sample Reflectance} = \frac{\text{Sample Signal} - \text{Dark Current}}{\text{White Reference Signal} - \text{Dark Current}}$$

A spectrum average was determined using 20 scans of each sample.

Spectroradiometer data was processed using the RS<sup>3</sup>® and Indico® software associated with each instrument and then was exported as ASCII text files for further use in other programs.

### 3.2.3 Data Pre-Processing

The raw reflectance spectra (1.4 nm and 2.0 nm bandwidths) were interpolated to give a working dataset with a 1 nm bandwidth. Due to spectral inconsistencies from low signal-to-noise ratios bands from 325-399 nm and 2401-2500 nm were excluded from analysis, giving a final combined dataset of 2000 bands from 400-2400 nm.

High spectral resolution data can be sensitive to noise due to the channels collecting from a small region of energy. This noise creates unwanted fluctuations in the spectra of the sample and can cause errors in further analysis. Noise can be dampened by applying a smoothing filter that modifies a data point by aggregating all of the data points that fall within the filter window. In this study a Savitky-Golay (SG) filter was used to reduce noise. The Savitky-Golay filter smooths a data mid-point by applying a

polynomial equation to the adjacent data points within the filter using a linear least squares method (Savitzky 1964). When smoothing spectra derived from vegetation the SG smoothing method has been shown to preserve the original data better than mean filters, which average all the data points within the filter window, especially when the features or data points being filtered are smaller than the filter window size (Tsai and Philpot 1998; Vaiphasa 2006; Miglani et al. 2011).

Larger filter windows provided increases smoothing effects; however, there is a trade-off between reducing noise and preserving the original data. Increased window sizes can potentially dampen features that best discriminate the GA and NA classes. Since the objective of this study was to identify regions of the spectra that best separate and classify these two classes, it was important to select an appropriate filter that smooths data but retains important features of the original data. Studies analyzing the effects of smoothing window size on vegetation spectra from hyperspectral data sets show that smoothing effects are negligible below a 7-point window size and that optimal window size for SG smoothing tends to be between 7- and 11-points wide (Miglani et al. 2011). To choose an appropriate smoothing filter size in this study, a Mann-Whitney U test was performed in SPSS® v. 22 to compare the number of significant differences between 7-, 9-, and 11-point filter sizes. Figure 3.4 gives a visual representation of the smoothing effect for each filter type. The 7-pt window had smallest number of significant differences from the raw data (Figure 3.5) and smoothed some of the fluctuations of the raw data while maintaining some of the band- to-band fluctuations observed in the raw reflectance spectra curves (Figures 3.4). Based on these results, a SG filter with a 7-point

window size was selected and is defined by:

$$Y_j^* = \frac{\sum_{i=-m}^{i=m} C_i Y_{j+1}}{N}$$

where  $Y_j^*$  is the data point to be smoothed,  $Y$  is the original data point,  $j$  is the running index of the ordinate data in the original table,  $m$  is the half-width of the window size,  $N$  is the total number of convoluting integers, and  $C_i$  is the coefficient for the  $i^{\text{th}}$  spectral value determined using quadriatic/cubic polynomial function tables published by Savitzky (1964).

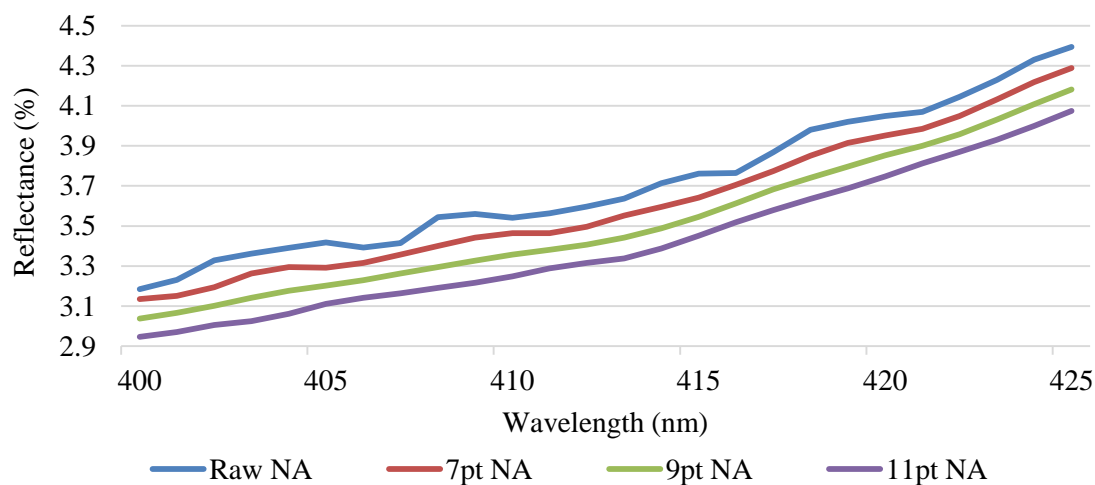


Figure 3.4. Effects of three smoothing filter sizes on spectral curves. Subset (400-425 nm) example of NA mean reflectance curve comparisons for the raw dataset and SG filter sizes. Mean reflectance curves are offset by 0.1% reflectance for each increase in filter size for visual comparison.

### 3.2.4 Spectral Reflectance Curves

To provide a visual representation of separation between the GA and NA trees, mean reflectance values for each class were plotted for all 2000 bands. Additionally mean spectral reflectance curves plus/minus one standard deviation were plotted to provide a visual representation of variance in reflectance values between the two classes.

Since the slopes of reflectance curves can make it difficult to visually assess differences between curves, the mean difference between GA and NA trees were calculated and plotted to provide a better representation of separation between the two groups.

### 3.2.5 Statistical Analysis and Best Band Selection

Descriptive statistics such as mean, median, and standard deviation both for the GA and NA classes were calculated. Distribution normality was examined using a Shapiro-Wilk test.

Since the high collinearity between spectral bands in hyperspectral datasets makes classification and modeling problematic, there is a need

to identify the bands that best separate the target groups and reduce the dimensionality of the dataset to create a more parsimonious group of predictors. There are numerous methods for reducing data dimensionality and identifying spectral features that best discriminate groups, each with strengths and weaknesses relative to the characteristics of the dataset. Previous research into using hyperspectral datasets to discriminate species, disease stages, or other vegetation stress have included analysis of variance techniques (Ahern 1989, Carter and Knapp 2001; Wang and Sousa 2009; Prospere et al. 2014),

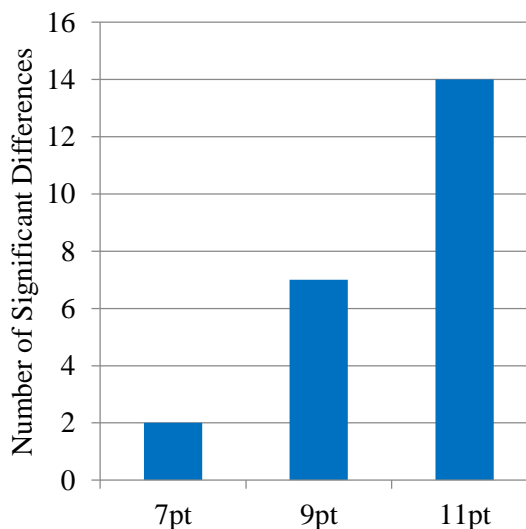


Figure 3.5. Number of significant differences between smoothed spectra and raw data. Total number of channels (400-2400 nm) with significant differences (Mann-Whitney U;  $p < 0.05$ ) between raw data and SG filters window sizes analyzed. Totals combine differences for both the GA ( $n=96$ ) and NA ( $n=89$ ) classes.

discriminate analysis techniques (Heath 2001; Thenkabail et al. 2004; van Aardt and Wynne 2007; Pu and Liu 2011), correlation analysis (Thenkabail et al. 2004), principle component analysis (Thenkabail et al. 2004; Prospere et al. 2014;), random forest (Prospere et al. 2014), support vector machine (Prospere et al. 2014), wavelet analysis (Cheng et al. 2010), and Mann-Whitney U tests (Prospere et al. 2014).

In this research, a multi-statistical method approach was undertaken in an attempt to utilize the benefits that different methods have relative to the dataset. The results of these methods are meant to complement each other and provide a higher level of confidence for predicting variable importance. Based on the results of the distribution normality tests the following parametric, non-parametric, and decision tree methods were used to analyze which bands were most sensitive to GA beetle damage.

### 3.2.5.1 Group Separation and Effect Size

A Mann-Whitney  $U$ -test was performed to examine significant differences between median reflectance values of individual bands of the GA and NA classes using the following equation:

$$U_i = n_1 n_2 + \frac{n_2(n_2 + 1)}{2} - R_i$$

where  $U_i$  is the U-statistic for band  $i$ ,  $n_1$  is the sample size for group 1,  $n_2$  is the sample size for group 2, and  $R_i$  is the sum of the ranks for band  $i$ . Since the  $U$  statistic has a normal distribution, the significance can be examined by calculating a standardized score ( $z$  - score) for each band using the following equation:

$$z = \frac{U_i - m_{u_i}}{\sigma_{u_i}}$$

where  $U_i$  is the U-statistic for band  $i$ ,  $m_{u_i}$  and  $\sigma_{u_i}$  is the standard deviation of  $U_i$ . This non-parametric test was used for bands with a non-normal distribution of GA or NA reflectance values (400-717 nm and 1003-2400 nm; Shapiro-Wilk,  $p < 0.05$ ). To provide a meaningful measure of the magnitude of difference (effect size) between GA and NA median values a Pearson's correlation coefficient  $r$  value was calculated using the following equation (Rosenthal 1991):

$$r = \frac{z}{\sqrt{N}}$$

where  $z$  is the  $z$ -statistic produced from the Mann-Whitney  $U$ -test and  $N$  is the number of observations used to produce the  $z$ -statistic. For bands with a normal distribution of reflectance values (718-1002 nm; Shapiro-Wilk,  $p > 0.05$ ) a parametric Student's  $t$ -test was used to analyze group differences. To measure the effect size of bands with parametric distributions a Pearson's correlation coefficient  $r$  value was calculated using the following equation (Rosenthal 1991):

$$r = \sqrt{\frac{t^2}{t^2 - df}}$$

where  $t$  is the  $t$ -statistic produced from the student's  $t$ -test and  $df$  is the degrees of freedom. Effect size provides a useful measure to analyze the magnitude of difference between GA and NA samples. In this context,  $r$  values range from zero (no effect) to 1 (perfect effect). Since effect size measures the amount of variance in values explained by group membership (Cohen 1988), it is assumed that bands with a larger effect size will have greater discriminatory ability. Since the  $r$  value is normalized for sample size they

can be compared between the Mann-Whitney  $U$ -test and student's  $t$ -test. Cohen (1988) interprets  $r$ -values greater than 0.5 to represent a large effect/difference between groups, accounting for 25% or greater of the total variance. Values less than 0.5 but greater than 0.3 as a medium effect size, and lower than 0.3 as a low magnitude of difference between groups.

### 3.2.5.2 Discriminant Analysis

Linear discriminate analysis (LDA) is a commonly used multivariate data mining and classification method used in hyperspectral studies (Heath 2001; Thenkabail et al. 2004; van Aardt and Wynne 2007; Pu and Liu 2011). Linear discriminant analysis is a supervised method that looks for linear combinations of known predictor variables to maximize between group variance to produce a single discriminate score that can then be used to classify group membership (Pohar et al. 2004). LDA is a type of parametric test that uses a least square estimations to discriminate groups and under ideal conditions it is a very powerful technique, however hyperspectral datasets can present a number of characteristics that violate LDA assumptions and potentially lower the robustness this technique. Along with the assumption of normality in the data, LDA is also sensitive to extreme outliers, multicollinearity issues, and assumes that the covariance matrices are homogenous between groups.

A variety of diagnostics were used to assess the data assumptions with respect to LDA. Mahalanobis distance provides information that can identify multivariate outliers (Atkinson 1994). For this dataset the Mahalanobis distance diagnostics ( $\chi^2_{0.99} = 2105.07$ ;

$df=2000$ ) indicated there were no samples that had a disproportionate influence on the analysis. Homogeneity between groups is problematic to fully analyze due to the sheer number of predictor variables (2000 bands), which makes it difficult to compare scatterplots between groups. A Box's M test provides a statistical measure that examines the null hypothesis that covariance is equal between groups (IBM Knowledge Center 2016). With this dataset a significant Box M test ( $p<0.001$ ) indicated a violation of the homogenous covariance assumption. However, the Box M test itself is highly sensitive to non-parametric data and should be interpreted with skepticism. The biggest threat to LDA is multicollinearity between predictors. A colinearity tolerance test was performed to analyze the proportion of variance for each predictor variable that is not accounted for by other predictors (UCLA Statistical Consulting Group 2016). In this study all but eleven of the 2000 predictors had tolerance values that indicated problematic multicollinearity issues ( $t<0.10$ ). Based on this, results from the LDA analysis should be interpreted with skepticism, especially if they show discrepancies with other measures of importance that are more robust against this multicollinearity issues.

One of the benefits of LDA is that it allows for a stepwise variable selection process in which the predictor variables are added or removed to the discriminate function based on the amount they can lower the overall Wilk's Lambda, or minimize the unexplained variance (IBM Knowledge Center 2016). This stepwise process continues until no variables can be added or lowered to significantly lower the Wilk's Lambda. In theory, this process should select variables that have the best discriminating ability and least redundant information. Another benefit of LDA is that it provides internal estimates

of variable importance. Correlation coefficients for each variable indicate the correlation between that variables and the latent variable (discriminate score) of the LDA function. Since the goal of LDA is to use a linear equation to reduce multiple predictor variables down to a single discriminate score that better separates the two groups, individual variables that are highly correlated with that score are assumed to have better discriminating ability themselves.

In this study two LDA techniques were used. First, a stepwise selection method (SDA) was performed using the aforementioned Wilks' Lambda criteria in SPSS® v. 22.0 (IMB Corp. 2013). Individual variable performance was assessed using the correlation coefficients for each band. In addition to SDA, LDA was performed for each individual band and the performance of each band validated using a leave-one-out cross-validation (LOOCV) accuracy, in which one sample is randomly left out of training to be used for accuracy assessment and the process is iterative to account for all samples. Individual LDA was performed using 'R' v.3.2.4 (R Core Team 2016) with R package 'MASS' v.7.3 (Venables and Ripley 2002) in an iterative script.

### **3.2.5.3 Logistic Regression**

To account for non-normal distribution and multicollinearity between variables, statistical methods that are robust against violations of these assumptions were also examined to determine variable importance. Logistic regression (LR) is similar to LDA techniques in that it attempts to predict a binary outcome variable using a linear combination of multiple continuous predictor variables. Unlike LDA, logistic regression

is a non-parametric method that uses maximum likelihood estimations to create a linear function that produces a latent variable that can then be used estimate the probability that a sample belongs to particular groups. It has fewer assumptions than LDA, making it a potentially more robust method for hyperspectral datasets. Probability of belonging to the GA class was predicted using the following logistic regression equation:

$$P(\text{GA}) = \frac{1}{1 + e^{-(b_0 + b_1 \lambda_1)}}$$

Where  $P(\text{GA})$  is the probability of a sample belonging to the GA class,  $e$  is the base of the natural logarithms,  $b_0$  is the linear constant (Y intercept), and  $b_1$  is the coefficient for the band used as the predictor variable ( $\lambda_1$ ).

While logistic regression is capable of handling multiple predicting variables, having fewer than 10 samples per predictor variable can create unreliable results and biased estimates of variable importance (Peduzzi et al. 1996). In this dataset there were 0.09 samples per predictor (185 samples/2000 bands). Furthermore, even though LR is more robust against multicollinearity compared to LDA methods, severe multicollinearity issues can lead to inflated standard errors and unreliable estimations of variable importance. To avoid potential issues caused by sample size and multicollinearity, LR models were created for each individual band as a predictor. This analysis was performed using ‘R’ v. 3.2.4 (R Core Team 2016) with R package ‘boot’ version 1.3-17 (Canty and Ripley 2015) and R package ‘pscl’ v. 1.4.9 (Jackman 2015) using a iterative script. Variable importance was examined using three different parameters. First, the prediction accuracies were determined using a LOOCV for each per-band LR model. Second, the Wald statistic was calculated to determine if the coefficients of a predictor variable were

significantly different from zero. Wald statistics have a chi-square ( $\chi^2$ ) distribution and variables that make a significant contribution to group separation have Wald  $\chi^2$  values greater than  $\chi^2$  critical values for the 0.05 probability level (df=1; N=185; Wald  $\chi^2_{\text{critical}} = 3.84$ ). Predictor variables with higher Wald statistics have a higher contribution to group separation. It should be noted that Wald statistics are highly sensitive to multicollinearity issues (Menard 2002) and should be interpreted with suspicion and validated in comparison to other measures of importance. Lastly, the odds ratio (OR) for each predictor variable was calculated using the following equation:

$$\text{OR} = e^{b_1}$$

Where  $e$  is the base of the natural logarithm and  $b_1$  is the coefficient of the band ( $\lambda_1$ ) variable used in the LR equation. The OR represents the odds a sample belongs to the GA class based on a one unit increase in reflectance (+1%) for a particular band (Field 2009). This measures magnitude of the effect that changes in band reflectance has on determining GA or NA group membership, with a higher absolute OR value indicating that a change in a particular band would lead to a higher probabilities of belonging to a particular group. Values above one show that increases in reflectance increase the probability of belonging to the GA group, while values below one indicating an increased probability of belonging to the NA group with reflectance increase.

#### **3.2.5.4 Random Forest**

The last method implemented was a Random Forest (RF) ensemble classification tree learner. A relatively new statistical method for classification, RF is becoming

increasingly popular in land-cover and vegetation mapping with both multi- and hyperspectral datasets (Ham et al. 2005; Pal 2005; Chan and Paelinckx 2008; Lawrence et al. 2006; Adam et al. 2012; Immitzer et al. 2012; Rodriguez-Galiano et al. 2012; Immitzer and Atzberger 2014). Random Forest is robust against issues such as low sample size-to-predictor variable ratios, non-parametric distributions, multicollinearity, and low signal-to-noise ratios which are characteristic of this dataset and hyperspectral datasets in general (Breiman 2001; Liaw and Weiner 2002). Another benefit of RF is that it is robust against overfitting models, provides an internal estimation of variable importance, and provides reliable measures of model error/accuracy without the need of a validation dataset (Breiman 2001; Liaw and Wiener 2002). Random Forest works by growing many small classification trees using random bootstrapped subsets of the training data and then aggregating the results of these smaller trees into a single “forest” classification system (Breiman 2001; Liaw and Weiner 2002). Model error is assessed by running the remaining samples not included in the bootstrapped training subset, termed the out-of-bag (OOB) sample, down its

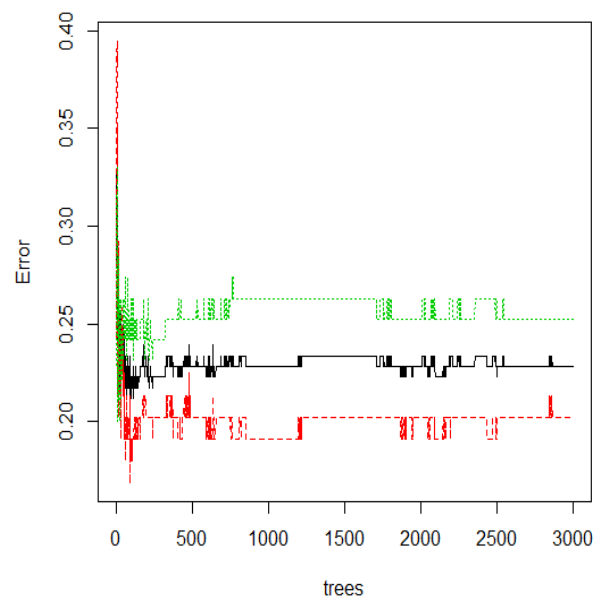


Figure 3.6. Random Forest OOB estimation of error with increasing number of individual trees. The black line represents the OOB of the overall RF model, the green is the OOB estimation for the GA samples, and the red is the OOB estimation of the RA samples.

respective smaller classification tree and aggregating these results to get an overall estimation of error (Breiman 2001; Liaw and Weiner 2002).

Variable importance is assessed by randomly permuted single predictor variables from the OOB sample and evaluating the decrease in accuracy of the permuted model relative to the complete OOB sample, then aggregating the results to achieve a mean decrease in accuracy (MDA) for each band if that predictor is left out of analysis. The OOB and MDA estimates have been shown to be reliable and comparable compared to more traditional accuracy assessment methods when applied to hyperspectral datasets (Lawrence et al. 2006). Random forest classification was done using the ‘R’ v. 3.2.4 (R Core Team 2016) with R package ‘randomForest’ v. 4.6 (Liaw and Wiener 2015) which is based on the original random forest procedures developed by Breiman and Cutler (Breiman 2001) with all 2000 bands input as predictors. To maximize the accuracy of the RF model two parameters, the number of individual trees created (ntree) and the number

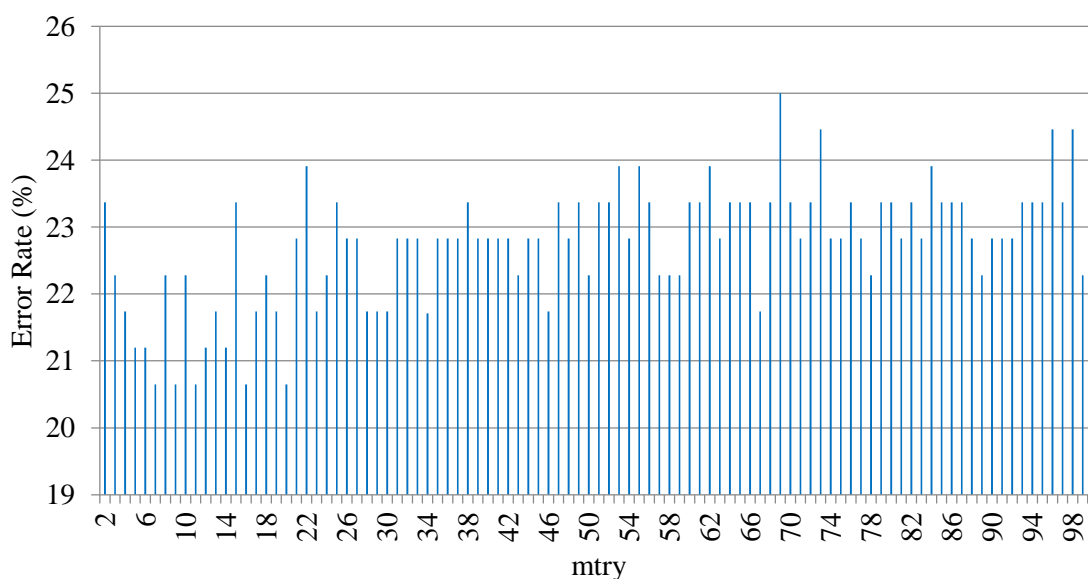


Figure 3.7. Random Forest OOB estimation of error for mtry settings from 1 through 100. Mtry represents the number of predictor variables used at each tree split. The lowest error rate was 20.65% and was observed for five mtry settings; 7, 9, 11, 16, and 20.

of predictors used at each tree split (*mtry*), were optimized using the OOB estimate to evaluate the optimal setting for parameter. A tree of 1000 was used based on the error rate stabilizing around 800-900 trees (Figure 3.6). The default *mtry* is set as the square root of the total number of predictor variables. Along with the default value (*mtry*=44), *mtry* values ranging from 2-100 variables were examined (Figure 3.7). Adjusting the *mtry* parameter had minimal impact on the error rate of the RF model. Five different *mtry* values had the lowest error rate (*mtry* = 7, 9, 11, 16, 20; error rate = 20.65%) and an *mtry* of twenty was selected for analysis.

### **3.3 Results**

#### **3.3.1 Spectral Reflectance Curves**

The mean spectral reflectance curves (Figure 3.8) and difference in mean spectral reflectance (Figure 3.9) provides a visual representation of the spectral response of and differences between GA and NA tree samples. Except for portions of the NIR (727-919 nm) and lower SWIR (1006-1121 nm) regions of the spectrum, the mean GA reflectance values are greater than NA means for all bands.

At shorter wavelength bands of the violet-blue region (400-450 nm) reflectance values for GA samples are relatively similar to NA samples, with GA trees being just slightly higher (<1% difference; Figure 3.8 & 3.9). Reflectance of GA trees increases relative to NA trees creating a small peak of mean differences above 1.25% from 474-523 nm with a maximum difference of 1.47% at 504 nm. Mean reflectance differences between the two groups become more similar approaching the green-peak (1.03%

difference at 538 nm), with a slight blue shift of the green-peak. Differences between the two groups increase through the yellow and red regions with GA higher than NA. A peak in mean reflectance differences above 2% is observed from 588-707 nm, including a small subset of bands from 680-699 nm in which the mean GA reflectance has a small but sharp increase compared to NA, with a maximum difference of 2.83% at 692 nm. Increased GA reflectance at the base of the red edge creates a slight blue shift in the lower bands of the red edge. Differences between GA and NA samples decrease with the rise of the red edge up to 727 nm, after which NA reflectance is higher than GA. Green attack reflectance is suppressed at the shoulder of the NIR and marks a region of peak differences above an absolute value of 1% from 736-794 nm, with a the mean NA reflectance reaching a greater than mean GA reflectance maximum difference of an absolute value of 1.68% at 751 nm. Differences between groups decrease from 751 – 920 nm followed by increasing GA reflectance relative to NA up to a peak value of 1.26% at 987 nm and is associated with the absorption feature centered at ~975 nm. Although peak differences between GA and NA samples in the NIR are comparable to those observed in the green regions (~475-550 nm), the highest standard deviations and overlaps in variance were observed in the NIR (Figure 3.8).

A small discrepancy between the FieldSpec Pro (VNIR dataset) and QualitySpec Pro (SWIR dataset) occurs at the transition between the datasets at 1002 to 1003 nm, with the GA reflectance slightly higher than NA at 1002 nm but slightly lower at 1003 nm. Spectral reflectance measurements were taken following well established guidelines (Analytical Spectral Devices 1999) for calibrating dark currents optimization and

reflectance standardization using white reference and the reason for this discrepancy is unaccounted for.

Within the SWIR dataset, deep absorption features are centered around bands at ~1200, ~1450 nm, and ~1930 nm, with a shallower absorption feature centered at ~ 1780 nm (Figure 3.8). Reflectance for GA needles is higher than NA needles throughout a majority of the SWIR region. Mean GA reflectance was 3% or higher than NA from 1326 – 1694 nm, 1753 – 1900 nm; and 1991 – 2038 nm (Figure 3.9). Within the 1326-1694 nm region there is a subset of bands with group differences above 4% from 1381-1420 nm with a maximum difference of 4.50% from 1398-1400 nm. Bands from 1753-1900 nm represents the second highest peak in mean reflectance difference with a maximum of 3.98% from 1874-1876 nm. The last peak from 1991-2038 nm has a maximum difference of 3.17% at 2012 nm.

Standard deviation (SD) in reflectance values provides information about regions of the spectrum in which the two classes have the least amount of overlap. For each band GA SDs were greater than NA samples (Figure 3.8). Within the VNIR GA standard deviations increases with increasing wavelengths, whereas the NA sample standard deviations stay relatively low ( $\pm 0.92$ -2.08%). Variance for both groups increases sharply with the rise of the red edge reaching maximums around ~ 765 nm and is relatively high for both samples throughout the NIR and lower SWIR. A notable decrease in the variance of NA values begins at approximately 1100 nm and with all of the bands from 1392-2400 nm having SDs between 0.69-1.80%. The variance of GA samples have the same general

trend of becoming smaller with increasing wavelength from 1100-2400 nm but have much more fluctuations in variance with a majority of bands having SDs between  $\pm 3-6\%$ .

There are no bands in the reflectance spectra in which the range of values  $\pm 1$  SD of the GA and NA means do not overlap (Figure 3.8). There are portions of the spectra in which the mean values for a particular group fall outside one SD of the other groups mean. Green-attack mean values are greater than plus one NA SD values from 464-521 nm and 587-700 nm with a peaks in separation at 504 nm and 687 nm respectfully. These ranges are associated with the peaks in separation located in blue-green region and near an absorption feature in the red spectrum. In the SWIR, GA mean reflectance was higher than plus one SD of NA mean values from 1331 – 2400 nm with notable regions from 1383-1561 nm (1405 nm peak), 1845-1905 (1881 nm peak), and 1976-2045 nm (2011 nm peak). There are no bands in which the NA mean reflectance values are outside  $\pm 1$  SD of the GA values.

### **3.3.2 Statistical Analysis and Best Band Selection**

#### **3.3.2.1 Group Differences and Effect Size**

Data measuring wavelengths 718-1002 nm were normally distributed both for the GA data (Shapiro-Wilk,  $df = 95$ ,  $p > 0.05$ ) and NA data (Shapiro-Wilk,  $df = 89$ ,  $p > 0.05$ ). Wavelengths 400-717 nm and 1003-2400 nm had a non-normal distribution both for the GA data (Shapiro-Wilk,  $df = 95$ ,  $p < 0.05$ ) and/or NA data (Shapiro-Wilk,  $df = 89$ ,  $p < 0.05$ ). Significant differences (Mann-Whitney-U;  $df = 1$ ;  $p < 0.05$ ) were observed between GA and NA reflectance values for bands located from 424-717 nm and 1151-2400 nm

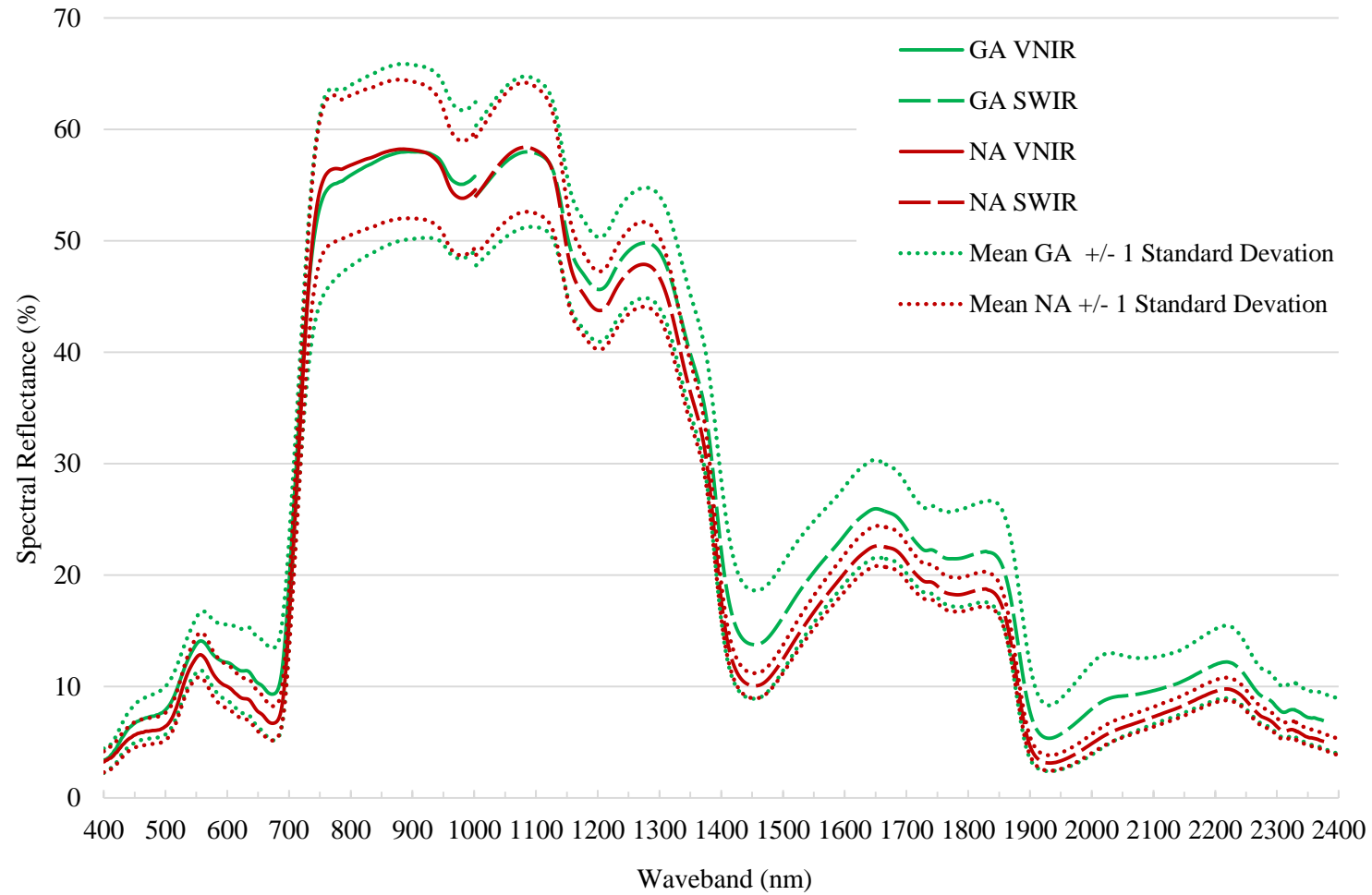


Figure 3.8 Mean reflectance spectra curves for GA and NA trees. Solid lines represent VNIR dataset (400-1002 nm) and dashed lines represent SWIR dataset (1003 -2400 nm). Dotted lines represent one standard deviation above and below the mean reflectance and are meant to give an estimation of the spectral similarities between the GA (n=95) and NA (n=89) classes.



Figure 3.9 Reflectance value differences between the mean GA and NA trees.

(Figure 3.10). Bands with a medium to high effect size ( $0.3 < r < 0.5$ ) were located from 457-519 nm, 575-698 nm, and 1328-2400 nm. Large magnitudes of differences (effect size  $r > 0.5$ ) were located at 1451-1541 nm and 1994-2045 nm. Regions that were not significantly different and had the lowest effect sizes were located below 424 nm and from the red edge to lower SWIR regions (718-1150nm). Within the VNIR datasets, the peaks in effect size were centered at 486 nm and 673 nm, which are associated by the left edge of the green-peak and red absorption feature respectfully. Within the SWIR dataset, the most prominent effect size peaks are centered at 1491 nm, 1884 nm, and 2010 nm, which are associated the left rise of the absorption feature at ~1925 nm, and subtle rise of an absorption feature between 2000-2050 nm respectfully. Additional regions that showed a significant difference but a low magnitude of difference were located in the blue (424 nm-456 nm), the green-peak (520-574 nm), along the lower half of the rise of the red edge (699-17 nm), and the absorption feature and reflectance peak located in the lower SWIR (1150-1327 nm).

### 3.3.2.2 Discrimination Analysis

The stepwise discriminant analysis (SDA) underwent nine iterations and selected nine wavelengths before terminating the selection process. The final discriminate function had a canonical  $R^2$  of 0.61 and significantly differentiated the RA and GA trees (Wilks Lambda = 0.389;  $\chi^2=167.610$ ;  $df=9$ ;  $p<0.001$ ). Table 3.2 lists the nine variable

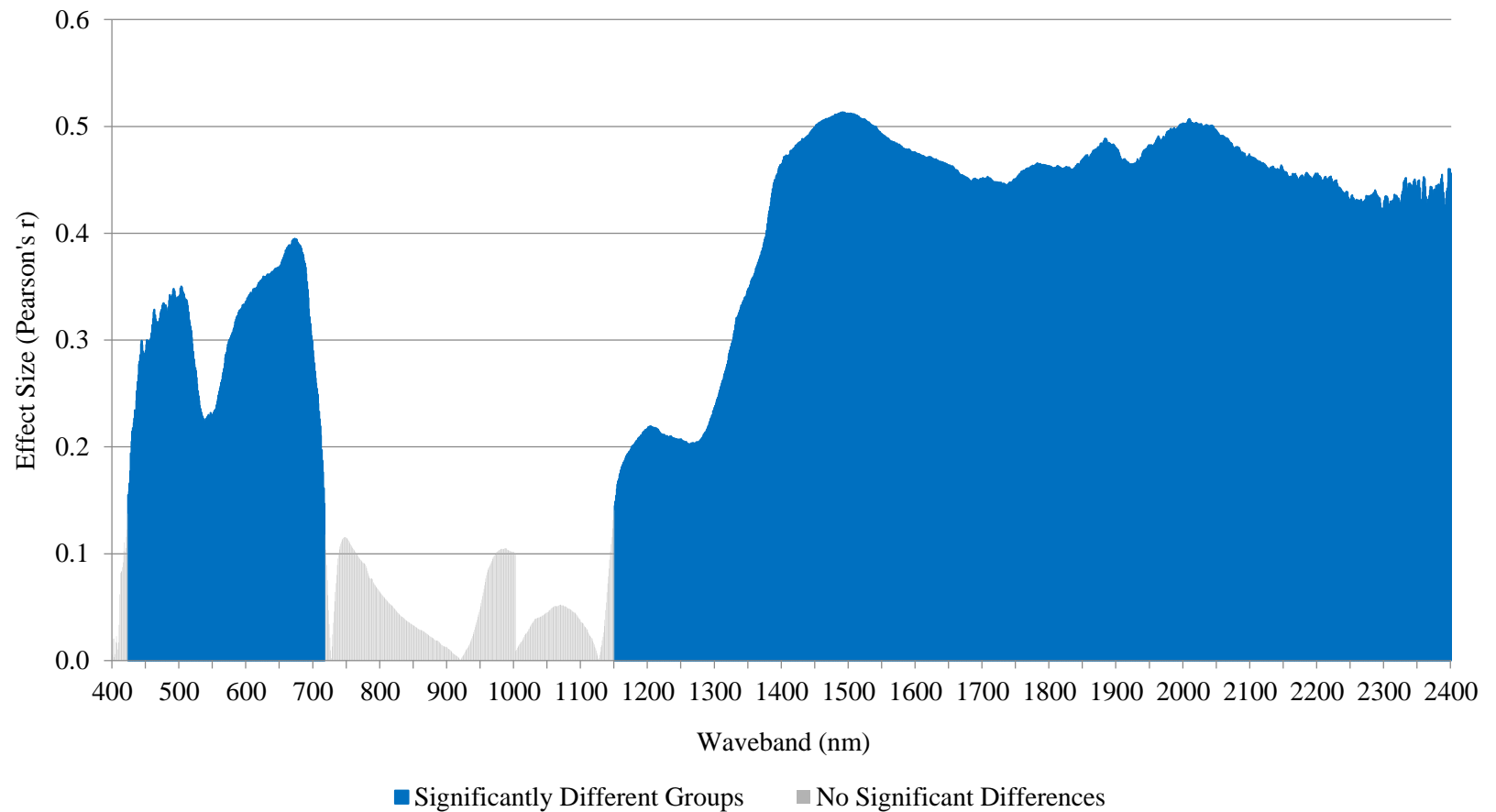


Figure 3.10. Pearson's  $r$  effect size of differences between GA and NA reflectance values. Mean and median reflectance differences were analyzed using a Mann-Whitney-U test for wavebands 400-717nm and 1003-2400 nm; a t-test was performed for wavebands 718-1002 nm. Blue bars represent wavebands in which the mean or median reflectance differences were significant (d.f.=1;  $p < 0.05$ ) and light gray represent wavebands with no significant differences between groups (d.f.=1;  $p > 0.05$ ). Figure 12. Reflectance differences between the GA and NA classes for the VNIR dataset (400-1002 nm) and SWIR dataset (1003-2400 nm). Differences were determined as the mean GA reflectance values minus the mean NA reflectance values.

Table 3.2. Wavebands selected by stepwise LDA method. Standardized canonical discriminant function coefficients indicate the relative contribution each waveband has within the function, with higher absolute values indicating more influence. The structure coefficients represent the correlation between each band and the discriminate function. This is an indication of discriminatory power for each band as a stand-alone variable.

<b>SDA Selected Wavebands (nm)</b>	<b>Standardized Canonical Discriminant Function Coefficients</b>	<b>Structure Coefficients</b>
463	15.92	0.31
509	-12.25	0.32
503	10.98	0.33
467	-9.10	0.30
1863	-5.19	0.39
1509	5.68	0.42
458	-4.99	0.29
404	-1.16	0.02
572	0.69	0.26

selected along with their standardized canonical discriminant function coefficients, which indicates the variables contribution to the overall function coefficient, and correlation coefficients. The SDA function had a LOOCV overall accuracy of 89.7%. A majority of the best selected

were located in the blue and green-peak rise regions of the spectrum (Table 3.2). As expected selected bands generally have high correlation coefficients but is not always the case as the band at 404 nm has a low correlation coefficient. Since the bands are selected based on whether they improve the overall function and not necessarily the best discriminating bands individually, it is possible that bands with low discriminating power selected for the final model. This is why the bands with the highest standardized canonical discriminant function coefficients do not have the highest correlation coefficients (Table 3.2) and why using stepwise selected bands as the sole indicator of which bands are most sensitive to damage.

Structure coefficients provide information about the relative importance of each bands' discriminatory ability thus which are more sensitive to MPB damage. Within the

VNIR dataset there are two prominent peaks in structure coefficients. The greater of the two peaks is centered at 675 nm, with most bands from 650-691 nm having coefficients above 0.4 (Figure 3.11). Another notably peak in the VNIR with values above 0.3 ranges from 462-516 nm and is centered at 496 nm. Structure coefficients drop steeply with the rise of the red edge and are lower throughout the NIR plateau. Compared to the VNIR bands, the SWIR bands had consistently higher structure coefficients (Figure 3.11), with most bands from approximately 1400-2400 nm having correlations higher or near 0.4, with two shallow sloped but distinct peaks in values. The first of these two peaks ranges from 1418-1672 nm, with a maximum coefficient at 1533 nm. The second peak ranges from 1982-2292 nm, with a maximum at 2089 nm. Most bands from 2293-2400 nm also have structure coefficients above 0.4; however, there tends to be greater fluctuations between bands and their neighbors, making it difficult to distinguish smaller regions of bands showing consistent sensitivities to damage. The last region of bands with values near or above 0.4 in the SWIR ranges is from 1747nm - 1821 nm.

When using individual bands as single predictor variables in LDA the classification accuracies (Figure 3.12) show similar trends as the structure coefficients with few major discrepancies increasing confidence in the stability of the SDA correlation coefficients as estimates of variable importance. Within the VNIR dataset, these similarities include increased LDA accuracies from the blue region to the red edge (approximately 430-719 nm; Figure 3.12). Notable peaks in LDA accuracies above 65% include bands from 663-689 nm, with a peak accuracy of 66.85% from 667-669 and 683 nm, and bands located from 521-527 nm, with a peak accuracy of 65.76% at 522-523 nm.

Another notable VNIR peak was observed for bands from 578-599 nm, which yielded accuracies above 64.5%. Similar to the SDA structure coefficient trends in the VNIR, the LDA classification accuracies were lower in the visible regions, with a sharp drop off in values with the rise of the red edge (at approximately 720 nm), and were relatively lower throughout the NIR portion. Again similar to the SDA structure coefficients, the LDA classification accuracies are generally higher for majority of the SWIR bands (~1350-2400 nm) compared to the VNIR dataset (Figure 3.12). The lowest accuracies in the SWIR dataset were observed at lower wavelengths bands from 1003 nm to approximately 1300 nm. Accuracies start to rise at ~ 1300 nm and reaching accuracies above 70% for individual bands at 1379 nm with accuracies consistently at or higher than 70% throughout the rest of the SWIR dataset with exception to some bands located from ~2200-2400 nm. This consistency in values makes it more difficult to isolate notable regions that distinguish themselves from other SWIR bands. However, there are number of small regions that are notably higher.

The highest accuracies attained for either datasets was 74.46% for bands at 1392 nm and 1404-1409 nm. These are part of a group of bands with values above 73% from 1389-1394 nm and 1400-1424 nm. Table 3.3 lists other notable regions of bands that yielded LDA classification accuracies that separate themselves from neighboring bands in the SWIR.

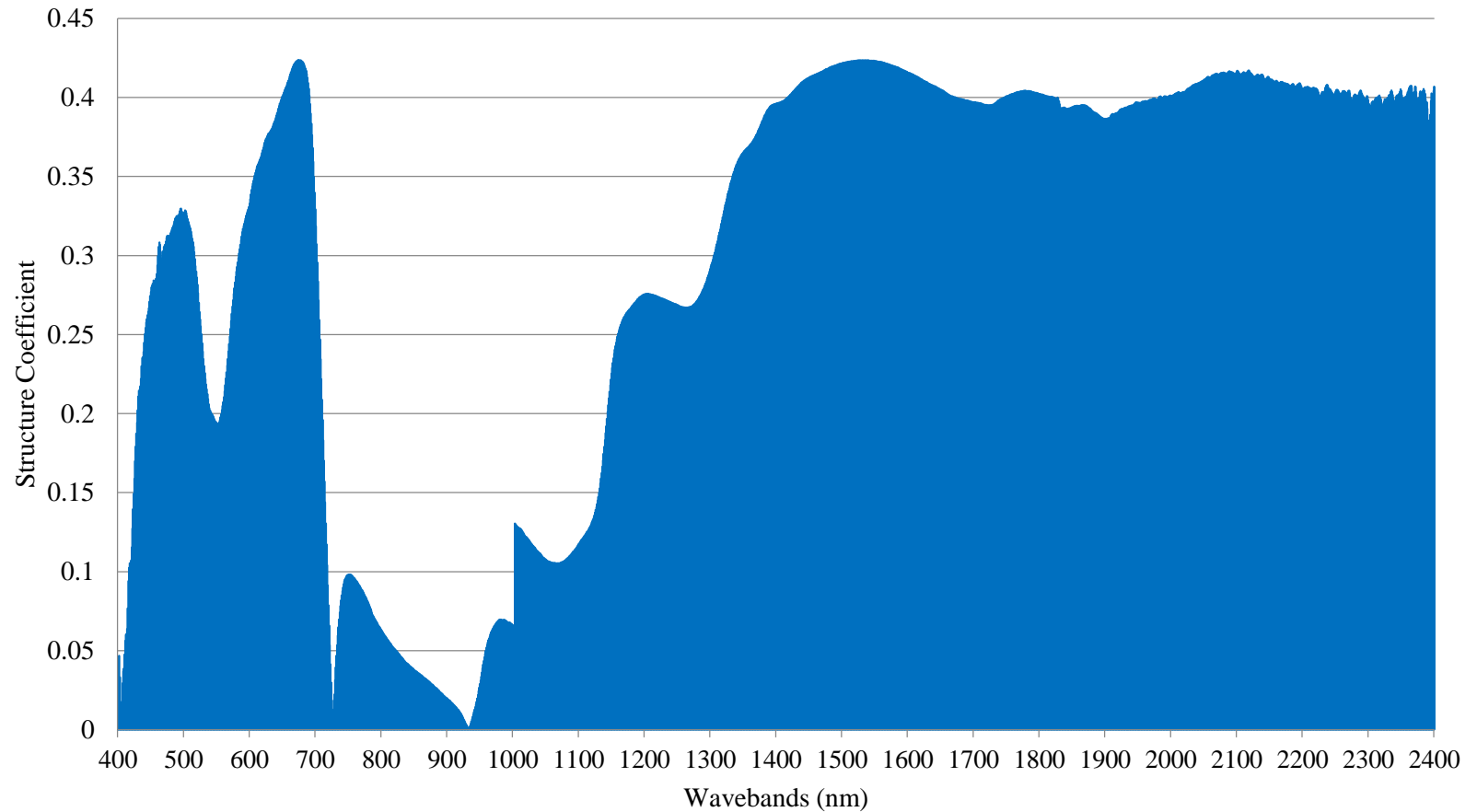


Figure 3.11. Discriminant analysis structure coefficients for each band. For display and easy comparison only on the absolute values are given on this figure, actual coefficients may have a negative correlation for a particular band however for illustrating the magnitude of importance of wavebands this was not deemed important information. Coefficients represent the correlation between each waveband and the SDA function discriminant scores. Higher coefficients indicate greater discrimination between the GA and NA groups at a particular band.

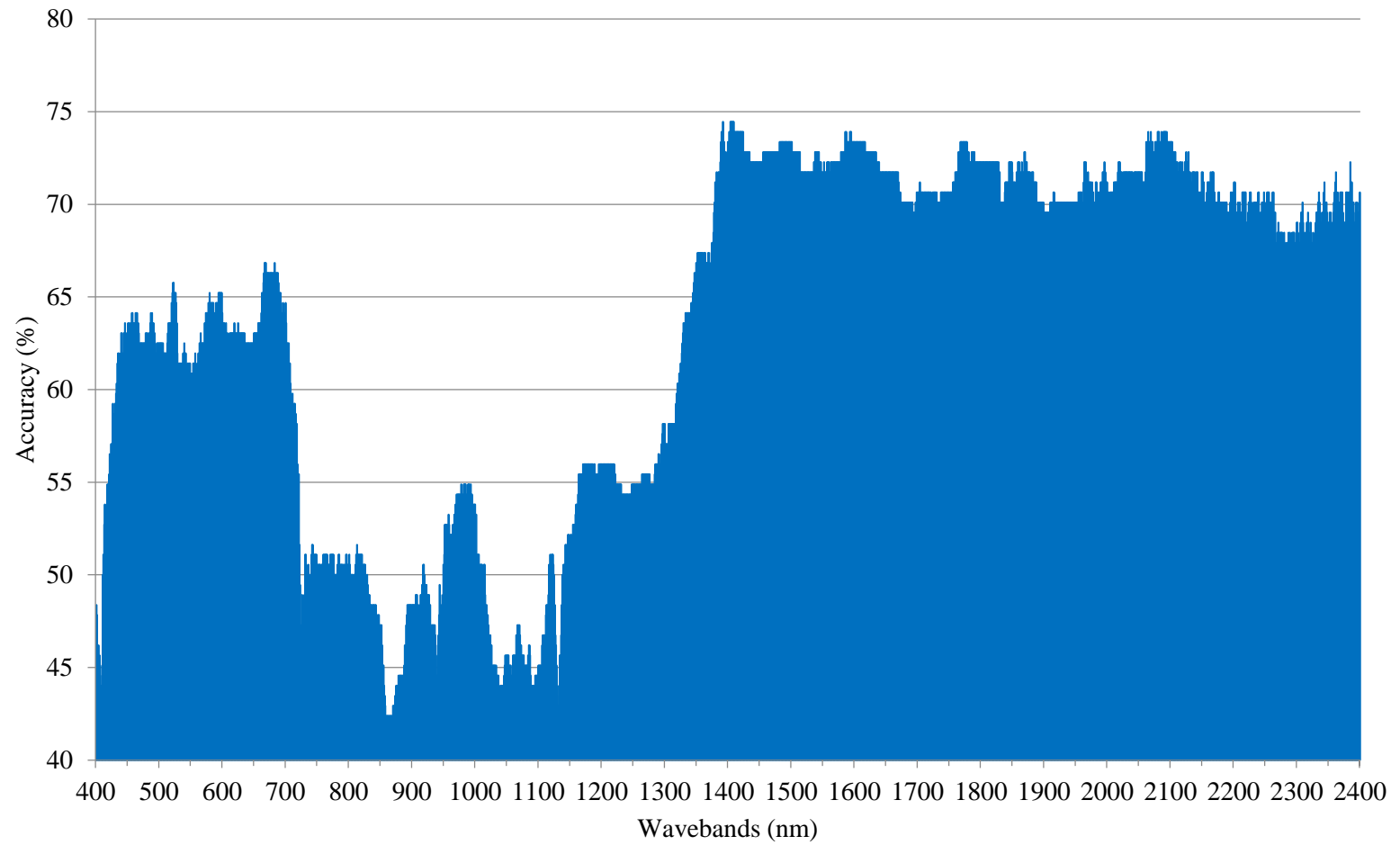


Figure 3.12. Leave-one-out cross validation classification accuracies for per band linear discriminant analysis.

Table 3.3. Band ranges with notable SWIR peaks in LDA accuracies. The minimum and maximum accuracies indicate the lowest and highest accuracies recorded for the given region wavebands.

<b>Bands (nm)</b>	<b>Minimum Accuracies</b>	<b>Max Accuracies (peak band)</b>
1389-1424	72.28%	74.46% (1392;1404-1409 nm)
1482-1501	73.37%	73.37%
1586-1617	73.37%	73.91% (1586-1587;1593-1595 nm)
1768-1778	73.37%	73.37% (1768-1778 nm)
2062-2103	72.28%	73.91 (2065; 2069; 2080-2082; 2086; 2089-2094 nm)

### 3.3.2.3 Logistic Regression

Based on per band logistic regression (LR) analysis, the following three statistical parameters, Wald statistics, LOOCV classification accuracies, and odds ratios (OR), were used to assess which wavelengths are most sensitive to MPB GA damage. A majority of the bands produced LR coefficients that significantly contributed to predicting GA and NA group membership (Figure 3.13). Bands from 431-707 nm and 1301-2000 nm had coefficients that were significant to  $p < 0.001$  threshold ( $df=1$ ;  $N=185$ ; Wald  $\chi^2 > \chi^2_{10.83}$ ). Within the VNIR dataset there are two distinct peaks in Wald statistics. The higher of these two peaks includes bands in the yellow and red regions of the spectrum from 555-707 nm with Wald statistics significant to the  $p < 0.001$  level ( $df=1$ ;  $N=185$ ; Wald  $\chi^2 > \chi^2_{10.83}$ ). This peak is centered around bands from approximately 650-675 nm, with the maximum at 662 nm (Figure 3.13). A similar spike in Wald statistics above the  $p < 0.001$  threshold are associated with bands located in the blue and blue-green regions of the spectrum from 431-546 nm ( $df=1$ ;  $N=185$ ; Wald  $\chi^2 > \chi^2_{10.83}$ ). This peak is centered around bands from approximately 486-507 nm, with the maximum value for this peak at 503 nm. Wald values begin to drop with bands associated with the rise of the red edge and are

below the  $p < 0.05$  significance threshold ( $df=1$ ;  $N=185$ ; Wald  $\chi^2 > \chi^2_{3,84}$ ) throughout the NIR regions of the spectrum (726-1152 nm). This indicates that bands in this region had LR coefficients that did not determine group membership different than a null value.

SWIR bands have significant Wald statistics ( $p < 0.05$ ;  $df=1$ ;  $N=185$ ; Wald  $\chi^2 > \chi^2_{3,84}$ ) from 1153-2400 nm and above the  $p < 0.001$  threshold from 1300-2400 nm (Figure 3.13).  $df=1$ ;  $N=185$ ; Wald  $\chi^2 > \chi^2_{10,83}$ ). Compared to the VNIR region, Wald statistics for SWIR dataset bands are generally higher and have less pronounced peaks. The most notable increase in Wald values was located from 1451-1550 nm, with a maximum value at 1497 nm. Another prominent rise is from 1973-2114 nm and with a maximum Wald statistic at 2043 nm (Figure 3.13). Other less prominent peaks in values are centered around bands at 1782 nm and 1899 nm.

The per-band LR LOOCV accuracies have the same general trends as the Wald statistics with peaks in LOOCV accuracies in similar parts of the spectrum as peaks in Wald statistics (Figure 3.14). Also similar to the Wald statistics, a majority of the SWIR bands have higher LOOCV classification accuracies than the VNIR bands. Within the VNIR dataset the highest accuracies were associated with the blue through red regions of the spectrum, with accuracies dropping with the rise of the red edge and consistently lower throughout the NIR and lower SWIR portions of the datasets (Figure 3.14). Within the blue, green, yellow, and red regions notable peaks in values are less discernable visually relative to the Wald statistics. There is a notable peak of classification accuracies greater than 63% from 670-697 nm, with a maximum accuracy of 66.00% at 693 nm. There is another rise in accuracies from 583-650 nm. These bands all have relatively

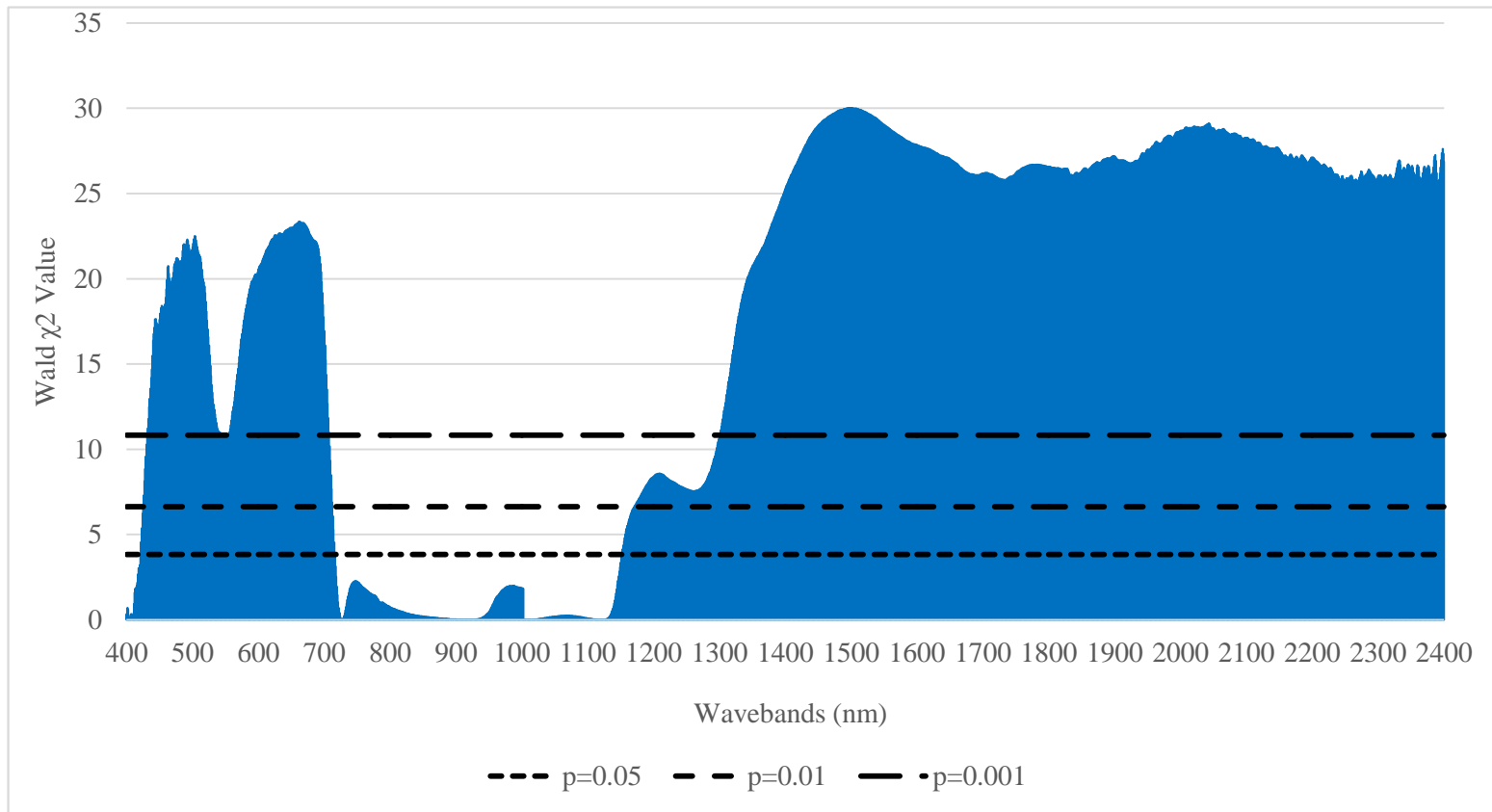


Figure 3.13. Wald Chi-square values for per-band logistic regression analysis. Bands with values above significant thresholds indicate coefficients that predict GA and NA group membership significantly better than null values. Higher values indicate a greater degree of group separation

similar accuracies ranging from 63.09% to a maximum of 64.87% located at 617 nm. Slightly smaller increases in accuracies were observed from 519-526 nm with a peak accuracy of 63.61% at 520 nm and from 453-464 nm with a peak accuracy of 63.42% at 464 nm.

In the SWIR dataset LOOCV accuracies begin to rise around ~1300 nm, with a large number of bands from 1380-2083 nm and 2347-2400 nm producing LOOCV accuracies between 70% and 75% (Figure 3.14). Accuracies in these two regions have relatively consistent values, with only a few smaller regions of peaks that are distinguishable from neighboring bands. A visual assessment of the SWIR accuracies indicate six regions that show separation from neighboring bands that may be useful for other applications. The highest classification accuracy for the entire spectrum was 75.25% and is associated with the band at 1891 nm, which centers a spike in accuracy values above 72% from 1883-1899 nm. The next highest peak in accuracies includes a group of bands from 1477-1553 nm with maximum accuracies between 74.0-74.5% from 1493-1498 nm (Figure 3.14). Two groups of bands with accuracies above 72% were located from 1430-1472 nm and 1384-1399 nm with the maximum accuracies at 1447 nm and 1385 nm respectfully. The last two notable peaks in bands with accuracies above 72% were from 1972-1976 nm, with a peak accuracy of 72.75% at 1975 nm, and 2023-2047 nm, with a peak 72.89% at 2043 nm (Figure 3.14).

Consistent to the Wald statistics and LOOCV accuracies, the individual band OR values were higher in the SWIR spectrum compared to the VNIR with peak values at similar locations of the spectrum (Figure 3.15). In the VNIR the highest peak in ORs was

located in the blue spectrum instead of red, centered around the bands at 462 nm and 463 nm with an OR of 1.68 (Figure 3.15). These bands are part of a larger group of bands with ORs over 1.5 from 430 nm to 520 nm and cover much of the blue to blue-green portions of the reflectance spectra. A second VNIR peak is located in the yellow to red regions of the reflectance spectra and has a maximum OR of 1.50 at 675 nm. This peak starts with a shallow rise in values at 555 nm before dropping back to similar OR values around 699 nm, and has a smaller subset of bands distinguished by a sharp rise from approximately 629-699 nm. Similar to the Wald and LOOCV parameters, ORs drop rapidly with the rise of the red edge and are consistently lower throughout the NIR and lower SWIR bands (~700-1300 nm). Most of the ORs in this range indicate that changes in the reflectance for these bands have very little difference in changing the probability of belonging to either class (OR value = 1).

In the SWIR dataset there are two notable peak regions that have OR values equal to or greater than 2.0. The greater of the two is located from 1892-2166 nm (Figure 3.15) with a smaller subset of bands with ORs greater than 2.5 from 1924-1951 nm and a maximum of 2.55 at 1941 nm. A second peak of OR values greater than 2.0 is located from 2260-2400 nm, with the maximum of 2.43 at 2399 nm. A third smaller peak in values above 1.5 range from 1399-1653 nm and is centered around a maximum of 1.90 at 1464 nm.

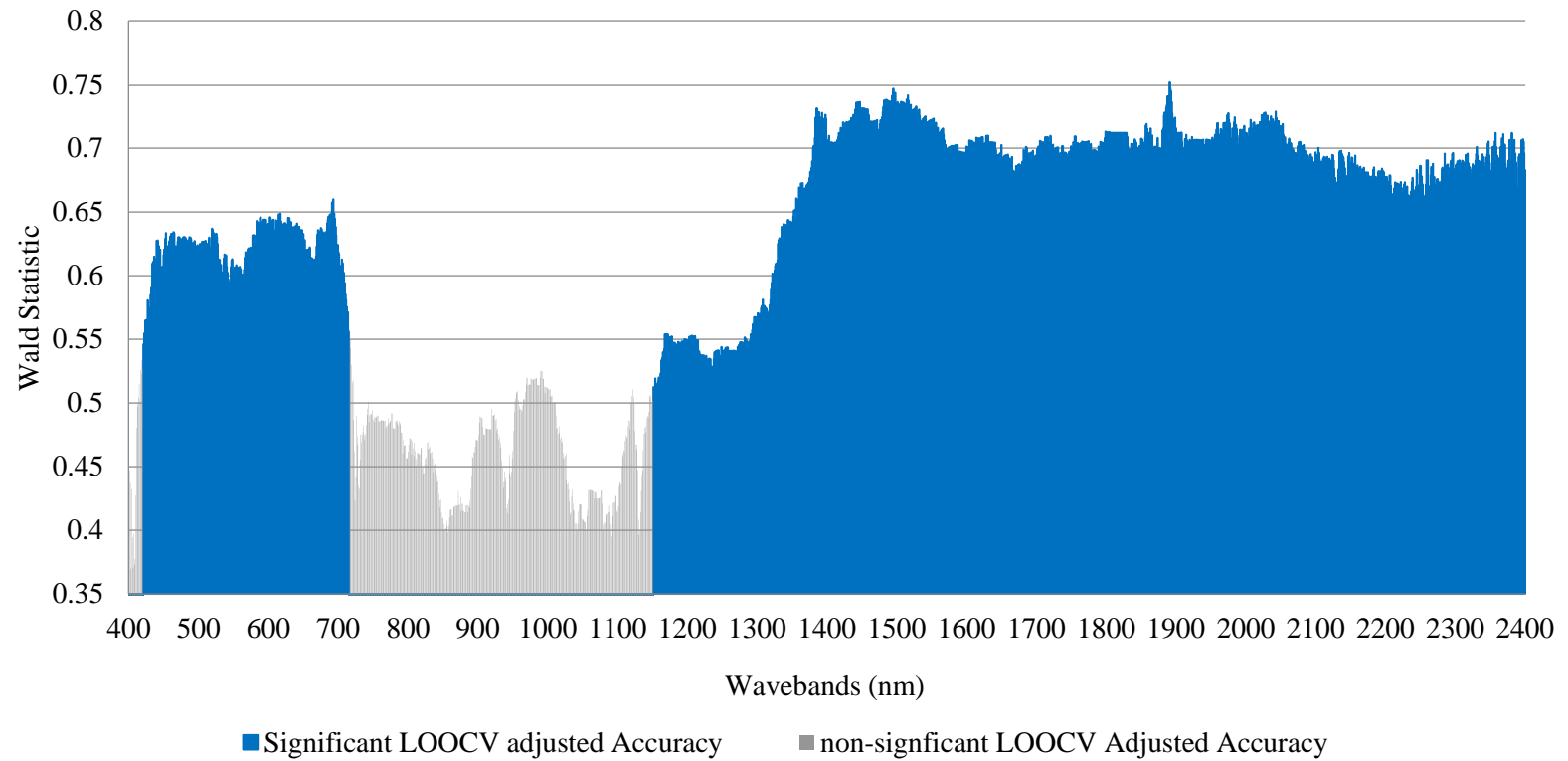


Figure 3.14. LOOCV accuracies per waveband LR analysis. Blue bars represent wavebands that had significant Wald statistics ( $df=1$ ,  $n=185$ ,  $p<0.05$ ). Light gray bars represent the LOOCV accuracies of wavebands that did not have significant Wald statistics ( $p>0.05$ ).

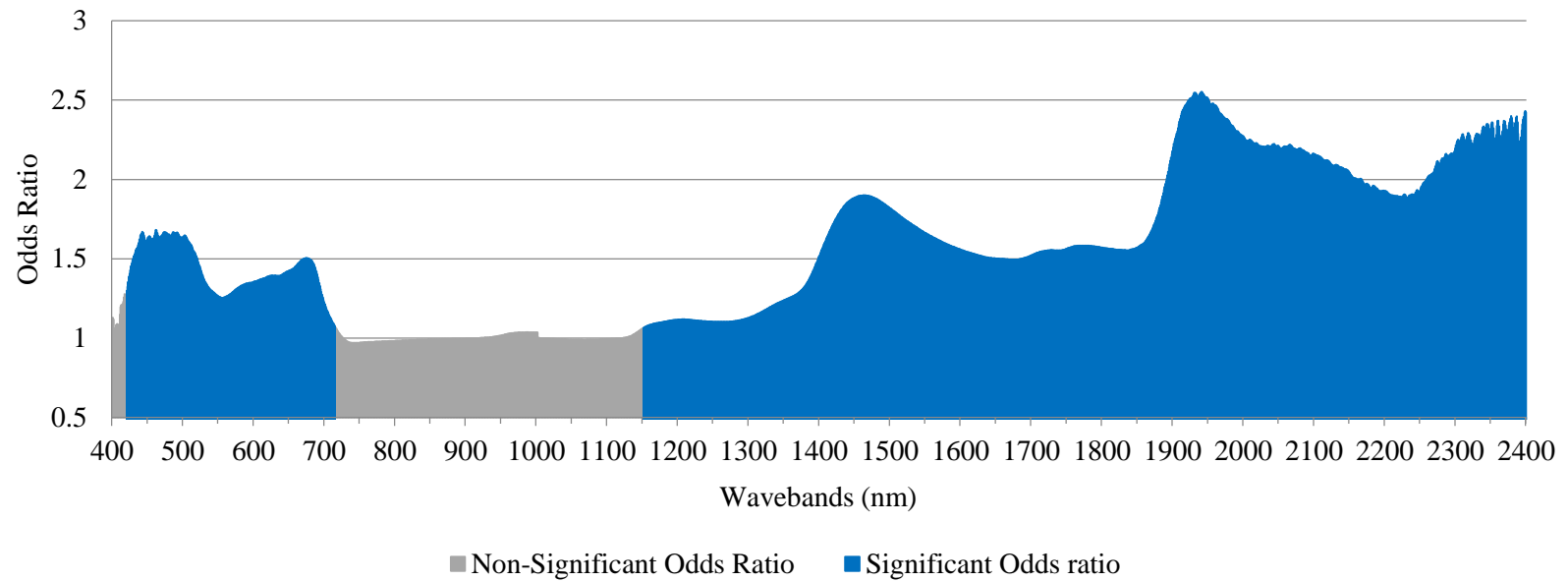


Figure 3.15. Logistic regression per waveband odds ratio. Blue bars represent the odds ratios of wavebands that had significant contributed to group discrimination ( $df=1$ ,  $n=185$ ,  $p<0.05$ ). Grey bars represent odds ratios or wavebands that did not significantly discriminate groups ( $p>0.05$ ). Odds ratios represent the increased probability of a sample belonging to the GA group with a 1% increase in reflectance is observed. For example, an odds ratio of two indicates that a sample is two times more likely to belong to the GA group with an 1% increase in reflectance. For graphical simplicity only absolute OR values are shown.

### 3.3.2.4 Random Forest Results

The RF OOB estimation of error for the overall model was 79.35% ( $Kappa = 0.59$ ). Producers and users accuracies for the GA class were 84.27% and 75.76% respectively and for the NA class were 74.74% and 83.53% respectively. Figure 3.16 represents the overall MDA for each band. Since the MDAs vary more drastically band to band compared to the other statistical parameters of importance examined in this research, it is difficult to visually discern regions of importance. As such, an eleven-point moving average filter was applied to the MDA to create a trend line to better visually indicate and generalize regions of the spectrum that maybe important for discriminating the groups (Figure 3.16). The reasons for the inconsistencies between neighboring bands remains unknown, however the filtered trend line peaks and bands with the highest MDAs (Table 3.4) are consistently located in spectral regions with the largest mean reflectance differences, increasing the confidence in using an average filter to interpret the results.

Table 3.4 lists the 25 bands with the highest overall MDA for both the VNIR and SWIR datasets. Within the VNIR dataset, the band at 627 nm has the highest MDA (3.25%). This band and three others with the high MDAs are part of peak region of bands with relatively higher MDAs from approximately 620-630 nm (Table 3.4; Figure 3.16). A second peak is observed from 653-687 nm, with a maximum MDA of 3.22% at 681 nm (Table 3.4; Figure 3.16). These two peaks account for a majority of the bands listed in

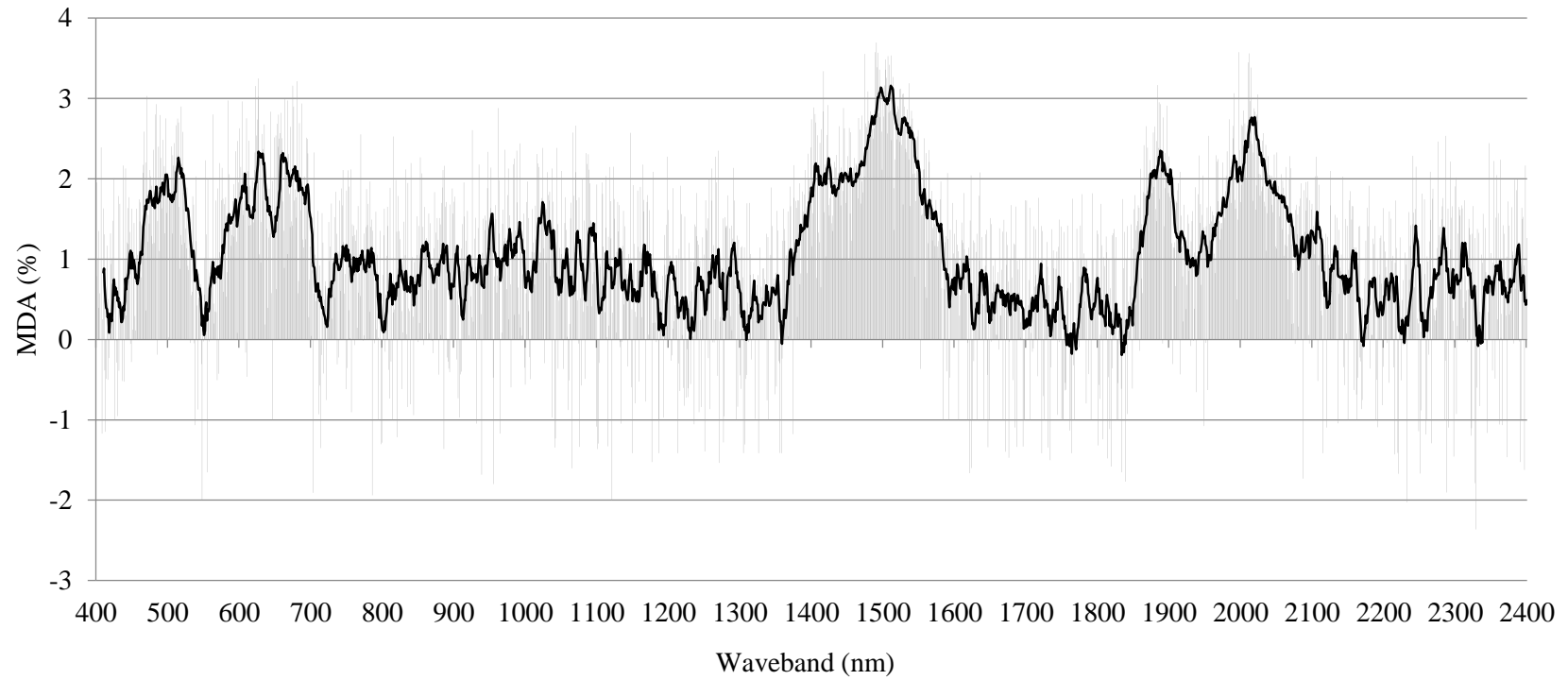


Figure 3.16. Random Forest out-of-bag estimation of mean decrease in accuracies. The black trend line represents an eleven point mean average filter and is used to visualize the general trends in values.

Table 3.4 VNIR and SWIR bands with 25 highest overall mean decreases in accuracies. The GA and NA MDAs represent decreases in class accuracies for each band if permuted from the OOB sample RF classification.

<b>VNIR Dataset</b>				<b>SWIR Dataset</b>			
<b>Waveband (nm)</b>	<b>NA MDA</b>	<b>GA MDA</b>	<b>Overall MDA</b>	<b>Waveband (nm)</b>	<b>NA MDA</b>	<b>GA MDA</b>	<b>Overall MDA</b>
<b>627</b>	2.274	1.572	3.251	<b>1491</b>	2.743	2.153	3.695
<b>681</b>	3.244	2.068	3.216	<b>1997</b>	3.342	1.265	3.575
<b>675</b>	3.230	0.175	3.160	<b>1489</b>	3.607	2.659	3.575
<b>623</b>	2.518	1.422	3.155	<b>1493</b>	3.360	2.194	3.568
<b>471</b>	3.249	-0.140	3.031	<b>2012</b>	2.229	2.890	3.561
<b>626</b>	2.012	1.474	3.018	<b>1475</b>	1.928	3.082	3.553
<b>664</b>	2.209	1.427	2.998	<b>1511</b>	2.273	2.678	3.535
<b>668</b>	2.870	0.193	2.976	<b>1507</b>	3.320	2.489	3.529
<b>585</b>	2.311	1.503	2.973	<b>1503</b>	3.141	2.578	3.488
<b>604</b>	2.691	0.798	2.963	<b>2011</b>	1.864	2.945	3.447
<b>687</b>	2.030	1.806	2.935	<b>1509</b>	3.270	1.489	3.417
<b>484</b>	2.667	0.633	2.930	<b>1492</b>	2.457	2.389	3.389
<b>676</b>	2.782	1.448	2.899	<b>2015</b>	2.252	2.954	3.386
<b>519</b>	3.025	0.205	2.898	<b>1504</b>	3.063	1.606	3.359
<b>962</b>	2.277	0.550	2.879	<b>1495</b>	2.259	2.522	3.358
<b>644</b>	1.841	1.892	2.835	<b>1417</b>	2.605	2.530	3.340
<b>658</b>	2.559	2.027	2.820	<b>1514</b>	2.660	2.041	3.269
<b>483</b>	2.416	0.154	2.803	<b>1505</b>	3.094	1.818	3.256
<b>563</b>	0.898	1.549	2.800	<b>1537</b>	2.547	1.317	3.191
<b>655</b>	3.152	-0.244	2.797	<b>1884</b>	2.478	2.452	3.165
<b>489</b>	2.134	1.497	2.794	<b>1502</b>	2.314	2.353	3.163
<b>610</b>	2.327	1.431	2.753	<b>1513</b>	2.779	2.079	3.142
<b>497</b>	2.365	0.116	2.752	<b>1497</b>	3.167	2.450	3.128
<b>514</b>	2.096	2.076	2.750	<b>1525</b>	2.003	2.484	3.121
<b>625</b>	2.279	1.195	2.739	<b>1524</b>	2.896	0.722	3.119

Table 3.4. The last notable peak in the VNIR dataset was located from 465-521 nm (Figure 3.6), with a maximum of 3.03% at 471 nm (Table 3.4). Similar to other statistical parameters, MDA drops with the rise of the red-edge at approximately 700 nm and is relatively low throughout the NIR and lower SWIR bands (Figure 19).

There are three notable regions within SWIR dataset with MDAs that indicate greater discriminating ability. The highest peak begins with a rise in MDAs at approximately 1391 nm, with MDAs consistently near or above 2% until dropping at approximately 1540 nm. On a smaller scale, this peak is punctuated by bands with MDAs near or above 3% located from 1489-1527 nm (Figure 3.16). This narrower region contains the highest overall MDA value of 3.70% at 1491 nm, along with 18 of the 25 highest MDA values in the SWIR dataset (Table 3.4; Figure 3.16). The second highest SWIR MDA peak is located from approximately 1980-2035 nm and is punctuated by a MDA of 3.58% at 1997 nm and includes four other MDAs above 3%. The third prominent increase in MDA was observed from 1869-1893 nm and has a maximum MDA of 3.17% at 1884 nm (Figure 3.16). The MDAs are relatively low for bands between ~1580-1850 nm and ~2070-2400 nm and are similar to the lower MDA values observed for the NIR and lower blue spectrum bands.

### **3.4 Discussion**

Multiple studies have attempted to characterize early spectral responses in pine foliage following MPB infestations and identify which spectral regions maybe useful for discriminating GA from NA trees (Ahern 1988; Cheng et al. 2010; Niemann et al. 2015).

However these studies have generally used small sample sizes from homogenous stands, have been limited to the visible and NIR spectrum, and collected in the fall following the initial attack. This study attempts to determine which spectral bands to separate GA from NA trees by identifying narrow bands that are sensitive to the pre-visual changes using needle-level hyperspectral measurements. The benefits of capturing reflectance from direct contact with foliage include decreasing inconsistencies due to illumination angles, background interference, and atmospheric effects. Furthermore a large number of samples were collected from trees in various locations with different stand ages and attributes.

### **3.4.1 Statistical Methods**

Nearly all of the statistical parameters used in this study showed similarities and overlap in spectral regions that best discriminated damage classes (Figures 3.10 – 3.16). These regions also correspond to the spectral regions with the greatest mean differences and least amount of overlap in variance between the classes (Figures 3.9). Only the SDA selected bands showed inconsistencies with other parameters. A majority of SDA selected bands (Table 3.2) were not selected from the spectral regions with the best indicators of separation between the groups based on the other parameters examined (Table 3.5; Figures 3.9 – 3.16). Even though a commonly used method in hyperspectral studies, research has shown that stepwise selection methods can give inconsistent results (Thompson 1995). Based on this the SDA selected bands were not considered in discussion.

### 3.4.2 Spectral Regions Separation for GA and NA Classes

Table 3.5 provides a summary of the notable regions that showed the best discriminating ability for each parameter and the peak band(s) for each of those regions. Compared to VNIR, bands in the SWIR generally had greater differences between groups and/or contributed more to discrimination. SWIR reflectance has been significantly correlated with moisture content in leaves in numerous studies (Fourty and Baret 1997; Ceccato et al. 2001; Sims and Gamon 2003; Kim et al. 2015), thus the changes in SWIR reflectance found in this study are expected as needle moisture content of needles decreases in attacked trees. The observed increase of GA reflectance over a large portion of the SWIR spectrum (~1200-2500 nm) is consistent with SWIR response in other GA research (Sharma 2007; Cheng et al. 2010; Fasnacht et al. 2014; Niemann et al. 2015) and with research examining vegetative dehydration due to various stress agents as well (Carter 1993; Cao et al. 2015; Kim et al. 2015).

In this study, the spectral regions that best discriminated groups are associated with moisture absorption features centered at approximately 1450 nm and 1920 nm (Table 3.5). The most consistent bands are located along the right edge of the 1450 nm absorption feature with overlaps in peaks of each statistical parameter from 1482-1501 nm. These bands are part of a larger region from 1451-1533 nm that overlapped in at least six parameters and from 1534-1540 nm with at least overlap in five parameters. Additional bands associated with this absorption feature and showing consistent discrimination over multiple parameters are located from 1418-1424 nm and 1586-1617 nm. The right edge of the moisture absorption feature at 1450 nm has been noted by other

moisture stress and GA studies. Fassnacht et al. (2014) noted a band at 1532 nm was stable for separating damage classes. Kim et al (2015) found the highest sensitivities to moisture stress at 1470 nm. This region has been correlated to moisture content of leaves in numerous studies as well (Carter 1993; Fourty and Baret 1997; Sims and Gamon 2003; Cao et al. 2015). However other GA studies show lack of separation with the 1450-1540 nm spectral range selected in this study (Cheng et al. 2010; Niemann et al 2015). Cheng et al. (2010) found bands located along the upper left edge (1318-1322 nm) of the 1450 nm absorption feature best separated GA and NA trees. The authors also noted that trees which had been girdled (bark cut through around the circumference) to simulate MPB damage had more pronounced water stress than GA trees and features that best correlated with moisture changes shifted to the right edge (~1550-1600 nm) of the 1450 nm feature. Given the later acquisition date, it is likely GA needles collected in this study are similar to the girdled trees dataset used by Cheng et al. (2010), which potentially explains the importance of the bands along the right edge of the 1450 nm moisture absorption feature. When tree water content is higher, reflectance sensitivity to moisture stress is greater at wavelengths with lower moisture absorption, but is vice versa for low moisture content (Sims and Gamon 2003; Kokalay et al. 2009; Ustin et al. 2012). Since the right edge of the 1450 nm absorption feature has higher absorption coefficients compared to the left edge (Gao and Goetz 1990; Sims and Gamon 2003), the observed importance of bands in this region is expected with that of plants with more severe water stress. This relationship between SWIR wavelength sensitivity and severity of water stress potentially explains research looking at earlier GA damage

Table 3.5. Summary of statistical analysis results. Notable regions of importance for each statistical parameter examined including peak wavelengths in parentheses. Notable overlaps in these regions are aggregated and reported at the bottom of the table.

Analysis	Statistical Parameter	Reference Figure/Table	Notable regions of importance – listed in order of relative importance	
			VNIR (Peak Values)	SWIR (Peak Values)
Group Differences	Mean Differences	Figure 11	588-707 nm with 680-699 nm subset (692 nm); 474-523 nm (504); 736-794 nm (751 nm)	1326-1694 nm with 1381-1420 subset (1398-1400 nm); 1753-1900 nm (1874-1876 nm); 1991-2038 nm (2012 nm)
	Variance Overlap	Figure 10	587-700 nm (687 nm); 464-521 nm (504 nm)	1383-1561 nm (1405 nm); 1845-1905 (1881 nm); 1976-2045 nm (2011 nm)
	Effect size – Pearson's <i>r</i>	Figure 13	575-698 nm (673 nm) 457-519 nm (486 nm)	1451-1541 nm (1491 nm) 1994-2045 nm (2010 nm)
Stepwise Linear Discriminant Analysis	Structure Coefficients	Figure 14	650-691 (675 nm); 462-516 (496 nm)	1418-1672 (1533 nm); 1982-2292 (2089 nm); 2293 – 2400 nm (no distinct peak); 1747-1821 nm (1761 nm)
	LOOCV classification accuracies	Figure 15	663-689 nm (667-669;683 nm); 521-527 nm (522-523 nm)	1389-1424 nm (1392;1404-1409 nm); 1586-1617 nm (1586-1587nm, 1593-1595 nm); 2062-2103 nm (2065; 2069; 2080-2082; 2086; 2089-2094 nm); 1482-1501 nm (no peak); 1768-1778 nm (no peak)
Per waveband Linear Discriminant Analysis	Wald $\chi^2$	Figure 16	650-675 nm (662 nm); 486-507 nm (503 nm)	1451-1550 nm (1497 nm); 1973-2114 nm (2043 nm)

Table 3.5. Summary of statistical analysis results cont.

Logistic Regression	Per Waveband LOOCV classification accuracies	Figure 17	670-697 nm (693 nm); 583-650 nm (617 nm); 519-526 nm (520 nm); 453-464 nm (464 nm)	1883-1899 nm (1891 nm); 1477-1553 nm (1493-1498 nm); 1430-1476 nm (1447 nm); 1384-1399 nm (1385 nm); 1972-1976 nm (1975 nm); 2023-2047 nm (2043 nm)
	Odds Ratio	Figure 18	430-520 nm (462-463 nm); 629-699 nm (675 nm)	1924-1951 (1941); 1892-1923 nm and 1952-2166; 1399-1653 nm (1464)
Random Forest	Mean Decrease in Accuracy	Figure 19	620-630 nm (627 nm); 653-687 nm (681 nm); 465-521 nm (471 nm)	1391-1540 nm with 1489-1527 nm subset (1491, 1489, 1493 nm); 1980-2035 nm (1997 nm); 1869-1893 nm (1884 nm)
Overlaps in wavebands – aggregate results			670-675 nm; 663-669 and 676-687 nm; 653-662, 688, 689 nm; 486-507 nm; 462-487 and 508-520 nm	1482-1501 nm; 1451-1481 and 1502-1533 nm; 1534-1540 nm; 1994-2045 nm; 2062-2103 nm; 1973-1993 nm 1418-1424 nm; 1586-1617 nm; 1885-1893 nm

(Cheng et al. 2010; Niemann et al. 2015) found better separation at shorter wavelengths in the SWIR than those in this study. In the Black Hills early spring precipitation is low and soils are still semi- to fully frozen, which could further induce water stress on trees and influence bands in this region as well. Although not examined in this study, it is assumed that environmental related water stress in trees would impact both the GA and NA trees similarly<sup>1</sup>.

After the 1451-1540 nm bands, the second most consistent spectral region with high discriminating ability was located along the right edge of an absorption feature at approximately 1900 nm. Bands from 1994-2045 nm had overlap in peak regions of five different statistical parameters (Table 3.5). These bands are a part of larger regions from 1973-1993 nm and 2062-2103 nm with overlap in peak regions of four parameters. Additionally bands on the left edge of this absorption feature, from 1885-1893 nm, also showed consistency in discrimination. While research indicates bands near the 1920 nm absorption feature are sensitive to moisture stress and GA damage (Carter 1993), they have not been as commonly identified as important for detecting GA damage (Sharma 2007; Cheng et al. 2010; Niemann et al 2015). As previously discussed, this is again likely due to the relationship between wavelength sensitivity and severity of moisture stress. In studies using earlier acquisition dates (Sharma 2007; Cheng et al. 2010; Niemann et al 2015), bands from 1900-2100 nm would be less likely to discriminate damage as they have higher water absorption coefficients thus are less effected by small

---

<sup>1</sup>Tree water stress induced by early spring precipitation minimums would occur in different seasons in other ponderosa pine forests in the U.S. Further west in the Cascades and Sierra Nevada precipitations minimums would be in the late summer/early fall and in the summer months in the Southern Rockies.

reductions in needle moisture (Kokalay et al. 2009; Ustin et al. 2012). The results consistently indicating discriminating ability of the 1900-2100 nm region observed in this study further confirms a more severe level of GA damage in this dataset. Cheng et al. (2010) also found correlations between bands in this region and girdled trees that had more severe moisture stress. Consequently, the utility of SWIR bands for remote detection of GA damage will be largely influenced by the progression of the water stress following an attack, based on the location of peak regions of discrimination observed in this study compared to those observed in GA research with earlier acquisition dates.

The GA sensitive bands from 1973-2103 nm also overlap with or are in close proximity to absorption features sensitive to leaf proteins, waxes, lignin and/or cellulose structures (Elvidge 1990; Curran 1989; Kokaly 2001; Kokaly et al. 2007; Wang et al. 2015). It is possible that changes in dry matter structures, due to water stress and tissue injuries caused by MPB infestations (Moura et al. 2010), could influence the spectral response of bands along the right side of the absorption feature at 1900 nm. Research has shown the influence of dry plant matter, such as lignin and cellulose, on reflectance from 2000-2500 nm is relatively weak in healthy green vegetation, but become increasingly more evident with plant desiccation (Elvidge 1990; Kokaly et al. 2007). In this study, the subtle absorption in the GA spectra at approximately 2100 nm (Figure 10) may indicate increased absorption due to increased concentrations of dry-matter structures (Elvidge 1990; Kokaly 2001; Kokaly et al. 2007) and would be consistent with the hypothesis that the spectral response of GA needles in this dataset is indicative of a more advanced GA damage compared to previous GA studies.

Although SWIR bands showed the best indications of discriminating ability, broad regions of the visible spectrum also indicated consistent differences between groups and may provide forest managers more flexibility since many currently available sensors have multiple bands in this range. Analysis of the VNIR dataset shows that GA reflectance is significantly higher than NA crowns from 424-717 nm (Figure 3.9 & 3.10). Increased reflectance in the visible bands is a consistent response in vegetation across numerous types of stress agents (Carter 1993; Carter and Miller 1994; Carter and Knapp 2001) and is primarily due to reductions in plant pigments following an attack (Carter and Knapp 2001; Sims and Gamon 2002).

In this study, VNIR peaks in discrimination were most consistently associated with bands in the blue and red regions of the spectrum. The bands that showed the most consistent discrimination are located from 670-675 nm, with overlap in the peak regions of discrimination for each of the statistical parameters examined (Table 3.5). This narrow region of bands is part of a larger group from 663-687 nm that overlap in at least six peak regions and from 653-689 nm with overlap in at least five peak regions. These bands are associated with a major chlorophyll absorption feature centered at approximately 675 nm. Similar consistencies in discrimination, with slightly smaller magnitudes of separation, were observed for bands associated with chlorophyll absorption in the blue to green-peak regions, with overlaps in five statistical parameters from 486-507 nm and for at least four statistical parameters from 462-520 nm (Table 5). The selection of bands associated with chlorophyll absorption maxima is inconsistent with most results from other hyperspectral GA studies. While some have observed bands in the blue and red spectra that

discriminate GA trees (Health 2001; Sharma 2007; Fassnacht et al. 2014; Niemann 2015), most previous research indicates bands that best isolate GA damage are located in the red-edge from approximately 690-750 nm and green-peak at approximately 550 nm (Murtha and Wiart 1989; Ahern 1988; Health 2001; Carter and Knapp 2001; Sharma 2007; Fassnacht et al. 2014; Niemann et al. 2015). Ahern (1988) even noted that bands in the red absorption maximum (667-686 nm) could be used as reference bands to eliminate confounding variables due to indifference between GA and NA trees.

Research examining vegetative stress generally finds peak differences and spectral sensitivities to various stress agents in the red-edge and green-peak regions as well (Carter 1993; Carter and Miller 1994). While significant discrimination was observed in the green-peak area and lower wavelengths of the red-edge in this study, it was consistently lower than discrimination in the blue and red regions. These results might be explained by the later collection date of this study compared to other GA research, thus differences in the severity of the GA damage. The blue and red spectrum have high pigment absorption coefficients and similar to moisture features in the SWIR, the spectral regions that have high pigment absorption coefficients are generally insensitive to changes because lower concentrations in pigments have strong enough absorption to still saturate the regions (Blackburn 1998; Carter and Knapp 2001; Blackburn 2007). Thus increases in the severity of chlorophyll loss must happen for reflectance changes to manifest in the blue and red wavelengths (Carter and Knapp 2001).

Peak discrimination in the blue and red wavelengths observed in this study are consistent with reflectance changes following severe chlorophyll reductions. Cheng et al.

(2010) also observed correlations in the blue and red regions for a more severely damaged girdled tree dataset. A further indication of more developed GA damage might be the dip in discrimination at the green-peak. Lower separation in the green-peak bands relative to blue and red bands might indicate increased concentrations of anthocyanin pigments which have absorption maximums near the green-peak (Gitelson et al. 2001). Anthocyanin pigments generally do not become dominant until more advanced stages of damage when chlorophyll and carotenoid pigments are severely degraded (Safranyik and Carroll 2006). Non-pigment factors such as moisture content (Carter 1993; Cao et al. 2015) and foliar nitrogen content (Kokalay et al. 2009) could influence reflectance in the visible spectrum as well but it is difficult to indicate importance of these using spectral response alone because they overlap with regions more heavily influenced by pigment absorption (Carter and Knapp 2001).

As previously mentioned, wavelengths along the red-edge have been consistently correlated with chlorophyll concentrations and are used to detect plant stress (Carter 1993; Carter and Miller 1994; Filella and Penuelas 1994; Blackburn 1998; Carter and Knapp 2001). Increased reflectance at the base of the red-edge because of decreased chlorophyll content shifts the red-edge of stressed plants to shorter wavelengths, commonly called a blue-shift (Carter 1993; Filella and Penuelas 1994; Blackburn 1998; Carter and Knapp 2001). While most GA research has observed a blue-shift in GA trees (Carter and Knapp 2001; Niemann et al. 2015), other research has noted red-shifts for GA trees (Ahern 1988). In this study GA trees had significantly higher reflectance at the base of the red-edge indicating a blue-shift in the red-edge. However, the usefulness of the

red-edge bands for remote detection is likely low based on these results. Differences between groups at the base of the red-edge are relatively small compared to other regions and become insignificant along the center of the red-edge (Figure 3.9). As the red-edge rises into the NIR shoulder, the influence of chlorophyll becomes negligible around 750 nm, and leaves internal structure and moisture content become the main drivers of reflectance sensitivity (Carter and Knapp 2001; Foley et al. 2006). Further analysis using reflectance derivatives may help to better understand the significance of red-edge changes in GA trees.

None of the bands in the NIR plateau showed indications of discrimination and had similar mean reflectance values for both groups with large amounts of overlap in variance (Figure 3.8). The similarities in NIR reflectance maybe due to the inverse nature of NIR spectral response associated with changes in internal leaf structure and moisture content following a MPB attack. As stress develops internal structures degrade reducing refractory surfaces in the form of intercellular spaces and air-water interfaces causing a reduction in reflectance (Foley et al. 2006). Conversely, increased dehydration in plants lowers moisture absorption and potentially increases NIR reflectance (Foley et al. 2006). Given the indications of more severe GA stress observed in the SWIR and visible bands, it is possible that increases in NIR reflectance due to moisture loss in GA trees is negated by decreases related more pronounced changes in internal leaf structure changes. Murtha and Wiart (1989) came to similar conclusions to explain spectral overlap between GA and NA trees in the NIR plateau.

This situation might also explain why some GA research with earlier collection dates observed significant increases in the NIR reflectance of GA trees (Ahern 1989; Niemann et al. 2015). These confounding effects could also explain why moisture absorption features in the NIR plateau and lower portions SWIR dataset did not show strong discrimination in this study but have shown sensitivity to GA damage in studies with earlier acquisition dates (Cheng et al. 2010; Fassnacht et al. 2014; Niemann et al. 2015). Research attempting to estimate vegetation moisture have also noted the confounding effects of moisture and internal structures in the NIR and lower wavelength SWIR bands (Aldakeheel and Danson 1997; Ceccato et al. 2001).

### **3.5 Implications for Remote Sensing and Management**

The results of this study possess numerous implications relative to detecting GA damage using aerial or satellite platforms. Compared to GA research with fall measurements, sensitivity to damage was observed over wider portion of the visible and SWIR spectrum. This potentially widens the scope of sensors and platforms available for detection and might allow managers more flexibility in selecting sensors with temporal, spatial, and spectral resolution that better match the characteristics of an infestation. Furthermore, information provided by this study provides a foundation for the development of spectral indices to further enhance operational remote detection of GA damage by combining information from damage sensitive bands in the visible or SWIR range with insensitive bands in the NIR.

The results of this study indicate that wavelengths in the SWIR offer the best potential to discriminate GA and NA damage classes. This opens up the potential for use of many contemporary airborne hyperspectral sensors (HyMap, AVIRIS) and satellite sensors (WorldView-3, Landsat-8, ASTER) that have bands located in the SWIR spectrum. With respect to the SWIR bands, when interpreting results for canopy level detection methods, atmospheric water vapor absorption needs to be considered. Atmospheric scattering due to water vapor strongly influences wavelengths from approximately 1350-1450 nm, 1800-2000 nm and 2400-2500 nm (Gao and Goetz 1990; Sims and Gamon 2003; Thenkabail et al. 2004). Using bands located within or near these wavelengths can increase noise in the spectral response of the tree crowns. Therefore, obtaining data when clear skies prevail and dew points are low is strongly recommended. The utility of bands along the right edge of the 1450 nm and 1900 nm absorption features could be negatively impacted by atmospheric scattering. When accounting wavelengths with high atmospheric absorption coefficients (Gao and Goetz 1990), the SWIR bands that maybe most useful for GA detection are located from approximately 1486-1540 nm and 2000-2103 nm. Within the Black Hills, late winter/early spring collection dates would have a benefit of drier atmospheres as dew points and humidity are low. While not specifically discussed due to falling outside the peak values, additional SWIR bands from 1541-1799 nm and 2104-2400 nm also showed consistently high separation between groups and are located in windows with low atmospheric absorption (Gao and Goetz 1990; Sims and Gamon 2003) making them potential candidates to be utilized to detect GA damage as well. Additionally, localized differences in atmospheric aerosols can

negatively impact the generalization of results from leaf-level studies to the canopy and make atmospheric correction a necessity (Gao and Goetz 1990; Kokaly et al. 2009).

It is unknown if separation between GA and NA observed at the needle level can be scaled-up to effective canopy-level detection. Regions with good separation have large variance in GA reflectance values and overlap with NA needles (Figure 10), which would make accurate classification difficult. Previous GA detection attempts have also observed high GA variance and overlap with healthy trees as the main cause for low classification accuracies (Murtha and Wiart 1989; Heath 2001; Fassnacht et al. 2014). Optically thick needle stacks used in this study better to represent canopy structure, but have also been shown to exaggerate reflectance (Kokaley et al. 2009), could be a source of uncertainty when generalizing results from this study. Sims and Gamon (2003) found that moisture content is more accurately estimated at the canopy-level compared to needle-level measurements. Based on their results, the SWIR bands that best discriminated damage classes in this study could potentially be more sensitive to damage at the canopy-level and improve detection accuracies. A certain degree of uncertainty in scaling results to canopy-level is also expected due to the inclusion of background elements within a pixel which would reduce the signal of tree crowns.

There are temporal related issues that may limit the effectiveness of remote detection of GA damage in the late winter/early spring. Relative to late summer/early fall collections, late winter/early spring acquisition dates will have lower solar zenith angles which can: (1) alter the spectral response of vegetative (Kollenkark et al. 1981), (2) increase shadows in an image, and (3) increase atmospheric scattering as solar radiation

has to pass through a greater portion of the atmosphere. Early detection dates increases the chances of snow cover, especially in mountainous regions, which can contaminate pixels. In western North American cloud cover fractions are greater in the early spring compared to the summer dates (NASA Earth Observation 2016), reducing the likelihood of acquiring cloud free images.

Within the Black Hills, late winter/early spring GA detection faces a narrow but attainable acquisition window. Images must be acquired late enough that snow cover is minimal but early enough to allow for images to be processed and analyzed in a timely manner for mitigation of infected trees to take place before the broods take flight. In the Black Hills methods such as cut-and-chunk, in which attacked trees are felled and cut into small chunks to dry out, need to be completed by March 1<sup>st</sup> to be effective and chemical spraying of NA trees usually needs to be completed by June 1<sup>st</sup> (USDA Forest Service 2010). Given these deadlines, remote sensing of GA damage in the late winter/early spring is well suited for implementing proactive mitigation such as forest thinning along leading edges of infestations in later spring/early summer.

### **3.6 Summation**

Green-attack reflectance was significantly higher than NA trees from 424-717 nm and 1151-2400 nm. Increases in GA reflectance are likely due to decreased pigment absorption following chlorophyll degradation in the visible bands and water absorption in the SWIR bands. No notable separation was observed for bands along the upper red-edge and NIR plateau. In general, bands located in the SWIR spectrum (~1390-2400 nm)

showed increased discrimination of GA from NA trees compared to bands in the visible and NIR spectrum.

Within the SWIR spectrum, this study identified two regions of bands, from approximately 1451-1540 nm and 1973-2103 nm, that show the most promise for detection of GA damage with remotely sensed imagery. Spectral response of GA trees in these regions is consistent with those following severe moisture losses in vegetation. Bands in the visible spectrum also showed consistent separation and are likely useful for remote sensing of GA damage as well. Bands associated with chlorophyll absorption features in the blue –green (462-520 nm) and red (663-689 nm) provided greater measures of discrimination than other visible bands.

It is unknown if these results can be scaled up to canopy level detection at rates that are operationally viable. Large within-class spectral variability, spectra; overlap between groups, and canopy variability can negatively impact classification using imagery datasets. The regions in the SWIR showing the most promise are located near wavelengths affected by atmospheric water vapor scattering. Later winter/spring collection dates have increased technical obstacles for quality imagery and shorten the time between collection and deadlines for mitigation. However, later collection allows for greater stress development and greater separation between groups, which will likely provide more reliable detection of GA trees.

## **4. Early Detection of Mountain Pine Beetle Attacked Trees using WorldView-2**

### **Imagery and Field Data**

#### **4.1 Introduction**

To effectively inventory the spatial extent of MPB green-attack damage and apply mitigation strategies, forestry officials need to detect tree stress with high accuracies at large spatial scales before next seasons broods take flight. Ground-based assessments provide the most reliable results of GA detection. However, ground-based assessments are not well suited for large scale mapping and fail to provide enough coverage to mitigate the problem. Remote sensing data sources can provide information that meets the temporal and spatial needs of early MPB damage detection. This chapter focuses on the use of high spatial resolution multispectral imagery to detect MPB GA trees. While the narrow bandwidths of hyperspectral data examined in the previous chapter may better characterize spectral response of GA tree crowns, it is unknown if that information can be scaled to canopy level detection using satellite platform sensors. The availability of hyperspectral satellite sensors is limited and those available do not have the spatial resolution needed to capture the spectral response of individual tree crowns. Aerial based hyperspectral sensors have high acquisition costs and require a large number of images to capture comparable scene coverage to satellite sensors, increasing the amount of image processing needed. Alternatively, numerous multispectral satellite sensors provide spatial resolutions that can distinguish single tree crowns. However, they generally have coarser

spectral resolutions increasing the likelihood that a subtle spectral response will be masked out of the signal.

Recently developed multispectral satellite sensors provide forest officials with options that have the spatial and potentially the spectral resolutions needed to detect GA damage with high accuracies. The WorldView-2 (WV-2) operated by Digital Globe® has a sub two-meter spatial resolution and has a unique spectral resolution. Traditional visual broad bands are located in the blue, green, red, and NIR portions of the spectrum. The WV-2 sensor has additional bands in the lower blue, yellow, and red-edge regions along with an additional NIR band. Previous GA and vegetation stress research has indicated the importance of some of these bands, especially the red-edge, in detecting stress related changes such as pigment degradation (Ahern 1989; Carter 1993; Carter and Miller 1994; Carter and Knapp 2001).

Since its launch in 2009 the WV-2 platform has been used in numerous studies looking at detecting forest disturbances (Filchev 2012; Penuel and Mutanga 2013; Immitzer and Atzberger 2014; Waser et al. 2014; Murfitt et al. 2016). Immitzer and Atzberger (2014) were able to detect GA damage due to spruce bark beetles in Norway spruce trees with an overall accuracy of 73.7%. These accuracies are slightly better than achieved using aerial (Health 2001; Fassnacht et al. 2014) and satellite (Sharma 2007) hyperspectral sensors to detect MPB GA damage. In a review of GA detection research, Wulder et al. (2009) noted two of the biggest obstacles to successful GA detection have been spectral similarities between GA and NA trees and the inclusion of background elements within a single pixel diminishing the response of tree crowns.

The very high spatial resolution of WV-2 imagery can help alleviate the latter of these problems. The former maybe due to data acquisition dates of GA research being in the summer/early fall following the initial attack (Ahern 1988; Murtha and Wiart 1989; Carter and Knapp 2001; Cheng et al. 2010; Fassnacht et al. 2014; Immitzer and Atzberger 2014; Niemann et al. 2015). If the onset of biophysical stress within attacked trees is too subtle, the spectral differences between GA and NA trees may not allow for accurate discrimination between the two classes in the fall, which can lead to high rates of GA omission. Late winter/early spring acquisition dates would allow more time for stress and subsequent spectral changes to develop. However there are disadvantages to late winter/early spring acquisitions due to risk of snow cover, shorter days, and increased cloud cover which could reduce collection windows. These problems can be alleviated as the WV-2 satellite has a temporal resolution of 1.1 days, increasing the opportunities for acquiring desirable imagery.

The goal of this study is to examine the potential for WV-2 data collected in the late winter/early spring to detect and classify GA damage. To reach this goal, research focused on two objectives: 1) comparing the spectral responses of GA to NA trees and 2) identify which WV-2 bands or indices reliably discriminate GA trees using multiple statistical methods. Identifying spectral variables important in detection can potentially cut down on data redundancy, processing times, and costs. To address the second objective, the performances of three different classifiers (logistic regression, linear discriminant analysis, and Random Forest) were examined using various groupings of predictor variables. These groupings of predictor variables are selected using stepwise

selection methods and examination of correlation tables. If successful, these methods could provide forest officials with an operational method for accurately detecting GA damage and improve the effectiveness of mitigation and assessments of current damage impacts.

#### **4.1.1 Study Site**

Located in the east-central portion of the Black Hills region in Southwestern, SD (Figure 4.1) and covering 34,225 acres, the Norbeck Wildlife Preserve (43° 50' 53" N, 103° 27' 39" W) area was chosen based on discussion with USFS officials located at the Forest Supervisor's Office in Custer, SD. The study site is located along the leading edges of two large infestations and was accessible by roads and trails at the time of the field visit. The reserve was set aside in 1920 to be managed as habitat for game animals, with the Black Elk Wilderness area designated in 1980 under the Wilderness Act of 1964 (Continuing Education in Ecosystem Management Group 2006). The preserve boundary includes portions of Custer State Park to the south, Mt. Rushmore National Monument to the Northeast, and Black Elk Wilderness area located in the central area of the preserve. Elevations within the preserve range from 4,360-7,242 feet, with the topography dominated by narrow ridges and valley bottoms with steep slopes and granite outcrops (Continuing Education in Ecosystem Management Group 2006). Field data were collected in the east-central portion of the preserve along the southeastern border of the Black Elk Wilderness area approximately 2.5 miles south of Mt. Rushmore National Monument.

## 4.2 Methods

### 4.2.1 Field Data Collection

Figure 4.2 provides a flowchart that outlines the methodology used in this study. Field data were collected on March 7-8 and March 11, 2015 between 8:00 and 17:00. GPS locations for NA and GA trees were collected using a Trimble GeoXH with Terrasync connected to an external antenna. Differential corrections were done in real-time using an integrated space-based augmentation system. GA trees were selected if they showed signs of a successful beetle attack

(Figure 3.2 & 3.3) and had no visual signs of fading in the tree crown. NA trees were selected if they did not show signs of the attack and also had no fading in the tree crowns. To increase the likelihood that multiple image pixels align and overlay each sample location and reduce the inclusion of incorrect classes in the training data, tree locations were collected only from clusters of GA or NA trees (approximately >10 trees) that were mutually exclusive to one of the two damage classes.

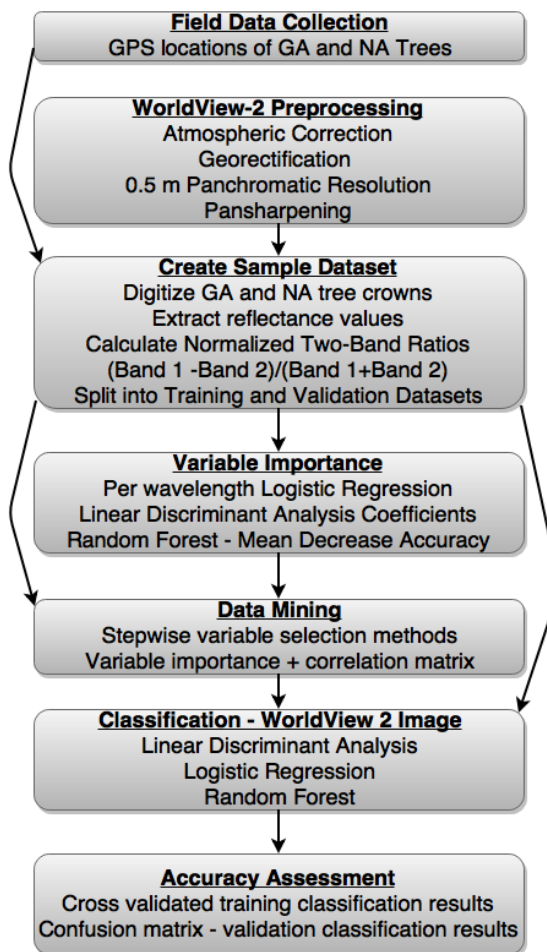


Figure 4.2. Flowchart outlining methodology.

#### **4.2.2 WorldView-2 Image Processing and Segmentation**

To provide coverage encompassing the field collection area, two WV-2 images were collected on April 9, 2015 under cloud-less conditions. In addition to covering the field data collection area, the image provides approximately 24,710 acres of coverage over large portions of the Norbeck Wildlife Preserved, including sections of the Black Elk Wilderness Area and much of the Mt. Rushmore National Monument area. The acquisition specifications of the two images are detailed in Table 4.1. The WV-2 satellite imagery has a high spatial resolution, 1.85 m for the multispectral bands and 0.5 m for the panchromatic band at nadir, and a unique combination of spectral bands. For example, in addition to the traditional blue, green, red, and NIR bands the WV-2 data has four bands located in the coastal, yellow, red edge, and NIR-2 regions (Table 4.2). These additional bands may be beneficial for the detection of beetle related tree stress as they are located in regions of the spectrum previously shown to be sensitive to MPB induced tree stress (Ahern 1989; Carter and Knapp 2001; Fassnacht et al. 2014; Niemann et al. 2015).

Both images were converted to at-sensor radiance values before atmospheric correction. In order to obtain spectral reflectance values that produce meaningful and transferable results to other data sets atmospheric correction was performed using the FLAASH 5.3 module with ENVI 5.3 software. The atmospheric correction module produced some saturation artifacts. To remove these from further analysis, pixels with values below 0% and above 100% reflectance were masked out of both images. The two

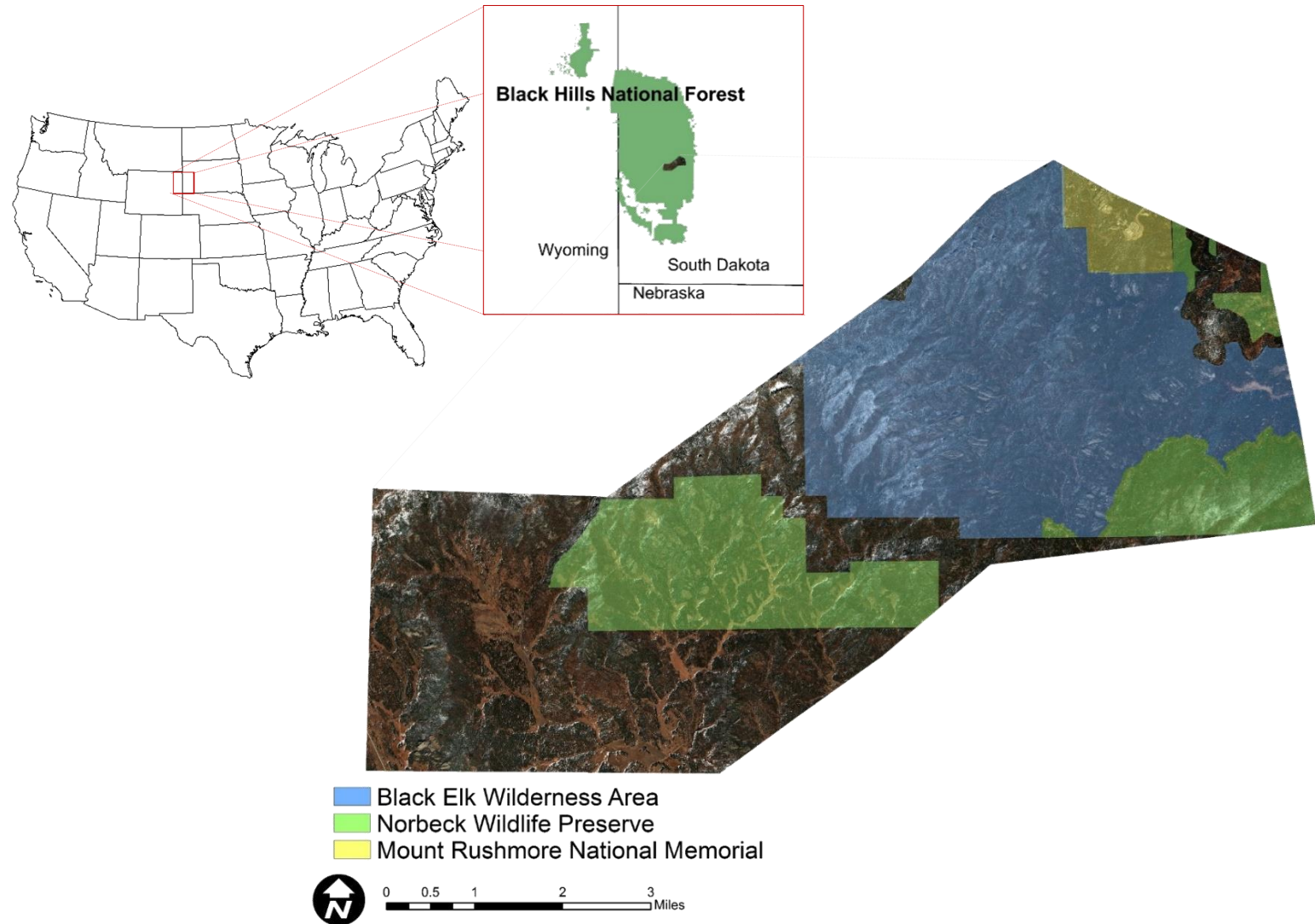


Figure 4.1. Study area and WorldView-2 image footprint. Pan-sharpened WorldView-2 image (5,3,2, RGB) and location of the study area with transparent administrative boundaries overlaid for reference. Inserts provide regional context of the study area.

Table 4.1. WV-2 image acquisition specifications

	<b>Image 1</b>	<b>Image 2</b>
<b>Acquisition Time</b>	17:56:16	17:26:55
<b>Scan Direction</b>	Forward	Reverse
<b>Mean Sun Elevation</b>	51.8°	51.8°
<b>Mean Sun Azimuth</b>	155.8°	156.0°
<b>Mean Satellite Elevation</b>	76.3°	73.4°
<b>Mean Satellite Azimuth</b>	142.6°	156.8°
<b>Mean off nadir view angle</b>	12.0°	14.6°

Table 4.2. Spectral resolution of WV-2 bands.

<b>WorldView-2 Band Spectral Resolutions</b>	
<b>Coastal: 400-450 nm</b>	Red: 630-690 nm
<b>Blue: 450-510 nm</b>	Red-edge:705-745 nm
<b>Green: 510-580 nm</b>	NIR-1: 770-895 nm
<b>Yellow: 585-625 nm</b>	NIR-2: 860-1040 nm

images were mosaicked using with the MosaicPro module in Erdas Imagine 2015 using histogram matching to account any differences in color, shading, and illumination between the two images. The multispectral WV-2 image was fused with the panchromatic image using Hyperspherical Color Space (HCS) algorithm. The pan-sharpened image served as a visual aid and as the input for green tree image segmentation. Pixel values on pan-sharpened WV-2 images have been showed to be highly correlated with the original multispectral image pixel values (Cho et al. 2015) and the HCS algorithm specifically maintains good spectral quality (Padwick et al. 2010). However, since the contextual features were not used in the variable selection, classification, or mapping methods to preserve the spectral quality of tree crowns, only the original multispectral image was used as for analysis and classification.

To automatically extract green tree crowns (both GA and NA trees) from the WV-2 image, an object based classifier was chosen. When used with high spatial resolution datasets, object based classifiers yield higher accuracies than traditional pixel-based methods when classifying vegetation (Yu et al. 2006). This process can be particularly useful when trying to segment large numbers of small features such as pine tree crowns.

Segmentation was performed using the Feature Analyst 5.1 extension for ArcMap 10.3. Training polygons were created using tree crowns from both the GA and NA classes to minimize the between class variance of the two classes. Tree crowns were digitized on the panchromatic image if they showed no signs of fading in the multispectral image. After multiple iterations using different settings, a Natural Feature selector using a three pixel wide bull's eye pattern as the input representation yielded the best results. A vector shapefile representing green trees was exported and later used as a mask to eliminate unneeded landcover types from classification and mapping. The green tree segmentation had an overall accuracy of 85% and a user's accuracy of 100%, indicating all of the extracted pixels represent green tree crowns.

#### **4.2.3 Sample Dataset**

GA and NA tree locations collected during the field visit were overlaid on the WV-2 multispectral and panchromatic images to delineate the GA and NA tree crowns. Since there was approximately a one month time lapse between the field visit and the WV-2 image acquisition, attention was given to make sure no noticeable yellow fading was apparent in tree crowns within the polygons on the multispectral image. Individual sunlit tree crowns are readily discernable on the 0.5 cm resolution panchromatic image. As such, the panchromatic image was used to manually digitize sunlight crowns from both GA and NA trees if they were located within each class's respective field collected polygons and had no visual fading in the multispectral or pan-sharpened images.

To further verify GA status of tree crowns, Google Earth imagery (Map Data: Google, DigitalGlobe) from the fall following WV-2 image acquisition was used to inspect whether GA trees had faded. Only sunlight portions of crowns were selected to mask-out and reduce the effect of tree shadows in analysis. Within some polygons spacing between tree crowns was compact enough that the sunlight crowns of multiple trees overlapped and were included within a single reference tree crown. Figure 4.3 gives an example of this process.

A total of 291 GA and 414 NA tree crowns were delineated and converted to shapefiles in ArcMap 10.3. These delineated tree crown shapefiles were used to extract the reflectance values from the multispectral image and averaged together for each tree crown polygon. This object based approach has been shown to yield better classification results compared to using per pixel reflectance values alone (Immitzer et al. 2012). A total of 4,697 pixels representing GA crown damage were extracted with each GA crown polygon representing a median value of 12 pixels. A total of 2,626 pixels representing NA tree crowns were extracted with each crown encompassing a median value of six pixels. The discrepancy between the number of pixels for GA and NA tree crowns is likely due to GA damage in stands characterized by high tree densities, which provide favorable conditions for beetle infestations, thus increases the probability that multiple sunlight tree crowns are included in a single reference polygon.

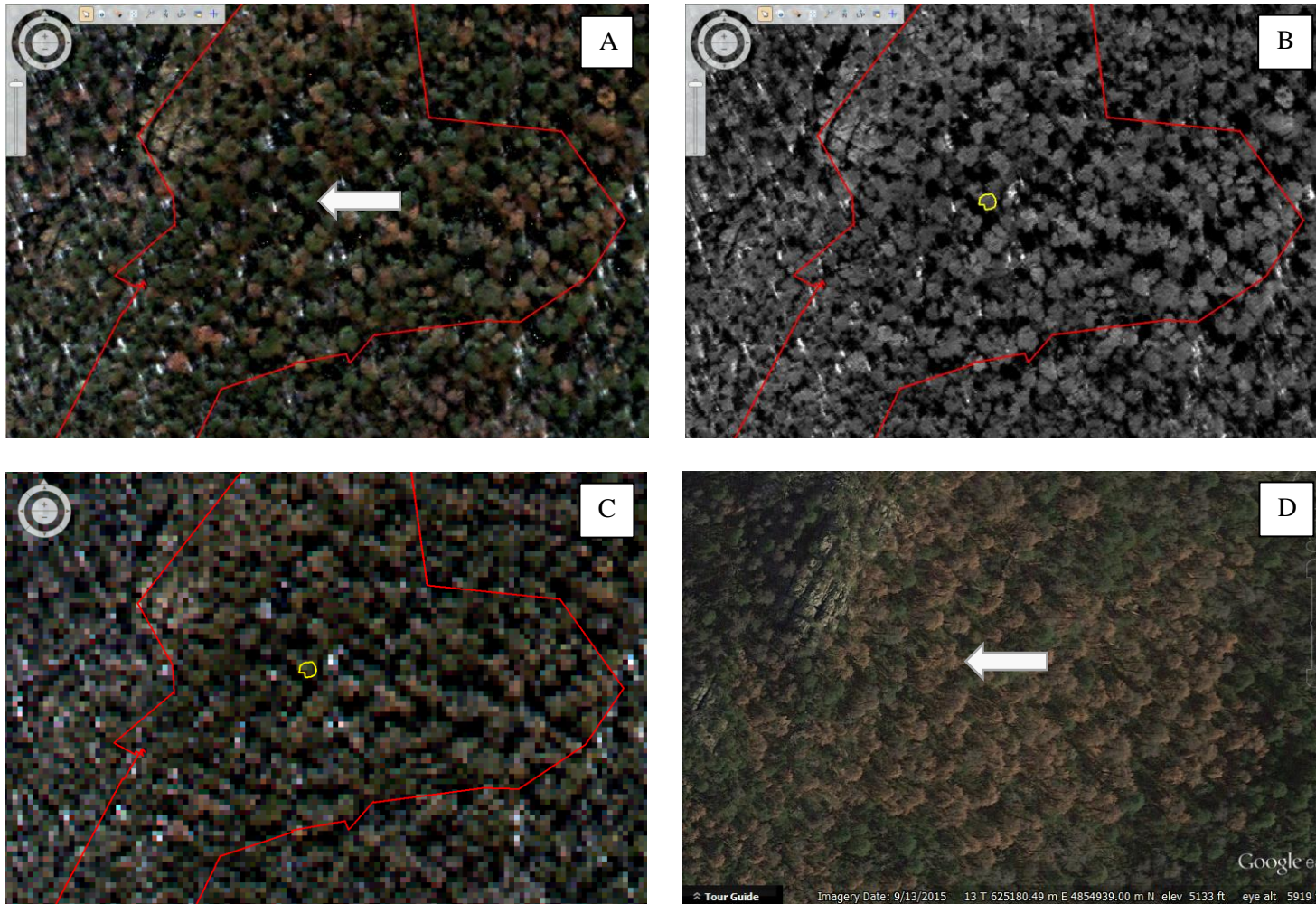


Figure 4.3. Example of manual delineation of tree crowns. Still green GA tree crowns (arrow) within field data polygons (red) identified on the pan-sharpened image (A) and sunlit crowns were delineated (yellow) on the panchromatic image (B). Pixel values were then be extracted from the multispectral image (C). Google earth imagery was examined to confirm GA trees (D). Map data: Google. Digital Globe.

#### 4.2.4 Spectral Predictor Variables

Reflectance values were extracted for all eight WV-2 spectral bands using the reference polygons. The mean value of pixels within each individual tree crown polygon was calculated and normality was assessed using a Shapiro-Wilk test (Appendix B). Spectral reflectance signatures were created using the mean reflectance values of all GA and NA tree crowns for each WV-2 band. Within- and between-class variability was assessed using the reflectance signatures and median reflectance box-plots.

In addition to the WV-2 bands, normalized two-band indices were also used as predictor variables. Normalized two-band indices were created using all possible WV-2 band combinations with following equation:  $(R_y - R_x) / (R_y + R_x)$ , where  $R_y$  is reflectance in band  $y$  and  $R_x$  is reflectance in band  $x$ . Numerous vegetation indices (VIs) have been developed and correlated with different phenological stages and levels of tree stress. Indices can be better indicators of damage stress compared to single band reflectance alone because they combine information from multiple bands and emphasize differences between GA and NA classes. For example one of the most widely used VIs, the normalized difference vegetation index (NDVI), uses NIR bands sensitive to chlorophyll changes and red bands that are insensitive to changes to maximize vegetation response. Immitzer and Atzberger (2015) found that normalized two-band ratios improved classification accuracies compared to single bands when mapping insect disturbances in spruce stands with a WV-2 dataset. For simplicity in reporting, normalized 2-band combinations will be referenced as Band  $Y$ -Band  $X$  to indicate the combination of bands

used in a particular normalized index. The eight spectral bands plus normalized two-band indices gave a total of 36 spectral variables that served as potential predictor variables.

#### **4.2.5 Variable Importance and Data Mining**

To compare the spectral responses of GA to NA tree crowns and identify which spectral variables are most important for separating classes, this study used four statistical approaches. A Mann-Whitney- $U$  test was used to examine the null hypothesis that there were no significant differences between the GA and NA crowns. This non-parametric test was chosen because only one spectral variable had a normal distribution for both the GA and NA damage classes and all but eight spectral variables had non-normal distribution for either damage class (Shapiro-Wilk,  $p < 0.05$ , Appendix B). A Pearson's correlation coefficient  $r$  value was calculated for each spectral variable to determine the effect size of differences between the classes (Rosenthal 1991). For interpretation, effect sizes with  $r$ -values above 0.1 are considered small, above 0.3 are moderate, and above 0.5 are large effects (Cohen 1988).

The discriminatory power of each spectral variable was examined using logistic regression (LR) analysis with individual spectral variables iteratively used as predictors and assessed using the leave-one-out cross validation (LOOCV) classification accuracies for each spectral variable. LR was chosen because it is a parametric classification method, allows for a categorical binary dependent variable, is robust against violations of assumptions, and allows for single variables to be used as inputs to the model. The remaining two approaches use internal estimates of importance for classification models

using all 36 predictor variables as inputs. First of these internal estimates are the factor structure coefficients between each predictor variable. These coefficients are the correlation between a particular variable and the discriminant function. High correlations with the discriminant function indicate a spectral variable has greater ability to discriminate classes. The second statistic is the mean decrease in accuracy (MDA) if a variable is left out of Random Forest (RF) classification. Higher MDAs indicate a greater importance a particular spectral variable has in RF classification.

Data mining and variable reduction can potentially yield more parsimonious classification models without sacrificing accuracy. Reducing data redundancy can lessen multicollinearity between variables used as model inputs, which possibly improves accuracies and transferability of models. Furthermore, it can cut down on the processing time and power needed to classify large datasets. In this study three data mining techniques were examined. The first method was a stepwise LR method, which adds or subtracts variables to minimize the models Akaike's information criterion (AIC) until it can no longer be significantly minimized. Second, a stepwise linear discriminant analysis (SDA) which selects or removes variables based on minimizing the Wilk's Lambda. Lastly, using the indicators of variables importance and examining a variable correlation matrix, predictor variables that best discriminant the two classes and had the lowest correlations with other important variables were selected. Stepwise LR was done using 'R' v.3.2.4 (R Core Team 2016) with R package 'caret' v.6.0-64 (Kuhn 2016). SDA and correlation matrices were done in SPSS® v. 22. For both the data mining and variable

importance statistical methods the entire sample dataset (GA= 291; NA=414) were used for analysis.

#### 4.2.6 Classification and Validation

Two-thirds (GA=194; NA=276) of the sample dataset was split to serve as training data for the classification models and one-third (GA=97; NA=138) was used for validation purposes. Spectral variables were grouped into five different sets of predictor variables to serve as inputs for the classification models (Table 4.3). Groupings include one with all 36 predictor variables, another with only the eight WV-2 bands and three additional groupings based on the results of the data mining techniques. To separate tree crowns into GA or NA classes, LR, linear discriminant analysis (LDA), and RF classification algorithms were examined. LR was chosen to provide a linear model that handles non-parametric data. LDA classification is a powerful classifier, but is more susceptible to violations to data assumptions. It is a commonly applied method in remote sensing studies and was included in this study to see if it could handle the non-parametric

Table 4.3. Groupings of predictor variables used for classification. Groupings 3-5 represent the variables selected as part of the data reduction methods.

	<b>Description</b>	<b>Predictor Variables</b>
<b>Grouping 1</b>	All WV-2 Extracted Variables	8 WV-2 bands + 28 normalized two-band ratios
<b>Grouping 2</b>	WV-2 Bands	8 WV-2 bands
<b>Grouping 3</b>	Selected by stepwise logistic regression	Blue + Yellow + Red Edge + NIR 1 + Green-NIR 1 + Blue-NIR 1 + Green-Red + Red-NIR 2
<b>Grouping 4</b>	Selected by stepwise discriminant analysis	Yellow + NIR1 + Green-Red + Green-NIR 2 + Yellow-NIR 1 + Red-NIR 2
<b>Grouping 5</b>	High variable importance and low correlations	Red Edge-NIR 1 + Yellow + NIR 1 + Yellow-NIR 1 + NIR2 + Coastal-NIR 1

data. RF classification was chosen because it has shown to be faster, more robust, and requires less analyst guidance compared to other popular classification algorithms, while providing comparable or better results (Ham et al. 2005; Gislason et al. 2006; Chand and Paelinckx 2008; Rodriguez-Galiano et al. 2012; Immitzer and Atzberger 2014).

The RF classifiers were created using 1000 classification trees (ntree parameter) and two predictor variables at each tree split (mtry). Performance of these classifiers was compared using both cross-validated accuracies of the training data split and classification accuracies of the validation data split. Cross-validation of the training data was done using a LOOCV method for LR and LDA and the internal out-of-bag (OOB) method for RF. After model training, the validation data split was ran through each classifier and confusion matrices were created to compare model performance based on the user's accuracy, producer's accuracy, overall accuracy, and Cohen's kappa coefficient for each model. All classification was done in 'R' v. 3.2.4 (R Core Team 2016) with the following R packages, 'boot' version 1.3-17 (Canty and Ripley 2015), 'pscl' v. 1.4.9 (Jackman 2015), 'MASS' v.7.3 (Venables and Ripley 2002), and 'randomForest' v. 4.6 (Liaw and Wiener 2015). The classifiers with the highest cross-validated and independent dataset classification accuracies were applied to the entire WV-2 image masked with the green-tree segmentation shapefile to give a visualization of a final mapping product.

### 4.3 Results

#### 4.3.1 Spectral

##### Reflectance Signatures

Both the median and mean reflectance values of GA trees was higher than NA trees in the visible bands and lower in the red-edge, NIR-1, and NIR-2 bands (Figures 4.4, 4.5, & 4.6).

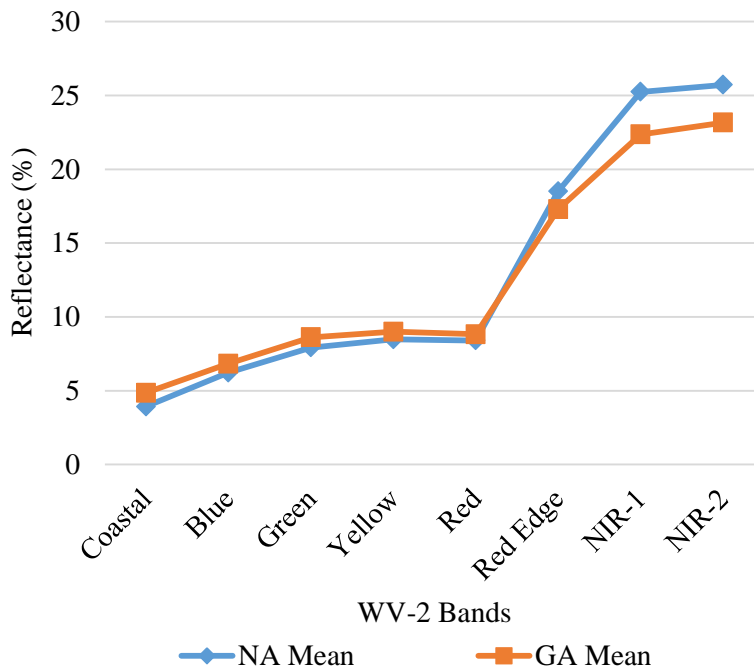


Figure 4.4. Mean reflectance values of NA and GA trees in each WV-2 band.

For each band, a majority of the within-class variances between classes overlap and all median values of GA and NA trees lie within the upper or lower quartiles of each other (Figure 4.6). In the visible

bands the GA class have

greater standard deviations (SD) compared to the NA class and both classes have similar within-class variances in the red-edge, NIR-1, and NIR-2 bands (Figure 4.6). A large majority of the classes had a non-parametric distribution for each spectral variable (Appendix B) and generally had more right skewed than left-skewed.

### 4.3.2 Variable Importance

The spectral responses of GA trees was significantly different than NA trees for all WV-2 bands (Figure 4.7; Mann Whitney-*U*:  $df=1$ ;  $p<0.05$ ). While significant, the effect

sizes of these differences were small ( $0.1 < r < 0.3$ ).

Spectral differences between GA and NA trees were greatest in the NIR-1 band followed by the NIR-2 bands. All of the visible bands had similar magnitudes of differences between the two classes, with the red and coastal bands slightly higher than the green, yellow, and red-edge bands. A majority of the normalized two-band indices separate the GA and NA classes, differences observed for 17 of the 28 indices (Figure 4.7; Mann Whitney-*U* ;  $df=1$ ; with significant  $p<0.05$ ). The normalized two-band index using the red edge and NIR-1 band had the greatest magnitude of difference between the two classes, with a medium effect size ( $r>0.3$ ). Relative to other indices, the normalized two-band indices utilizing a combination of the NIR-1 band and a visible band had the highest effect sizes, followed by NIR-2 bands or red-edge bands paired with visible bands.

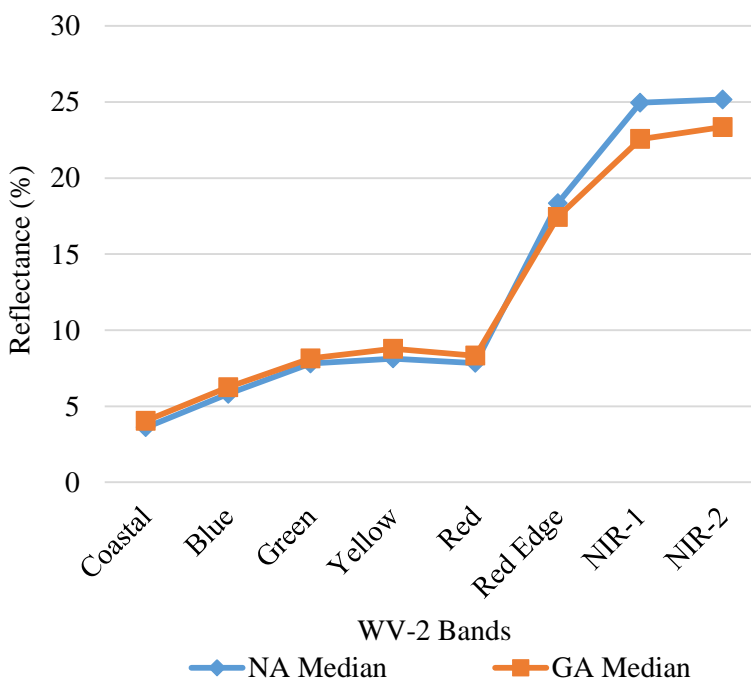


Figure 4.5. Median reflectance values of NA and GA trees in each WV-2 band.

Normalized two-band indices using two visible bands had non-significant differences between the two classes. Other than the NIR-1 and NIR-2 bands, normalized two-band ratios had higher effect sizes compared to the WV-2 bands.

LR classification models using single spectral variables ranged from 57.66% to 65.54% accuracies (Figure 4.8). Of the WV-2 bands, the coastal band produces the highest LOOCV accuracy (63.15%). The other visible bands had slightly lower but comparable accuracies to the coastal band and the red-edge band produced the lowest accuracy. Unlike class differences in which the two NIR bands had the highest magnitude of difference between GA and NA of the WV-2 bands, the accuracies of the NIR-1 and NIR-2 bands were lower than the visible bands. Use of normalized two-band indices in the equation improved accuracies compared to single WV-2 bands, with a max accuracy of 65.54% for the normalized two-band index using the NIR-1 and green band. Indices using a combination of a NIR band and a visible band had higher accuracies than combinations using two visible bands or two NIR bands.

Of the WV-2 bands, the NIR-1 band had the highest correlation with the LDA function using all spectral variables as inputs, followed by the coastal band (Figure 4.9). The correlation structure coefficient of the red-edge band has the lowest discriminatory power of the WV-2 bands. Several normalized two-band indices had higher correlations than the best WV-2 band (NIR-1). Similar to the effect size and LR accuracies, combinations utilizing one of the NIR bands and a visible band resulted in better discrimination.

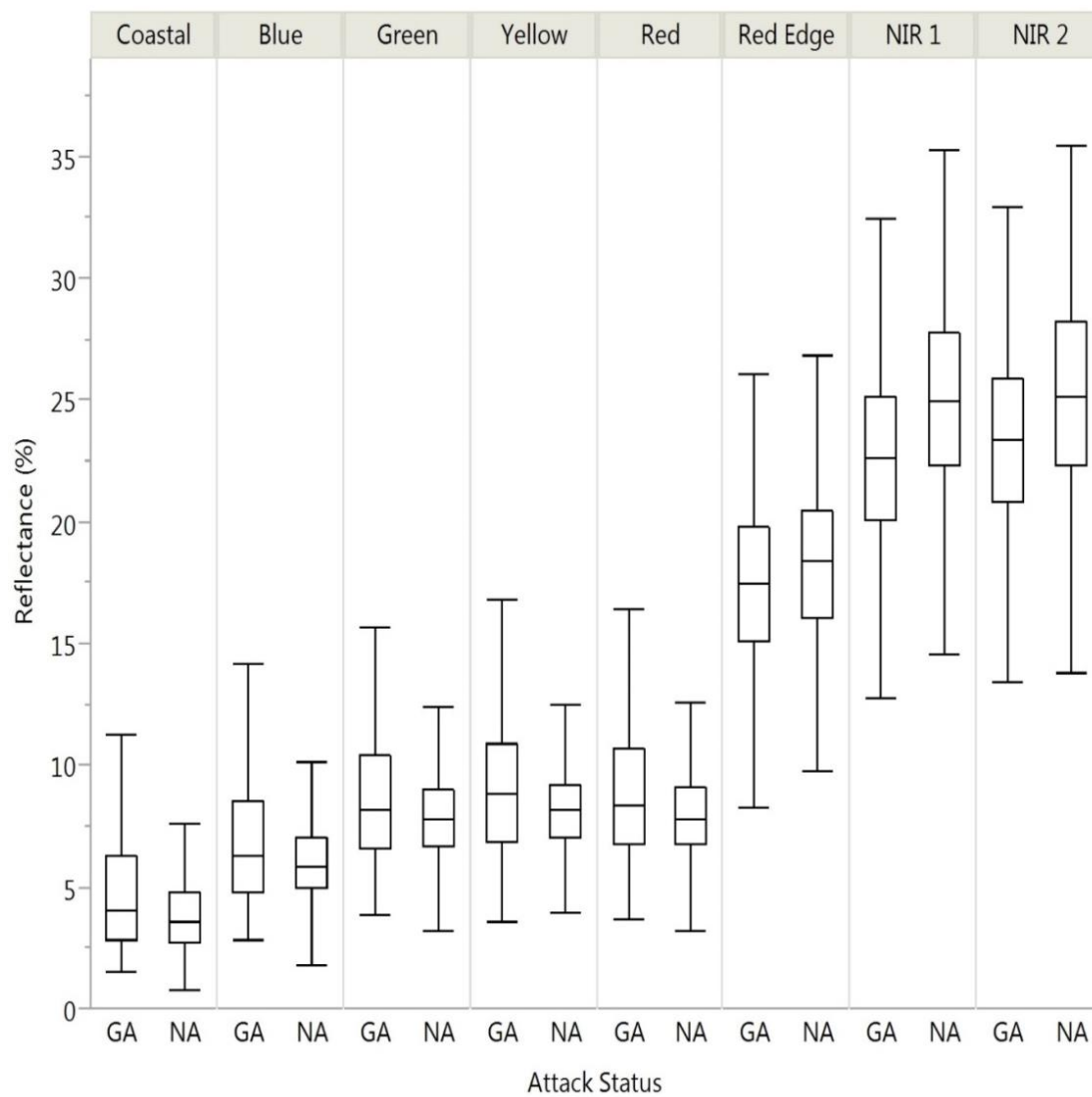


Figure 4.6. GA and NA box-and-whisker plots for each WV-2 band. Center lines are median reflectance values. The box is defined by the upper and lower quartiles of data. Whiskers are defined by the upper quartile  $\pm 1.5x$  the interquartile range.

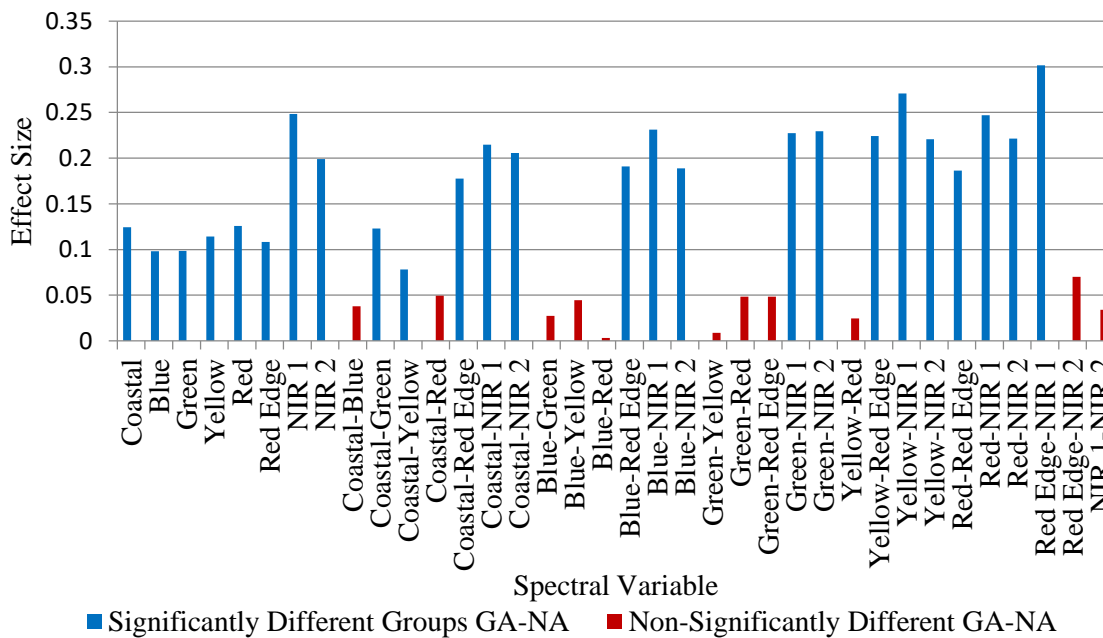


Figure 4.7. Pearson's r effect size of differences between GA and NA for WV-2 spectral variables. Blue bars represent variables in which classes were significantly different (Mann-Whitney  $U$ , d.f.=1;  $p < 0.05$ ) and red bar represent variables with no significant differences between groups (d.f.=1;  $p > 0.05$ ).

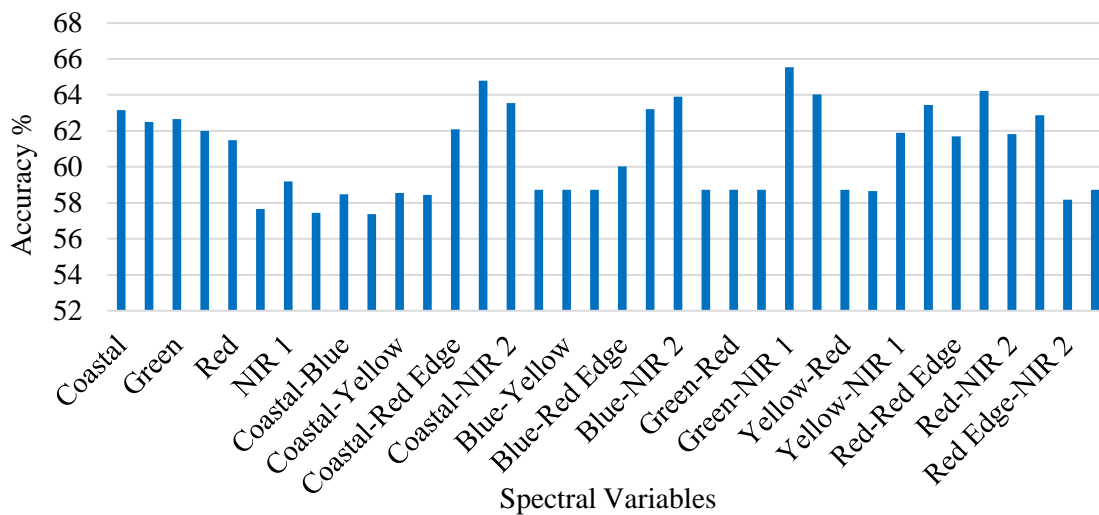


Figure 4.8. Per-variable logistic regression LOOCV accuracies.

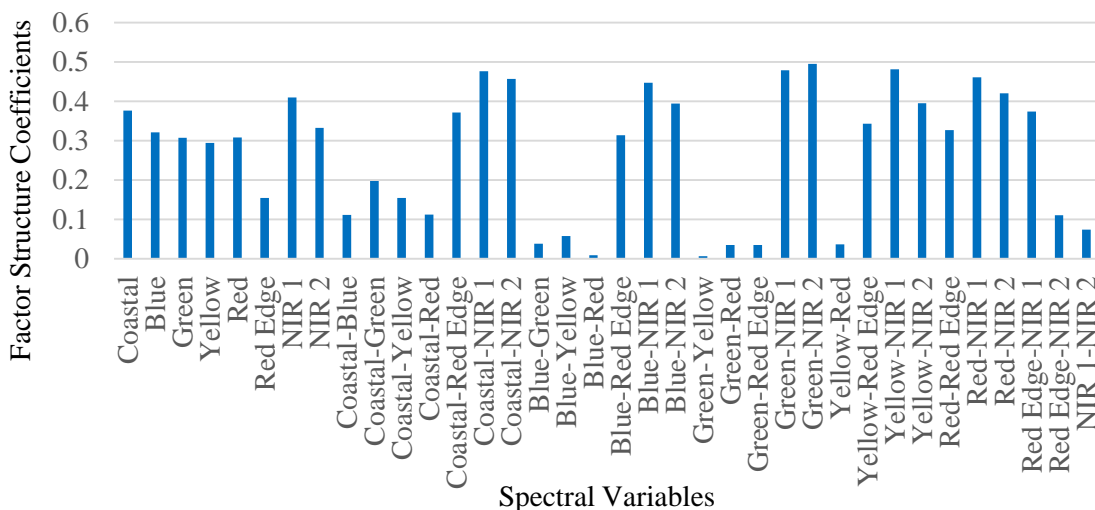


Figure 4.9. Linear discriminant analysis correlation structure coefficients for WV-2 spectral variables. Absolute values are displayed for visual purposes. Individual variables are correlated with a linear discriminant function with all spectral variables as predictors that significantly separate groups with a 69.1% overall accuracy (Wilks Lambda = 0.768;  $\chi^2=184.041$ ;  $df=29$ ;  $p<0.001$ ).

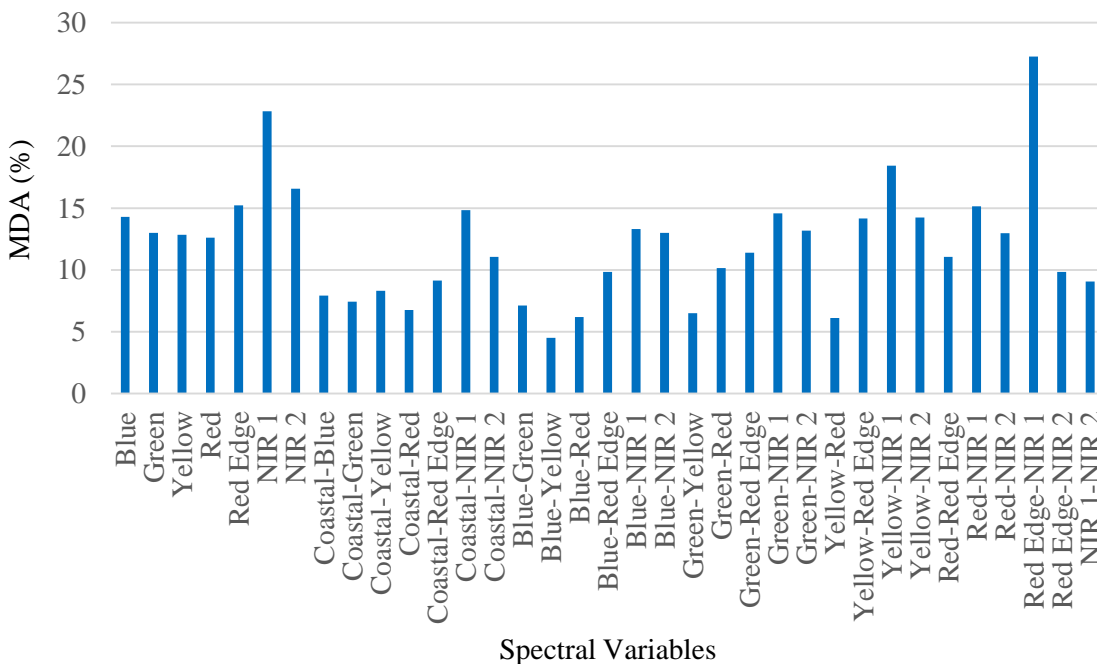


Figure 4.10. MDA of spectral variables attributed by Random Forest classification of OOB sample.

The WV-2 band with the highest influence on RF classification was the NIR-1 band, dropping prediction accuracies by 22.83% if removed from RF classification models (Figure 4.10). Other WV-2 bands had MDAs ranging from 12.61% to 16.57%. The spectral variable with this highest overall MDA was the normalized two-band index using the NIR-1 and red edge band (Figure 4.10). Indices using a combination of NIR bands and a visible band were relatively more important to RF classification compared to other combinations. Unlike the previous variable importance parameters inspected, the normalized two-band indices had comparable MDAs to the WV-2 bands, with exception to the red edge-NIR 1 index and NIR 1 band. It should be noted, unlike the other parameters which indicate variable importance relative to the other variables, the MDA of a single variable left out of a RF model will depend on its relationship with the variables left in the model.

### 4.3.3 Data Mining

The stepwise LR model significantly separated GA and NA trees with an LOOCV overall accuracy of 72.34% ( $\chi^2=125.30$ ;  $df=8$ ;  $p<0.001$ ) and selected eight variables before terminating the selection process (Table 4.4). The stepwise LDA model significantly separated GA and NA trees with a LOOCV overall accuracy of 67.45% (Wilks lambda = 0.828;  $\chi^2=131.733$ ;  $df=6$ ;  $p<0.001$ ) and selected six variables before terminating the selection process (Table 4.5). The selection of high separation-low correlation variables data mining process started with the red-edge-NIR 1 normalized two-band index, which had low correlations with other variables (Appendix C) and high

measures of separation. Spectral variables were then added to models with preference given to those with high and low correlations with other variables already in the models. Variables were added or subtracted in a trial and error manner based on improvements in

Table 4.4. Predictor variables selected by the final stepwise LR final model separating GA and NA trees.

<b>Predictor Variables</b>	<b>B</b>	<b>S.E.</b>	<b>Wald</b>	<b>df</b>	<b>Sig.</b>	<b>z-score</b>	<b>Exp(B)</b>
<b>NIR 1</b>	-0.521	0.072	52.211	1	0.000	-7.226	0.594
<b>Blue</b>	1.132	0.200	32.113	1	0.000	5.667	3.103
<b>Yellow</b>	0.070	0.048	2.115	1	0.146	1.454	1.073
<b>Red Edge</b>	0.102	0.053	3.736	1	0.053	1.933	1.107
<b>Green-Red</b>	-10.203	4.249	5.766	1	0.016	-2.401	0.000
<b>Blue-NIR 1</b>	-21.651	3.889	30.995	1	0.000	-5.567	0.000
<b>Red-NIR 2</b>	-10.755	5.329	4.073	1	0.044	-2.018	0.000
<b>Green-NIR 2</b>	16.842	5.578	9.117	1	0.003	3.019	20624308.424
<b>Constant</b>	-7.180	2.161	11.036	1	0.001	-3.322	0.001

cross-validated model accuracies until no further improvements could be practically ascertained by the author. Six spectral variables were selected by this method and make up model predictors Grouping 5 (Table 4.3).

Table 4.5. Predictor variables selected by stepwise LDA final model separating GA and NA trees. Standardized canonical discriminant function coefficients give the absolute relative importance of each variable within the final model.

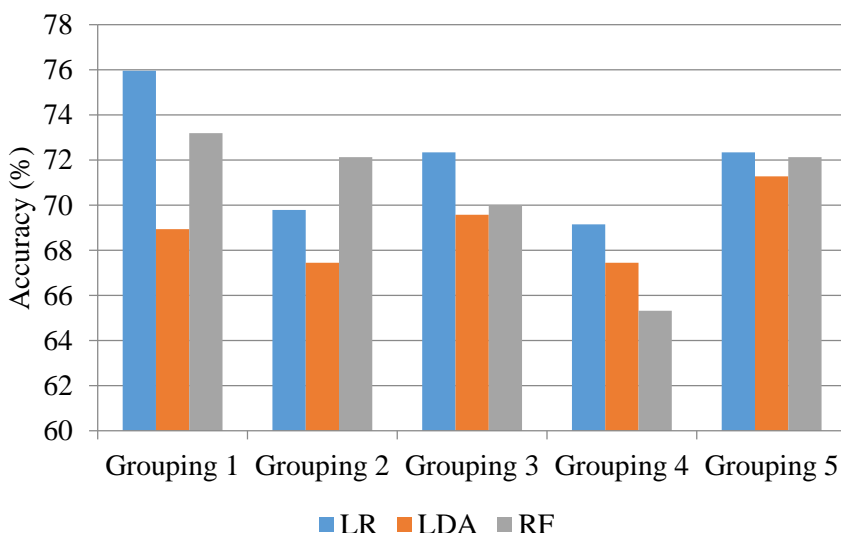
<b>Predictor Variables</b>	<b>Standardized Canonical Discriminant Function Coefficients</b>
<b>Yellow</b>	-1.896
<b>NIR 1</b>	1.788
<b>Green-Red</b>	1.796
<b>Green-NIR 2</b>	-1.795
<b>Yellow-NIR 1</b>	1.698
<b>Red-NIR 2</b>	1.450

### 4.3.4 Classification Accuracies

Appendices E and F include additional tables showing all of the overall, user’s, and producer’s accuracies, along with Kappa statistics, for each classifier and grouping of predictors for both the cross-validated and independently tested results.

#### 4.3.4.1 Cross-Validated Accuracies

Normalized two-band indices offered some improvements in the detection of GA damage. Using all 36 predictor variables (Grouping 1) as inputs for classification yielded higher overall accuracies (OA) than models using just the WV-2 bands (Grouping 2; Figure 4.11), including the model with the highest OA (LR classifier; 75.96%). LR classifiers yielded the highest OA in four of the five groupings, while the LDA models consistently had the lowest accuracies in all but one grouping. The data mining derived groupings used did not improve OAs compared to the models using all spectral variables



(Grouping 1), but were comparable to models using only the WV-2 bands as predictors. Manual selection of low correlation-high

Figure 4.11. Cross-validated classification OA for each classifier and predictor variable grouping. Predictor variable groupings are defined as (1) all 36 spectral variables, (2) eight WV-2 bands, (3) Stepwise LR selected, (4) Stepwise LDA selected, and (5) high importance-low correlation variables.

importance variables (Grouping 5) consistently outperformed input groupings based on stepwise selection methods (Groupings 3 & 4). The stepwise LDA selected grouping had the lowest OA for each classifier over all five groupings. The kappa coefficients of the classifiers indicate a range of probabilities from fair to moderate (Landis and Koch 1977) that the results achieved were above random chance ( $K = 0.300 - 0.494$ ; Appendix D).

#### 4.3.4.2 Independent Validation Accuracies

When performance was assessed using an independent dataset the classifiers performed worse compared to the cross-validated accuracies (Figure 4.11 & 4.12).

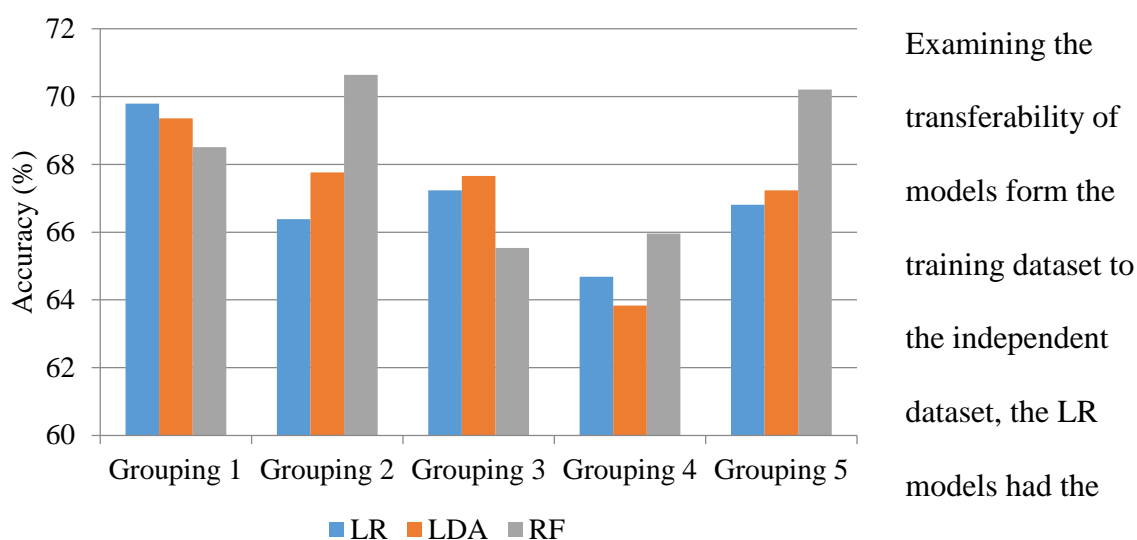


Figure 4.12. Independent dataset classification OA for each classifier and predictor variable grouping. Predictor variable groupings are defined as (1) all 36 spectral variables, (2) eight WV-2 bands, (3) Stepwise LR selected, (4) Stepwise LDA selected, and (5) high importance-low correlation variables.

Examining the transferability of models from the training dataset to the independent dataset, the LR models had the lowest generalization (i.e. more overfitting)

with a mean accuracy decrease of 4.94%, followed by the RF models (mean 2.38% decrease) and LDA classifiers (mean 1.77% decrease). The RF classifiers outperformed the other classifiers in three of the five variable groupings and produced the two best performing models with an OA of 70.64% for grouping 2 and 70.21% for grouping 5

(Figure 4.12). The LR and LDA methods had comparable performance for each grouping of predictor variables. Compared to the cross-validated accuracies, the improvements gained through using normalized two-band indices are more difficult to distinguish in the independent classification results. Consistently high accuracies across all three models for grouping 1 and the RF model for grouping 5 indicate improved GA detection but had lower accuracies than the RF classifier using only the WV-2 bands. Similar to the cross-validated training dataset, attempts to reduce model complexity by using subsets of predictor variables through data mining produced mixed results. Other than the RF classifier using the low correlation-high importance selected variables (Grouping 5), all three classifiers produced lower accuracies when using the data mined subsets of predictors (Groupings 3, 4, & 5) compared to the full model (Grouping 1). The stepwise LDA selected grouping (#4) underperformed compared to the two other data mining techniques, producing the lowest OA for two of the three classifiers. The kappa coefficients of all models indicate a fair probability (Landis and Koch 1977) that the results achieved are above random chance ( $K = 0.227 - 0.386$ ; Appendix E). Based on the cross-validated and independent validation results, the LR classifier using grouping 1 and RF classifier using grouping 2 were used to classify the entire WV-2 image masked with the green-tree segmentation shapefile to serve as an example of a potential operational map product.

While the OA of the best performing models indicate good potential for separating the two classes, the variance of accuracies between the two classes indicate that detection of GA trees might be more problematic. The GA class accuracies, user's

and producer's accuracies, indicate that GA trees suffer from errors of omission and commission a larger percent of the time than NA trees. GA user's and producer's accuracies ranged from 44.33-66.25% and 45.63-67.12%, respectfully (Figures 4.13 & 4.14), compared to the NA user's and producer's which ranged from 67.30-84.06% and 62.76-80.43%, respectfully (Figures 4.15 & 4.16). The two best performing classification methods (RF Grouping 2 & 5) had OA above 70% but GA user's and producer's accuracies below 60% and 66%, respectfully. Lower GA user's and producer's were also observed in the results based on cross-validation using the training data (Appendix D). The LR classifiers yielded higher GA user's accuracies across all variable groupings, with slightly lower but similar results observed for RF models using groupings 1, 2, & 5 (Figure 4.13). The LDA classifier achieved the highest GA producer's accuracies across four of the five groupings, with the RF models achieving similar results as well (Figure 4.14).

## **4.4 Discussion**

### **4.4.1 Spectral Response of GA and NA Trees**

Increased reflectance of GA trees within the visible bands is likely due to decreased absorption as photosynthetically active pigments, primarily total chlorophyll (chlorophyll *a* + chlorophyll *b*), which degrade following a successful MPB attack on a tree (Carter and Knapp 2001). Hyperspectral research examining MPB related GA damage and other plant stress agents have observed that spectral response is most sensitive in regions with lower chlorophyll absorption coefficients, such as the green

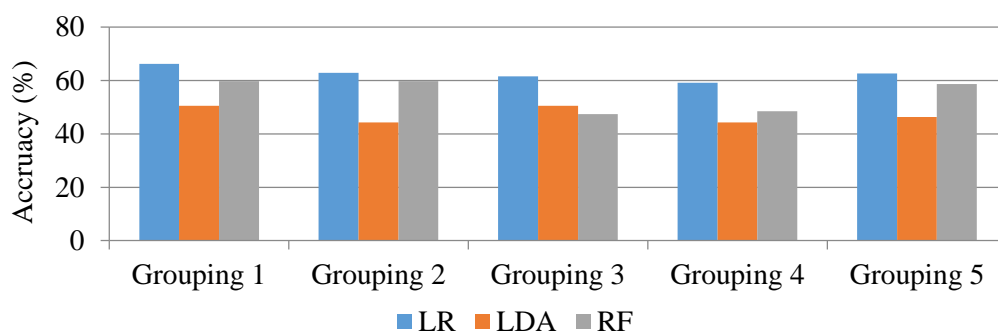


Figure 4.13. Independent dataset classification GA user's accuracies for each model and grouping of predictors.

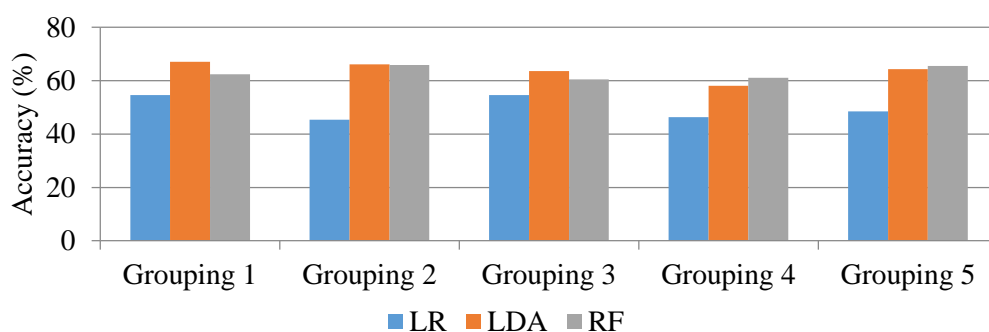


Figure 4.14. Independent dataset classification GA producer's accuracies for each model and grouping of predictors

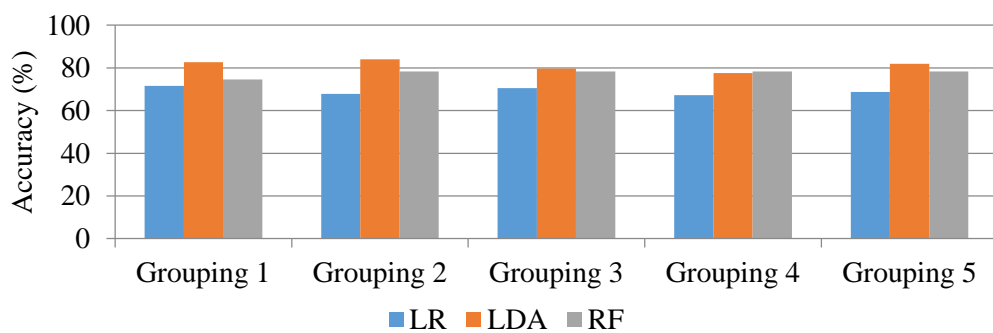


Figure 4.15. Independent dataset classification NA user's accuracies for each model and grouping of predictors.

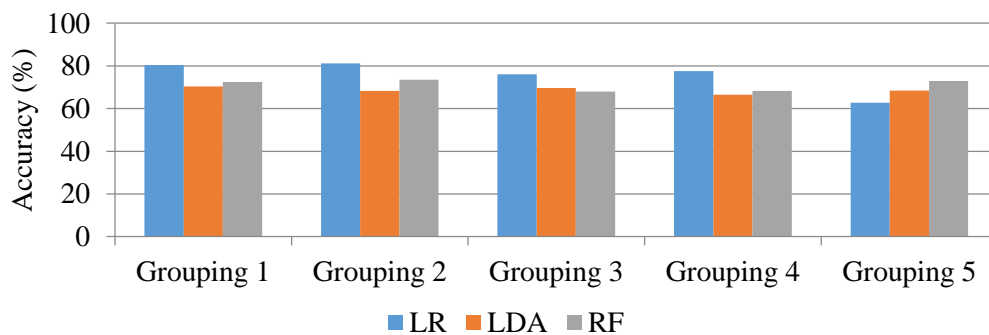


Figure 4.16. Independent dataset classification GA producer's accuracies for each model and grouping of predictors.

peak and red-edge regions of the spectrum (Ahern 1988; Carter 1993; Carter and Miller 1994; Carter and Knapp 2001; Fassnacht et al. 2014; Niemann et al. 2015). Spectral changes in the regions with higher chlorophyll absorption coefficients (blue and red spectrum) do not manifest until severe stress and chlorophyll loss has developed because absorption is strong enough saturate these regions even with some pigment degradation (Blackburn 1998; Carter and Knapp 2001; Blackburn 2007). The increased reflectance across all visible bands indicates a severe level of GA damage in this dataset, which is consistent with a late winter/ early spring collection date and a longer amount of time for stress to develop. Higher within-class variance in the visible bands of the GA samples is expected as the rates and timing of stress development within MPB attacked trees is highly variable from tree-to-tree and among localized environmental differences between stands (Wulder et al. 2009).

The red-edge region of the spectrum has been noted as important for discrimination of GA damage in previous studies (Ahern 1988; Carter and Knapp 2001; Niemann et al. 2015) and is consistently correlated with chlorophyll degradation and plant stress (Carter 1993; Carter and Miller 1994; Filella and Penuelas 1994; Blackburn 1998; Carter and Knapp 2001). In this study, GA reflectance in the red-edge band was significantly lower than NA trees (Figure 4.7), which is supported by Ahern (1988) who also observed lower GA reflectance for MPB lodgepole pines in the red-edge using ground-based hyperspectral data. However, red-edge response has been more commonly observed to increase in GA trees (Carter and Knapp 2001; Niemann et al. 2015) with red-edge reflectance being greater in stressed plants (Carter 1993; Filella and Penuelas 1994;

Blackburn 1998; Carter and Knapp 2001). Red-edge response observed in hyperspectral GA studies have noted shifts occur in a very narrow range of wavelengths (Carter and Knapp 2001; Niemann et al. 2015). The broader red-edge bands of the WV-2 sensor (705 – 745 nm) could also be influenced by a number of factors such as changes in internal structure towards the upper range of the red-edge band and changes in chlorophyll absorption in the lower range of the red-edge band. Research presented in Chapter 3, noted decreases in reflectance of GA needles around 740 nm but increases around 705-720 nm. This potentially explains why variance of the red-edge band was higher than visible bands, which are influenced primarily by pigment absorption.

In this study, reflectance in both NIR bands was significantly suppressed for GA trees (Figures 4.5 & 4.7). Lower NIR reflectance in GA trees is consistent with NIR response observed in previous hyperspectral GA research (Ahern 1988; Sharma 2007; Niemann et al. 2015) and other bark beetle research utilizing WV-2 imager (Immitzer and Atzberger 2015). As stress develops, there is a reduction in the number of refractory surfaces within the spongy mesophyll as leaves dehydrate and shrink, causing intercellular cavities and air-to-water interfaces to reduce (Ceccato et al. 2001). Since the NIR radiation penetrates deeper into leaves and primarily interacts with the spongy mesophyll, changes in these structures have stronger influence on bands in the NIR spectrum.

Reasons for spectral differences between classes cannot be isolated to changes in internal structures of GA needles alone. NIR reflectance is also influenced by other confounding factors. Aldakeheel and Danson (1997) noted confounding effects on

spectral response due to changes in moisture and internal structure are greatest in regions with low absorption, such as the NIR. In addition, age and positioning of needles on GA trees can influence the spectral response in the NIR (Ahern 1988); both of which were not accounted for in this study. Loss of foliage in pre-weakened GA trees could also increase NIR reflectance. The numerous factors influencing NIR reflectance may explain why NIR bands, along with the red-edge band, had the highest within-class variance. Inclusion of background elements and spectral mixing may also increase class variance, which is a greater problem in coniferous trees due to their conical shape creating less sunlit areas compared to broad-leaf trees. The object based method of extracting the values from entire tree crown and using average reflectance values should minimize these effects.

#### **4.4.2 Variable Importance and Discriminating Ability**

All of the WV-2 bands had some relevancy in discriminating GA and NA classes, but it is difficult to discern which are relatively best for separating classes. Non-parametric analysis (Mann-Whitney U and effect size) and the RF method, which is robust against multicollinearity and distribution problems, indicated the two NIR bands best discriminate between classes (Figure 4.7 & 4.10). The LR and LDA results indicated that WV-2 bands in the visible range either improved discrimination (LR LOOCV; Figure 4.8) or were similar (LDA; Figure 4.9) compared to the red-edge, NIR-1 & 2 bands. Large variance and spectral similarities between classes in the red-edge, NIR-1,

and NIR-2 bands could account for decreased discrimination in models analyzing the importance of individual WV-2 bands.

Normalized two-band indices utilizing a combination of a NIR band and visible band better separated classes compared to any individual WV-2 bands. This was expected as these regions have lower correlations (Appendix C) and combine unique information from visible regions, where GA reflectance is higher, and the NIR regions, where GA reflectance is suppressed (Figures 4.4, 4.5, & 4.6). Although not specifically compared in this study, normalized two-band indices may also provide comparable results to models using all eight WV-2 bands as well. The LR accuracies of the index using the green and NIR-1 bands achieved a similar overall accuracy (65.54%; Figure 4.8) to the LR model using all WV-2 bands (69.79%; Figure 4.12). Use of a single variable could cut down on the amount of analyst input and processing time for predictive models and produce more generalizable models that are less prone to overfitting. However, it should be noted these results may not be directly comparable because the per-spectral variable LR models were created using the entire extracted dataset while the LR models used to classify damage using all eight WV-2 bands (Grouping 1) were trained with a split (2/3<sup>rd</sup>) of the extracted dataset and validated with the remaining split.

#### **4.4.3 Classification Accuracies and Model Performance**

Despite substantial overlap in spectral response variability between the two damage classes, WV-2 imagery and the classifiers analyzed in this study show some promise towards the discrimination of GA damage. Cross-validated and independent

dataset classification results indicate that RF and LR classifiers outperform LDA classification (Figures 4.11 & 4.12). This was expected as LR and RF methods are more robust against non-normality and multicollinearity compared to the parametric LDA classifier. While LR models consistently yielded the highest accuracies when cross-validated with the training data, the RF methods produced the highest accuracies when transferred to the independent dataset (Figures 4.11 & 4.12). Increased generalization of RF methods compared to others examined in this study support claims that RF classification models not only handle multicollinearity and non-parametric data well but are also less prone to overfitting models, especially with larger numbers of predictor variables (Brieman 2001; Liaw and Wiener 2002).

Since GA damage is the target class for mitigation, lower GA user's and producer's accuracies (Figures 4.13 & 4.14) diminish the potential of the presented methods to be reliably used for GA detection at a level needed for operational use. The ratios of GA to NA trees in natural settings, in which GA trees occur in smaller numbers and patches, could further complicate operational use of these methods. In this study, GA and NA trees were sampled at relatively similar numbers, increasing the likelihood that of GA trees being correctly classified by probability alone. When applied in a natural setting, underestimations of GA damage may be more severe due to lower GA to NA ratios. LR models generally yielded higher user's accuracies for the GA class and LDA models generally had higher producer's accuracies, with RF yielding slightly lower for both. If shown to be further consistent, this unanticipated result could potentially be beneficial as it would allow forest officials to select different types of classifiers based on

the goals of mitigation. If mitigation is focused on more accurately placing ground troops in locations where GA is likely and reductions in wasted man-hours is emphasized, a classifier that yields higher GA user's accuracies, such as the LR classifiers, is more appropriate. If mitigation is focused more on a GA inventory or infestation spread, then classifiers that have higher producer's accuracies, such as the LDA, are more appropriate. When time and resources are limited, RF methods could provide results applicable to both.

Low user's and producer's accuracies for the GA class are likely due to large within-class variance and spectral confusion with healthy trees (Figure 4.6). Even with the unique spectral characteristics, the spectral resolution of the WV-2 bands is likely too broad to capture the subtle spectral differences of GA trees observed in previous hyperspectral research (See Chapter 3). For example, previous GA studies (Ahern 1988; Carter and Knapp 2001; Niemann et al. 2015) have commonly identified narrow shifts in the red-edge of GA trees as important regions for discrimination. These narrow shifts are less likely to be detectable with broader band sensors. In this study, the red-edge band was significantly different between GA and NA classes and consistently had lower indications of discriminatory power compared to the other spectral variables.

Looking at the example maps produced (Figures 4.17 & 4.18) it is evident how low GA class accuracies can negatively impact the usefulness of the classification maps produced. Compared to the reference Google Earth image (Figure 4.19) from September following the image acquisition, the user can see a number of commission errors (user's errors) within the yellow polygons and omission errors (producer's) outside of it. Trends

in user's and producer's errors between classifier types are also illustrated by the classified images. The RF classified image (Figure 4.17) overestimates the amount of GA pixels on the entire image compared to the LR classified image (Figure 4.17), which mirrors the differences in user's and producer's accuracies between the two classifiers observed in the independent dataset results (Figures 4.13 & 4.14).

Inclusion of normalized two-band indices as input predictor variables generally improved classification results. Models using all 28 indices plus the WV-2 bands as predictors (Grouping 1) yielded the highest cross-validated results and had consistently high accuracies when classifying the independent dataset. However, the RF model using just the WV-2 bands (Grouping 2) as predictors yielded the highest OA classifying the independent dataset, possibly foregoing the need to generate normalized two-band indices. Reliable GA detection without further data transformations would cut down on the amount of processing time and power needed to include variables such as the indices examined herein. This could potentially shorten the amount of time between image acquisition and mitigation. Benefits of using normalized indices are that it reduces the effects of illumination and topographic effects within a scene. This may better allow models to be transferred across multiple scenes and time periods.

Reducing model complexity through the data mining methods examined in this study did not improve results over models using all eight WV-2 bands or all 36 spectral variables. The stepwise LDA methods consistently produced the lowest OA compared to the other data mining methods, further confirming the unsuitability of parametric methods. Overall, the variables selected by interpretation of the correlation matrix and

indicators of variable importance produced better results than the two stepwise selection methods, including the model with the 2<sup>nd</sup> highest OA when classifying the independent dataset (RF – Grouping 5). While this method relies on the subjectivity of the analyst and more time consuming, it may be more appropriate and overcome the statistical shortcomings of stepwise selection methods that have been previously documented (Thompson 1995). Even though the RF model using Grouping 5 was a high performing model, there is a high likelihood that results could be improved if more time and focus is devoted to finding better combinations of predictor variables. It is unlikely that the six variables chosen in this study are the best possible combination as there are over 1.9 million potential combinations that could be derived from the 36 spectral variables analyzed.

#### **4.4.4 Limitations**

The methods used to validate the classification accuracy are reliable unless there are inherent biases within reference data. This is a potential limitation in this research since ground data was collected using convenience sampling methods and was not truly randomized due to the practical limitations of accessibility to all areas within the study area. Even though attention was given to not include fading trees in the GA samples, given the month long period between the field visit and image acquisition, there is a possibility that GA trees observed as green during the field visit had experienced some fading. Registration errors in GPS measurements could also bias the reference data, however careful analysis of the previous year Google Earth imagery was used to

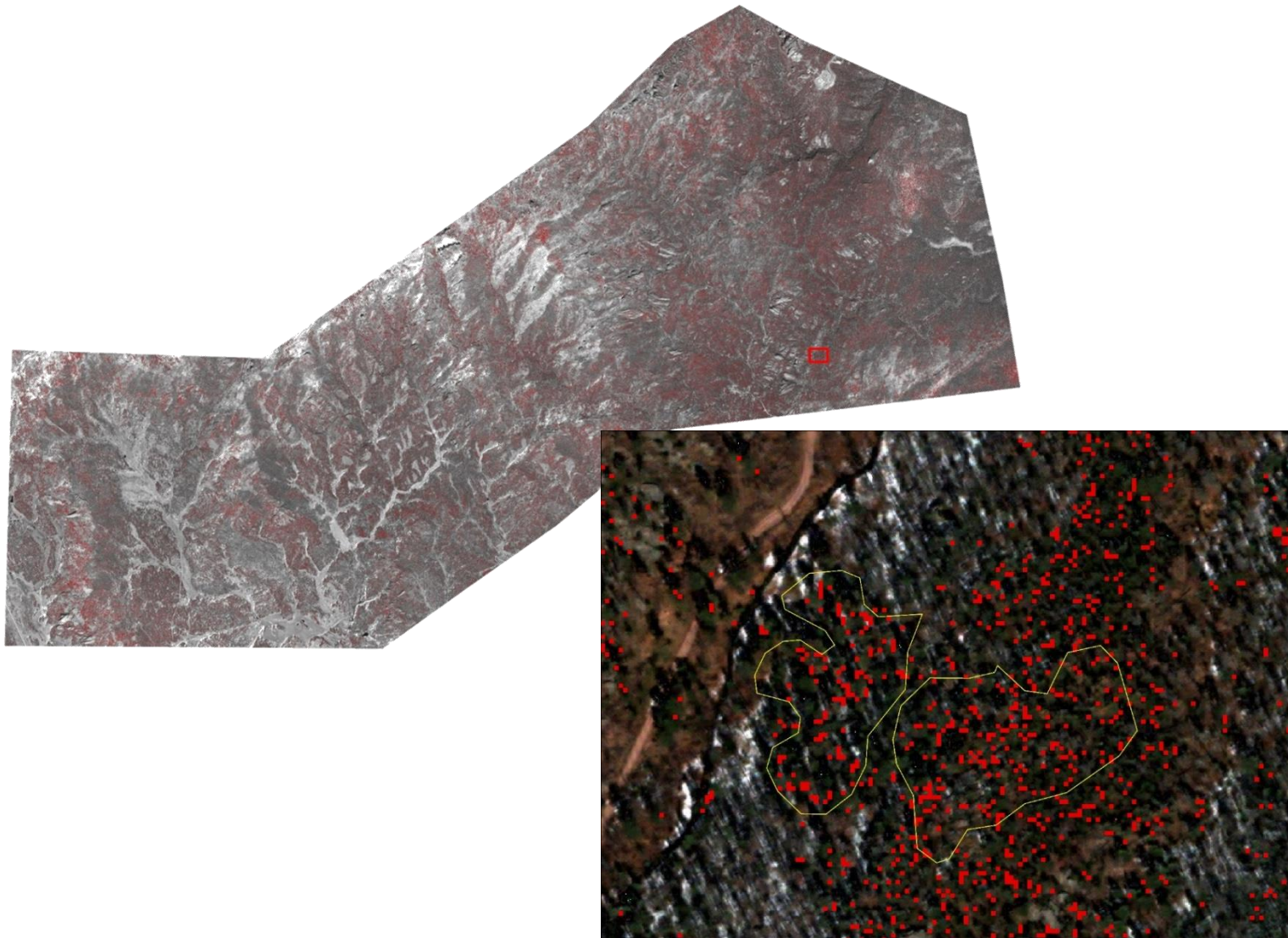


Figure 4.17. GA tree crowns (red) classified with the RF classifier using only WV-2 bands as predictors. Classified layer overlaid on the panchromatic WV-2 image (top) and pansharpened WV-2 image (subset). Clusters of GA damage outlined in yellow for comparison to a reference image (Figure 4.19)

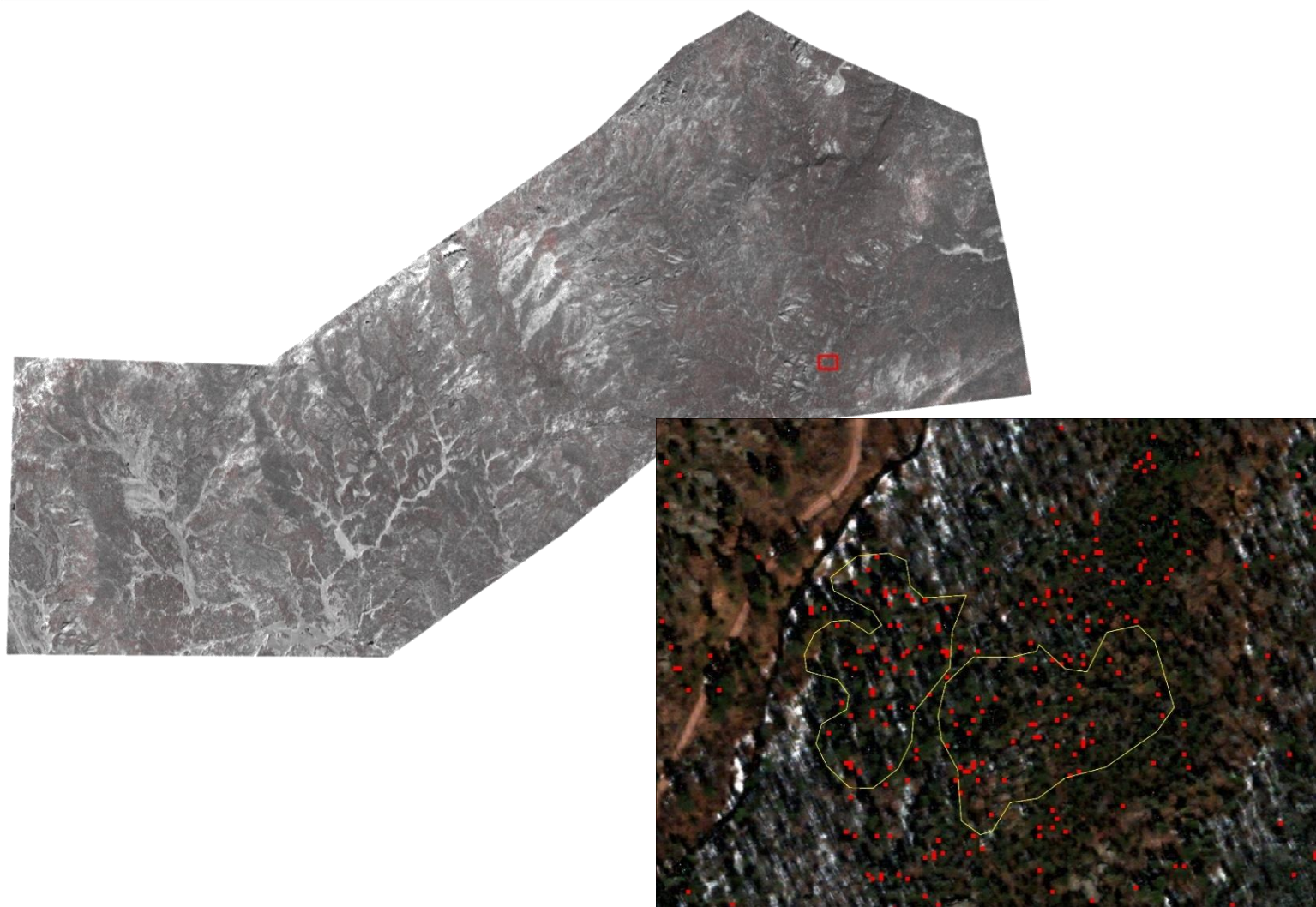


Figure 4.18. GA tree crowns (red) classified with the LR classifier using all 36 WV-2 spectral variables as predictors. Classified layer overlaid on the panchromatic WV-2 image (top) and pansharpened WV-2 image (subset). Clusters of GA damage outlined in yellow for comparison to a reference image (Figure 4.19)

minimize any of these negative impacts. Another limitation to this study, and potentially to later winter/early spring collection dates in general, are the less than ideal acquisition dates. Later winter/early spring collection of imagery in the Northern latitudes suffers from cloudy conditions, lower sun angles, and possible snow. The image used in this study had some snow cover in the image. Snow interfered with the atmospheric correction algorithms, causing undesired contaminated pixels in the image that needed to be removed. Image segmentation prior to extraction and classification removed a large amount of the snow from the image and is a necessary processing step under these conditions.



Figure 4.19. Google Earth™ imagery acquired 09/12/2015 with similar coverage to Figure 4.17 & 4.18 subsets. GA trees in the Figure 4.17 & 4.18 subsets will appear as red crowns in this image. Sunlit red tree crowns not classified as GA damage in the subset images likely represent examples of GA classification errors of commission.

#### 4.5 Summation

In this study, the spectral response of healthy and GA ponderosa pine trees located in the Black Hills was examined using WV-2 imagery and ground-truth data to determine which spectral variables best discriminate damage. GA and NA spectral responses were significantly different in each WV-2 band. Normalized two-band indices using a NIR and visible band increased discrimination compared to single WV-2 bands alone.

Classification using high separation-low correlated variables with a RF classifier yielded promising results, but otherwise data mining produced models with lower accuracies. Including normalized two-band indices as predictor variables produced models with relatively high and consistent accuracies. Classification using a RF classifier achieved the two highest independently validated accuracies (70.6% & 70.2%). While the overall accuracies achieved are comparable to previous research, the GA class user's and producer's accuracies were lower than the NA class. The likely reason for misclassifications of the GA class is due to high with-in class variances and spectral overlap with the NA class. Given the lower GA class accuracies, these methods are unlikely to be successful as a stand-alone detection method. However, consistencies in GA class user's and producer's accuracies could provide forest officials a means to customize methods to meet the needs of mitigation objectives. Given the benefits of the WV-2 datasets compared to aerial hyperspectral data, these methods offer a means to deploying ground crews to more likely GA areas where the crews can further assess the presence or lack thereof of GA trees.

## 5. Conclusions

Reliable early detection of MPB damage in coniferous forest would provide numerous advantages over traditional ground-based detection methods and improve the efficacy of mitigation. This research presented in this study aims to better understand the potential of remote sensing for MPB GA detection using ground-based spectroradiometer and satellite multispectral (WV-2) data.

Using hyperspectral data collected from needle stacks of GA and NA pine trees, this study identified several regions in the VNIR and SWIR spectrum that consistently separated the two classes and show promise for canopy level detection. Bands associated with the edges of water absorption features in the SWIR, from 1451-1540 nm and 1973-2103 nm, consistently yielded the greatest measures of discrimination across multiple statistical methods. Bands associated with regions influenced by total chlorophyll absorption from 462-520 nm and 663-689 nm consistently had the best discrimination in the visible spectrum. The spectral response of GA damage trees observed in this study is consistent with moisture loss and chlorophyll degradation from plant stress. Results also indicated evidence of more developed plant stress compared to GA studies with earlier collection windows. Using a later winter/early spring collection window allows more time for stress to onset, thus greater spectral differentiation between GA and NA trees.

It is unknown if these results can be scaled up for classification at the canopy level. High within class variance and overlap between classes is potentially a source of confusion. The SWIR bands recommended for GA detection are located near regions influenced by atmospheric water vapor scattering, which could decrease signal-to-noise

ratios. A degree of uncertainty can also be expected when scaling up results as variability in canopy structures cannot be accounted for at the needle level.

The ground-based hyperspectral findings of this study can be used to guide the use of existing remote sensing data sources for GA detection along with the development of future satellite-based remote sensing methods. Given the numerous options in sensors available, examining the suitability by a case-by-case basis would not be feasible. The information presented here can be used to select appropriate data sources and reduce data complexity or redundancy, thus saving valuable time and resources and potentially improving classification accuracies. Further analysis examining continuum and scale-based methods of normalizing the spectra and spectral derivative analysis can be used to remove unwanted noise and extract shape metrics from the spectra. These could be used to improve results and identify more subtle change features not identified in this study. Separation between classes may be improved through the use of vegetation and moisture indices. Future research can use the results here to guide the selection of these indices and help modify them by utilizing the damage sensitive and insensitive bands reported. Additionally, measurements of needle moisture and chlorophyll *a* and *b* content could be correlated with spectral differences observed in this study to better understand the biophysical changes in MPB attacked trees. This information could help explain the drivers of differences between GA and NA trees in the late winter/early spring following the initial MPB attacks.

To further meet the study objectives, ground-truth data and WV-2 imagery were used to identify multispectral variables that best discriminate GA and NA classes using

multiple statistical measures and classification was implemented using LR, LDA, and RF classifiers to examine the potential for canopy-level GA detection. All eight WV-2 bands significantly discriminated the two classes. Normalized two-band indices using a NIR band and visible band increased the separation of GA and NA trees, however it was inconclusive where using normalized two-band indices as a predictor variables in classification improved detection compared to only the eight WV-2 bands.

RF classifiers yielded models with the two best independently validated accuracies, with OA of 70.6% for the model using the eight WV-2 bands as predictors and 70.2% for the model using a grouping of spectral variables selected based on measures of importance and low correlations with each other. Furthermore, the RF classifiers showed the lowest degree of overfitting, required the least amount of user input, and had faster processing times.

The best performing models yielded accuracies that are comparable to those achieved in previous studies attempting MPB GA detection using hyperspectral aerial imagery (Heath 2001; Fassnacht et al. 2014) and spruce beetle GA detection using WV-2 data (Immitzer and Atzberger 2014). This is likely due to high spatial resolution of the WV-2 imagery. Furthermore, the WV-2 satellite offers a number of advantages over hyperspectral aerial imagery for GA detection. Hyperspectral data has a large number of variables that increase storage amount, decrease processing time, and reduce data dimensionality for most classification algorithms. The WV-2 image has multi-look capabilities which increases the temporal resolution and offers a larger coverage of the

landscape, where aerial imagery may require many flights and images to cover similar areas.

While the overall accuracies achieved are relatively good compared to previous research, the low GA user's and producer's accuracy observed mean the methods presented here are unlikely to reach the detection rates needed to successfully mitigate beetle infestations as a stand-alone detection method. All three classifiers underestimated GA damage relative to NA damage. However, given the benefits of the WV-2 datasets, these methods offer improvements over the existing GA detection methods. When used in conjunction with more traditional strategies, these methods can augment GA detection and may provide the coverage needed to improve the effectiveness of mitigation efforts. Consistencies in GA class user's and producer's accuracies could provide forest officials a means to customize methods to meet the needs of mitigation objectives. Detection maps can be incorporated in to other GIS analysis, such as heat mapping or hot spot analysis, to improve the placement of ground mitigation. Furthermore, future studies could investigate feasibility of using higher NA class accuracies to estimate GA damage by calculating the difference between forested area and NA trees.

Given the possible number of combinations, it is unlikely that the subset of predictor variables selected by the author's interpretation of variable importance results and correlation matrices produce the optimal grouping of predictors. Further data mining efforts will likely produce a more optimal grouping that yield higher accuracies while reducing model complexity. The indices examined in this research were relatively simple ratios based on the normalized difference vegetation index equation. Future research into

other vegetation indices using transformations of multiple bands could further improve detection accuracies. Given the separation between GA and NA observed for SWIR bands in the ground-based hyperspectral data, future detection and mapping using high spatial resolution satellite systems with SWIR bands, such as the WorldView-3 satellite, is recommended and will likely improve detection accuracies.

### **5.1 Final Thoughts**

Analysis of hyperspectral needle-level measurements identified multiple visible and SWIR regions of bands that discriminated GA damage from NA trees. This suggests that canopy level detection maybe possible and results can be used to guide the development of such methods. Attempts to accurately classify GA damage with WV-2 imagery achieved overall accuracies similar to previous studies using hyperspectral data, but given the low GA class accuracies, operational use of these methods as a stand-alone detection method will require technological advances in sensing systems. However, given the advantages of satellite data over aerial data, it is the author's opinion that the methods presented offer improvement over existing methods. Incorporating these methods with further research into different spectral variables and/or future improvements in the spectral and spatial resolutions of sensors may yield high enough accuracies to adequately supplement existing ground-based GA detection methods and improve effectiveness of GA detection.

## References

- Adam, E.M., Mutanga, O. Rugege, D., & Ismail. R., 2012. Discriminating the papyrus vegetation (*Cyperus papyrus* L.) and its co-existent species using random forest and hyperspectral data resampled to HYMAP. *International Journal of Remote Sensing*, 33(2), pp.552–569.
- Ahern, F.J., 1988. The effects of bark beetle stress on the foliar spectral reflectance of lodgepole pine. *International Journal of Remote Sensing*, 9(9), pp.1451–1468.
- Aldakheel, Y. & Danson, F., 1997. Spectral reflectance of dehydrating leaves: measurements and modelling. *International Journal of Remote Sensing*, 18(17), pp.3683–3690.
- Amman, G., 1973. Population changes of the mountain pine beetle in relation to elevation. *Environmental Entomology*, 2(4), pp.541–547.
- Amman, G. & Cole, W., 1980. *Mountain pine beetle dynamics in lodgepole pine forests, Part 1: course of an infestation*, USDA Forest Service, Intermountain and Range Experiment Station, General Technical Report INT-89, p. 56.
- Amman, G., 1984. Mountain pine beetle (Coleoptera: Scolytidae) mortality in three types of infestations. *Environmental Entomology*, 13(1), pp.184–189.
- Analytical Spectral Devices, 1999. *Analytical Spectral Devices, Inc. (ASD) Technical Guide 3rd Ed.*, Boulder, CO.
- Atkinson, A.C., 1994. Fast very robust methods for the detection of multiple outliers. *Journal of the American Statistical Association*, 89(428), pp.1329–1339.

- Ballard, R., Walsh, M. & Cole, W., 1984. The penetration and growth of blue-stain fungi in the sapwood of lodgepole pine attacked by mountain pine beetle. *Canadian Journal of Botany*, 62, pp.1724–1729.
- Bearup, L., Maxwell, R., Clow, D. & Mccray, J.E., 2014. Hydrological effects of forest transpiration loss in bark beetle-impacted watersheds. *Nature Climate Change*, April.
- Bentz, B.J., Logan, J.A. & Amman, G.D., 1991. Temperature-dependent development of the mountain pine beetle (Coleoptera: Scolytidae) and simulation of its phenology. *The Canadian Entomologist*, 123(5), pp.1083–1094.
- Bentz, B.J., Régnière, J., Fettig, C.J., Hansen, E.M., Hayes, J.L., Hicke, J.A., Kelsey, R.G., Negrón, J.F. & Seybold, S.J., 2010. Climate change and bark beetles of the western United States and Canada: direct and indirect effects. *Bioscience*, 60(8), pp.602–613.
- Blackburn, G.A., 1998. Spectral indices for estimating photosynthetic pigment concentrations: A test using senescent tree leaves. *International Journal of Remote Sensing*, 19(4), pp.657–675.
- Blackburn, G., 2007. Hyperspectral remote sensing of plant pigments. *Journal of Experimental Botany*, 58(4), pp 855-867.
- Breiman, L., 2001. Random Forests. *Machine Learning*, 45(1), pp.5–32.
- Brown, M.G., Black, T.A., Nesic, Z., Foord, V.N., Spittlehouse, D.L., Fredeen, A.L.,

- Bowler, R., Grant, N.J., Burton, P.J., Trofymow, J. A., Lessard, D., & Meyer, G., 2014. Evapotranspiration and canopy characteristics of two lodgepole pine stands following mountain pine beetle attack. *Hydrological Processes*, 28(8), pp.3326–3340.
- Canty, A. & Ripley, B., 2016. boot: Bootstrap R (S-Plus) Functions. R package version 1.3-18.
- Cao, Z., Wang, Q. & Zheng, C., 2015. Best hyperspectral indices for tracing leaf water status as determined from leaf dehydration experiments. *Ecological Indicators*, 54, pp.96–107.
- Carter, G.A., 1993. Responses of leaf spectral reflectance to plant stress. *American Journal of Botany*, 80(3), pp.239–243.
- Carter, G.A. & Miller, R.L., 1994. Early detection of plant stress by digital imaging within narrow stress-sensitive wavebands. *Remote Sensing of Environment*, 50(3), pp.295–302.
- Carter, G.A. & Knapp, A.K., 2001. Leaf optical properties in higher plants: linking spectral characteristics to stress and chlorophyll concentration. *American Journal of Botany*, 88(4), pp.677–84.
- Ceccato, P., Flasse, S., Tarantola, S., Jacquemoud, S., & Grégoire, J.M., 2001. Detecting vegetation leaf water content using reflectance in the optical domain. *Remote Sensing of Environment*, 77(1), pp.22–33.
- Chan, J.C.-W. & Paelinckx, D., 2008. Evaluation of Random Forest and Adaboost tree-

based ensemble classification and spectral band selection for ecotope mapping using airborne hyperspectral imagery. *Remote Sensing of Environment*, 112(6), pp.2999–3011.

Chapman, T.B., Veblen, T.T. & Schoennagel, T., 2012. Spatiotemporal patterns of mountain pine beetle activity in the southern Rocky Mountains. *Ecology*, 93(10), pp.2175–2185.

Cheng, T., Rivard, B., Sánchez-Azofeifa, G.A., Feng, J., & Calvo-Polanco, M., 2010. Continuous wavelet analysis for the detection of green attack damage due to mountain pine beetle infestation. *Remote Sensing of Environment*, 114(4), pp.899–910.

Cho, M.A., Malahlela, O. & Ramoelo, A., 2015. Assessing the utility WorldView-2 imagery for tree species mapping in South African subtropical humid forest and the conservation implications: Dukuduku forest patch as case study. *International Journal of Applied Earth Observation and Geoinformation*, 38, pp.349–357.

Clevers, J.G.P.W., Kooistra, L. & Schaepman, M.E., 2008. Using spectral information from the NIR water absorption features for the retrieval of canopy water content. *International Journal of Applied Earth Observation and Geoinformation*, 10(3), pp. 388-397.

Clevers, J.G.P.W., Kooistra, L. & Schaepman, M.E., 2010. Estimating canopy water content using hyperspectral remote sensing data. *International Journal of Applied Earth Observation and Geoinformation*, 12(2), pp.119–125.

- Coggins, S.B. et al., 2011. Comparing the impacts of mitigation and non-mitigation on mountain pine beetle populations. *Journal of Environmental Management*, 92(1), pp.112–120.
- Cohen, J., 1988. *Statistical Power Analysis for the Behavioral Sciences* 2nd ed., New York: Academic Press.
- Cole, W., 1981. Some risks and causes of mortality in mountain pine beetle populations: a long-term analysis. *Researches on Population Ecology*, 23(1), pp.116–144.
- Continuing Education in Ecosystem Management Group, 2006. Norbeck Wildlife Preserve Landscape Assessment, Black Hills National Forest, USDA National Forest Service, p.122.
- Coops, N.C., Timko, J.A., Wulder, M.A., White, J.C. & Ortlepp S.M., 2008. Investigating the effectiveness of Mountain Pine Beetle mitigation strategies. *International Journal of Pest Management*, 54(2), pp.151–165.
- Coops, N.C., Wulder, M.A., & White, J.C., 2006. Assessment of Quickbird high spatial resolution imagery to detect red-attack damage due to mountain pine beetle infestation. *Remote Sensing of Environment*, 103(1), pp.67–80.
- Curran, P.J., 1989. Remote sensing of foliar chemistry. *Remote Sensing of Environment*, 30(3), pp.271–278.
- Dennison, P., Brunelle, A. & Carter, V., 2010. Assessing canopy mortality during a mountain pine beetle outbreak using GeoEye-1 high spatial resolution satellite data. *Remote Sensing of Environment*, 114(11), pp.2431–2435.

- Edburg, S.L., Hicke, J.A., Lawrence, D.M., & Thornton, P.E., 2011. Simulating coupled carbon and nitrogen dynamics following mountain pine beetle outbreaks in the western United States. *Journal of Geophysical Research*, 116(June), pp.1–15.
- Elvidge, C.D., 1990. Visible and near infrared reflectance characteristics of dry plant materials. *International Journal of Remote Sensing*, 11(10), pp.1775–1795.
- Fassnacht, F.E., Latifi, H., Ghosh, A., Joshi, P.K., & Kock, B., 2014. Assessing the potential of hyperspectral imagery to map bark beetle-induced tree mortality. *Remote Sensing of Environment*, 140, pp.533–548.
- Field, A., 2009. *Discovering Statistics Using SPSS* 3rd ed., Sage Publications Ltd.
- Filchev, L., 2012. An assessment of European spruce bark beetle infestation using Worldview-2 satellite data. In *Proceedings of 1<sup>st</sup> European SCGIS Conference with International Participation-Best Practices: Application of GIS Technologies for Conservation of Natural and Cultural Heritage Sites*. Sofia, Bulgaria, pp. 21-23
- Filella, I. & Penuelas, J., 1994. The red edge position and shape as indicators of plant chlorophyll content, biomass and hydric status. *International Journal of Remote Sensing*, 15(7), pp. 1459-1470.
- Foley, S., Rivard, B., Sanchez-Azofeifa, G.A. & Calvo J., 2006. Foliar spectral properties following leaf clipping and implications for handling techniques. *Remote Sensing of Environment*, 103(3), pp.265–275.
- Fourty, T. & Baret, F., 1997. Vegetation water and dry matter contents estimated from top-of-the-atmosphere reflectance data: A simulation study. *Remote Sensing of*

*Environment*, 61(1), pp.34–45.

Franklin, S.E., Wulder, M.A., Kakun, R.S. & Carroll, A.L., 2003. Mountain pine beetle red-attack forest damage classification using stratified Landsat TM data in British Columbia, Canada. *Photogrammetric Engineering & Remote Sensing*, 69(3), pp.283–288.

Freeman, J., 2014. *Black Hills Forestry: A History*, University Press of Colorado.

Gao, B.-C. & Goetz, A.F.H., 1990. Column atmospheric water vapor and vegetation liquid water retrievals from Airborne Imaging Spectrometer data. *Journal of Geophysical Research*, 95(D4), p.3549.

Gibson, K., Kegley, S. & Bentz, B., 2009. Forest insect & disease leaflet 2: Mountain pine beetle. USDA Forest Service, Forest Insect and Disease Leaflet 2, p. 12.

Gislason, P.O., Benediktsson, J.A. & Sveinsson, J.R., 2006. Random Forests for land cover classification. *Pattern Recognition Letters*, 27. pp. 294-300.

Gitelson, A.A., Merzlyak, M.N. & Chivkunova, O.B., 2001. Optical Properties and Nondestructive Estimation of Anthocyanin Content in Plant Leaves. *Photochemistry and Photobiology*, 74(1), pp.38–45.

Gong, P., 1997. Conifer species recognition: An exploratory analysis of in situ hyperspectral data. *Remote Sensing of Environment*, 62(2), pp.189–200.

Goodwin, N.R., Coops, N.C., Wulder, M.A., Gillanders, S., Schroeder, T.A., & Nelson, T., 2008. Estimation of insect infestation dynamics using a temporal sequence of Landsat data. *Remote Sensing of Environment*, 112(9), pp.3680–3689.

- Graham, R.T., Asherin, L.A., Battaglia, M.A., Jain, T.B., & Mata, S.A., 2016. *Mountain Pine Beetles : A Century of Knowledge, Control Attempts , and Impacts Central to the Black Hills*, USDA Forest Service, Rocky Mountain Research Station, General Technical Report RMRS-GTR-353, Fort Collins, CO, p. 193.
- Graves, H.S., 1899. *The Black Hills Forest Reserve*, U.S. Government Printing Office.
- Griffin, J.M., Turner, M.G. & Simard, M., 2011. Nitrogen cycling following mountain pine beetle disturbance in lodgepole pine forests of Greater Yellowstone. *Forest Ecology and Management*, 261(6), pp.1077–1089.
- Ham, J., Chen, Y., Crawford, M.M. & Ghosh, J., 2005. Investigation of the random forest framework for classification of hyperspectral data. *IEEE Transactions on Geoscience and Remote Sensing*, 43(3), pp.492–501.
- Hansen, E. & Bentz, B., 2003. Comparison of reproductive capacity among univoltine, semivoltine, and re-emerged parent spruce beetles (Coleoptera: Scolytidae). *The Canadian Entomologist*, 135, pp.697–712.
- Hansen, E.M., Amacher, M.C., Miegroet, H.V., Long, J.N. & Ryan, M.G., 2015a. Carbon dynamics in central US Rockies lodgepole pine type after mountain pine beetle outbreaks. *Forest Science*, 61(4), pp.665–679.
- Hansen, E.M. Johnson, M.C., Bentz, B.B., Vandygriff, J.C. & Munson, A.S., 2015b. Fuel Loads and Simulated Fire Behavior in “Old-Stage” Beetle-Infested Ponderosa Pine of the Colorado Plateau. *Forest Science*, 61(4), pp.644–664.
- Heath, J., 2001. *The detection of mountain pine beetle green attacked lodgepole pine*

*using compact airborne spectrographsimager (CASI)*. M.Sc. Thesis, Faculty of Forestry, The University of British Columbia, p. 72.

Hicke, J., Allen, C.D., Desai, A.R., Dietze, M.C., Hall, R.J., Hogg, E.H., Kashian, D.M., Moore, D., Raffa, K.F., Sturrock, R.N. & Vogelmann, J., 2012. Effects of biotic disturbances on forest carbon cycling in the United States and Canada. *Global Change*, 18(1), pp.7–34.

Hicke, J. & Logan, J., 2009. Mapping whitebark pine mortality caused by a mountain pine beetle outbreak with high spatial resolution satellite imagery. *International Journal of Remote Sensing*, 30(17), pp.4427–4441.

Honey-Marie, C., Carroll, A.L., Lindgren, B.S. & Aukema, B.H., 2011. Incoming! Association of landscape features with dispersing mountain pine beetle populations during a range expansion event in western Canada. *Landscape Ecology*, 26(8), pp.1097–1110.

Hubbard, R.M., Rhoades, C.C., Elder, K. & Negron, J., 2013. Changes in transpiration and foliage growth in lodgepole pine trees following mountain pine beetle attack and mechanical girdling. *Forest Ecology and Management*, 289, pp.312–317.

Hunt Jr, E.R. & Rock, B.N., 1989. Detection of changes in leaf water content using Near- and Middle-Infrared reflectances. *Remote Sensing of Environment*, 30(1), pp.43–54.

IBM Corp., 2013. IBM SPSS Statistics for Windows, Version 22.0.

IBM Knowledge Center, 2016a. Testing Homogeneity of Covariance Matrices. Available at:

[http://www.ibm.com/support/knowledgecenter/SSLVMB\\_24.0.0/spss/tutorials/glm\\_m\\_patlos\\_homcov.html](http://www.ibm.com/support/knowledgecenter/SSLVMB_24.0.0/spss/tutorials/glm_m_patlos_homcov.html) [Accessed October 20, 2016].

IBM Knowledge Center, 2016b. Discriminant Analysis Stepwise Method. Available at: [https://www.ibm.com/support/knowledgecenter/SSLVMB\\_20.0.0/com.ibm.spss.statistics.help/idh\\_disc\\_met.htm](https://www.ibm.com/support/knowledgecenter/SSLVMB_20.0.0/com.ibm.spss.statistics.help/idh_disc_met.htm) [Accessed October 20, 2016].

Immitzer, M. & Atzberger, C., 2014. Early Detection of Bark Beetle Infestation in Norway Spruce (*Picea abies*, L.) using WorldView-2 Data. *Photogrammetrie, Fernerkundung, Geoinformation*, 5, pp.351–367.

Immitzer, M., Atzberger, C. & Koukal, T., 2012. Tree species classification with random forest using very high spatial resolution 8-band WorldView-2 satellite data. *Remote Sensing*, 4(9), pp.2661–2693.

Jackman, S., 2015. pscl: Classes and Methods for R Developed in the Political Science Computational Laboratory, R Package v.3.2.4., Stanford University.

Jenkins, M.J., Runyon, J.B., Fettig, C.J., Page, W. G. & Bentz, B.J., 2014. Interactions among the mountain pine beetle, fires, and fuels. *Forest Science*, 60(3), pp.489–501.

Keville, M.P., Reed, S.C. & Cleveland, C.C., 2013. Nitrogen cycling responses to mountain pine beetle disturbance in a high elevation whitebark pine ecosystem. *PLoS ONE*, 8(6), pp.1–8.

Kim, D.M. Zhang, H., Zhou, H., Du, T., Wu, Q., Mockler, T.C. & Berezin, M.Y., 2015. Highly sensitive image-derived indices of water-stressed plants using hyperspectral imaging in SWIR and histogram analysis. *Scientific reports*, 5. Available at:

<http://www.ncbi.nlm.nih.gov/pubmed/26531782> [Accessed October 21, 2016].

Klutsch, J.G., Battaglia, M.A., West, D.R., Costello, S.L. & Negron, J.F., 2011.

Evaluating Potential Fire Behavior in Lodgepole Pine-Dominated Forests after a Mountain Pine Beetle Epidemic in North-Central Colorado. *Western Journal of Applied Forestry*, 26(3), pp.101–109.

Kokaly, R.F. et al., 2007. Characterization of post-fire surface cover, soils, and burn severity at the Cerro Grande Fire, New Mexico, using hyperspectral and multispectral remote sensing. *Remote Sensing of Environment*, 106(3), pp.305–325.

Kokaly, R.F., Asner, G.P., Ollinger, S.V., Martin, M.E. & Wessman, C.A., 2009.

Characterizing canopy biochemistry from imaging spectroscopy and its application to ecosystem studies. *Remote Sensing of Environment*, 113, pp.S78–S91.

Kokaly, R.F., Rockwell, B.W., Haire, S.L. & King, T.V.V., 2001. Investigating a Physical Basis for Spectroscopic Estimates of Leaf Nitrogen Concentration. *Remote Sensing of Environment*, 75(2), pp.153–161.

Kollenkark, J.C., Vanderbilt, V.C., Daughtry, C.S.T. & Bauer, M.E, 1981. Canopy Reflectance as Influenced by Solar Illumination Angle Paper, *LARS Technical Reports*, (1), pp. 4,

Kuhn, M., Wing, J., Weston, S., Williams, A., Keefer, C., Engelhardt, A., Cooper, T., Mayer, Z., Team, R.C., Benesty, M. & Lescarbeau, R., 2016. caret: Classification and Regression Training R package version 6.0-64. Available at:

<https://github.com/topepo/caret/>.

- Lawrence, R.L., Wood, S.D. & Sheley, R.L., 2006. Mapping invasive plants using hyperspectral imagery and Breiman Cutler classifications (randomForest). *Remote Sensing of Environment*, 100(3), pp.356–362.
- Leatherman, D., Aguayo, I. & Mehall, T.M., 2007. *Mountain Pine Beetle: Fact Sheet No. 5.528*, Colorado State University.
- Liaw, A. & Wiener, M., 2002. Classification and Regression by randomForest. *R News*, 2/3, pp.18–22.
- Lin, C., Popescu, S.C., Huang, S.C., Chang, P.T. & Wen, H.L., 2015. A novel reflectance-based model for evaluating chlorophyll concentrations of fresh and water-stressed leaves. *Biogeosciences*, 12(1), pp.49–66.
- Ludlow, W., 1875. *Report of a Reconnaissance of the Black Hills of Dakota, Made in 1874*, U.S. Government Printing Office.
- Menard, S., 2002. *Applied logistic regression analysis*, Sage.
- Miglani, A., Ray, S.S., Vashishta, D.P. & Parihar, J.S., 2011. Comparison of two data smoothing techniques for vegetation spectra derived from EO-1 Hyperion. *Journal of the Indian Society of Remote Sensing*, 39(4), pp.443–453.
- Mikkelsen, K.M., Dickenson, E.R.V, Maxwell, R.M., Mccray, J.E. & Sharp, J.O., 2013a. Water-quality impacts from climate-induced forest die-off. *Nature Climate Change*, 3.
- Mikkelsen, K.M., Maxwell, R.M., Ferguson, I., Stednick, J.D., McCray, J.E. & Sharp,

- J.O., 2013b. Mountain pine beetle infestation impacts: modeling water and energy budgets at the hillslope scale. *Ecohydrology*, 6(1), pp.64-72.
- Murfitt, J., He, Y., Yang, J., Mui, A. & De Mille, K., 2016. Ash decline assessment in emerald ash borer infested natural forests using high spatial resolution images. *Remote Sensing*, 8(3), p.256.
- Murtha, P.A. & Wiart, R.J., 1989. PC-based digital analysis of mountain pine beetle current-attacked and non-attacked lodgepole pine. *Canadian Journal of Remote Sensing*, 15(1), pp.70–79.
- Natural Resources Canada, 2016. Mountain pine beetle (factsheet). Available at: <http://www.nrcan.gc.ca/forests/fire-insects-disturbances/top-insects/13397> [Accessed October 17, 2016].
- Negrón, J.F., Allen, K., Cook, B. & Withrow Jr., J.R., 2008. Susceptibility of ponderosa pine, *Pinus ponderosa* (Dougl. ex Laws.), to mountain pine beetle, *Dendroctonus ponderosae* Hopkins, attack in uneven-aged stands in. *Forest ecology and Management*, 254, pp. 327–334.
- Negrón, J.F. & Popp, J.B., 2004. Probability of ponderosa pine infestation by mountain pine beetle in the Colorado Front Range. *Forest Ecology and Management*, 191(1), pp.17–27.
- Nelson, T.A., Boots, B., Wulder, M.A. & Carroll, A.L., 2007. Environmental characteristics of mountain pine beetle infestation hot spots. *Journal of Ecosystems and Management*, 8(1), pp. 91-108.

- Niemann, K.O., Quinn, G., Stephen, R., Visintini, F. & Parton, D., 2015. Hyperspectral Remote Sensing of Mountain Pine Beetle with an Emphasis on Previsual Assessment. *Canadian Journal of Remote Sensing*, 41(3), pp.191–202.
- NASA Earth Observation, 2016. Cloud Fraction - 1 month - Terra/MODIS. Available at: [http://neo.sci.gsfc.nasa.gov/view.php?datasetId=MODAL2\\_M\\_CLD\\_FR](http://neo.sci.gsfc.nasa.gov/view.php?datasetId=MODAL2_M_CLD_FR) [Accessed October 18, 2016].
- Oumar, Z. & Mutanga, O., 2013. Using WorldView-2 bands and indices to predict bronze bug ( *Thaumastocoris peregrinus* ) damage in plantation forests. *International Journal of Remote Sensing*, 34(6), pp.2236–2249.
- Padwick, C., Deskevich, M., Pacifici, F. & Smallwood, S., 2010. WorldView-2 pan-sharpening. In *ASPRS 2010 Annual Conference*. San Diego.
- Page, W. & Jenkins, M.J., 2007. Predicted fire behavior in selected mountain pine beetle–infested lodgepole pine. *Forest Science*, 53(6), pp.662–674.
- Pal, M., 2005. Random forest classifier for remote sensing classification. *International Journal of Remote Sensing*, 26(1), pp.217–222.
- Peduzzi, P., Concato, J., Kemper, E., Holford, T.R. & Feinstein, A.R., 1996. A simulation study of the number of events per variable in logistic regression analysis. *Journal of Clinical Epidemiology*, 49(12), pp.1373–1379.
- Penuelas, J. Filella, I., Biel, C., Serrano, L. & Save, R., 1993. The reflectance at the 950–970 nm region as an indicator of plant water status. *International Journal of Remote Sensing*, 14(10), pp.1887–1905.

- Pohar, M., Blas, M. & Turk, S., 2004. Comparison of Logistic Regression and Linear Discriminant Analysis: A Simulation Study. *Metodološki zvezki*, 1(1), pp.143–161.
- Prospere, K., McLaren, K. & Wilson, B., 2014. Plant species discrimination in a tropical wetland using in situ hyperspectral data. *Remote sensing*, 6(9), pp. 8494-8523.
- Pu, R. & Liu, D., 2011. Segmented canonical discriminant analysis of *in situ* hyperspectral data for identifying 13 urban tree species. *International Journal of Remote Sensing*, 32(8), pp.2207–2226.
- Raffa, K. & Smalley, E., 1995. Interaction of pre-attack and induced monoterpene concentrations in host conifer defense against bark beetle-fungal complexes. *Oecologia*, 102(3), pp.285–295.
- Raffa, K.F., Aukema, B.H., Bentz, B.J., Carroll, A.L., Hicke, J.A., Turner, M.G. & Roome, W.H., 2008. Cross-scale drivers of natural disturbances prone to anthropogenic amplification: the dynamics of bark beetle eruptions. *Bioscience*, 58(6), pp.501–517.
- Raffa, K.F. & Berryman, A.A., 1983. The role of host plant resistance in the colonization behavior and ecology of bark beetles (Coleoptera: Scolytidae). *Ecological monographs*, 53(1), pp.27–49.
- Rencz, A.N. & Nemeth, J., 1985. Detection of Mountain Pine Beetle Infestation Using Landsat Mss and Simulated Thematic Mapper Data. *Canadian Journal of Remote Sensing*, 11(1), pp.50–58.
- Rodriguez-Galiano, V.F., Ghimire, B., Rogan, J., Chica-Olmo, M. & Rigol-Sanchez, J.P.,

2012. An assessment of the effectiveness of a random forest classifier for land-cover classification. *ISPRS Journal of Photogrammetry and Remote Sensing*, 67, pp.93–104.

Rosenthal, R., 1991. *Meta-analytic procedures for social research* 2nd ed., Newbury Park, CA: Sage.

Saab, V.A., Latif, Q.S., Rowland, M.M., Johnson, T.N., Chalfoun, A.D., Buskirk, S.W., Heyward, J.E. & Dresser, M.A., 2014. Ecological consequences of mountain pine beetle outbreaks for wildlife in Western North American forests. *Forest Science*, 60(3), pp.539–559.

Safranyik, L., 1978. Effects of climate and weather on mountain pine beetle populations. In *Symposium on Theory and Practice of Mountain Pine Beetle Management in Lodgepole Pine Forests, April 25-27, 1978, Washington State University, Pullman, Washington*.

Safranyik, L. & Carroll, A., 2006. The biology and epidemiology of the mountain pine beetle in lodgepole pine forests. In L. Safranyik & B. Wilson, eds. *The Mountain Pine Beetle: A Synthesis of Its Biology, Management and Impacts on Lodgepole Pine*. Victoria, British Columbia: Canadian Forest Service, Pacific Forestry Centre, Natural Resources Canada, pp. 3–66.

Safranyik, L., Shrimpton, D. & Whitney, H., 2002. *Management of Lodgepole Pine to Reduce Losses from the Mountain Pine Beetle: Second Edition*, Natural Resources Canada, Canadian Forest Service, Pacific Forestry Centre.

- Sambaraju, K.R., Carroll, A.L., Zhu, J., Stahl, K., Moore, R.D. & Aukema, B.H., 2012. Climate change could alter the distribution of mountain pine beetle outbreaks in western Canada. *Ecography*, 35(3), pp.211–223.
- Savitzky, A., 1964. Smoothing and differentiation of data by simplified least squares procedures. *Analytical Chemistry*, 36(8), pp.1627–1639.
- Schmid, J. & Mata, S., 2005. *Mountain pine beetle-caused tree mortality in partially cut plots surrounded by unmanaged stands*, USDA Forest Service, Rocky Mountain Research Station, Fort Collins, CO.
- Schmid, J.M. & Mata, S.A., 1992. *Stand density and mountain pine beetle-caused tree mortality in ponderosa pine stands*, USDA Forest Service, Rocky Mountain Forest and Range Experiment Station, Fort Collins, CO.
- Sharma, R., 2007. *Using multispectral and hyperspectral satellite data for the early detection of mountain pine beetle damage*. Ph.D. dissertation, Faculty of Forestry, The University of British Columbia.
- Shepperd, W. & Battaglia, M., 2002. *Ecology, silviculture, and management of Black Hills ponderosa pine*. USDA Forest Service, Rocky Mountain Research Station, General Technical Report RMRS-GTR-97, Fort Collins, CO.
- Sims, C., Aadland, D. & Finnoff, D., 2010. A dynamic bioeconomic analysis of mountain pine beetle epidemics. *Journal of Economic Dynamics and Control*, 34(12), pp.2407-2419.
- Sims, D.A. & Gamon, J.A., 2003. Estimation of vegetation water content and

- photosynthetic tissue area from spectral reflectance: a comparison of indices based on liquid water and chlorophyll absorption features. *Remote Sensing of Environment*, 84(4), pp.526–537.
- Sims, D.A. & Gamon, J.A., 2002. Relationships between leaf pigment content and spectral reflectance across a wide range of species, leaf structures and developmental stages. *Remote Sensing of Environment*, 81(2), pp.337–354.
- Skakun, R.S., Wulder, M.A. & Franklin, S.E., 2003. Sensitivity of the thematic mapper enhanced wetness difference index to detect mountain pine beetle red-attack damage. *Remote Sensing of Environment*, 86(4), pp.433–443.
- Stevens, R., McCambridge, W. & Edminster, C., 1980. *Risk rating guide for mountain pine beetle in Black Hills ponderosa pine*, US Department of Agriculture, Forest Service, Rocky Mountain Forest and Range Experiment Station,, Fort Collins, CO.
- Taylor, S.W., Carroll, A.L., Alfaro, R.I. & Safranyik, L., 2006. Forest, climate and mountain pine beetle outbreak dynamics in western Canada. In L. Safranyik & B. Wilson, eds. *The Mountain Pine Beetle: A Synthesis of Its Biology, Management and Impacts on Lodgepole Pine*. Victoria, British Columbia: Natural Resources Canada, Canadian Forest Service, Pacific Forestry Centre, pp. 67–94.
- Thenkabail, P.S., Enclona, E.A., Ashton, M.S. & Van Der Meer, B., 2004. Accuracy assessments of hyperspectral waveband performance for vegetation analysis applications. *Remote Sensing of Environment*, 91(3), pp.354–376.
- Thompson, B., 1995. Stepwise Regression and Stepwise Discriminant Analysis Need Not

Apply. In *Annual Meeting of the American Educational Research Association*. San Francisco, CA.

Tsai, F. & Philpot, W., 1998. Derivative analysis of hyperspectral data. *Remote Sensing of Environment*, 66(1), pp.41–51.

UCLA Statistical Consulting Group, Regression with SPSS: Chapter 2 - Regression Diagnostics. Available at:

<http://www.ats.ucla.edu/stat/spss/webbooks/reg/chapter2/spsreg2.htm> [Accessed October 20, 2016].

USDA Forest Service, 2010. *Topic: Mountain Pine Beetle in the Black Hills and Control Methods for Single Trees*. Available at:

<http://www.beatthebeetles.com/docs/mpbcontrolmethods4.pdf> [Accessed October 20, 2016].

USDA Forest Service Forest Health Protection, 2016. Forest Health Technology Enterprise Team Mapping and Reporting: Mountain Pine Beetle Summary.

Available at: <http://foresthealth.fs.usda.gov/portal/PestSummary/DamageSummary> [Accessed October 17, 2016].

Ustin, S.L., Gitelson, A.A., Jacquemoud, S., Schaepman, M., Asner, G.P., Gamon, J.A. & Zarco-Tejada, P., 2009. Retrieval of foliar information about plant pigment systems from high resolution spectroscopy. *Remote Sensing of Environment*, 113(1), pp.67–77.

Ustin, S.L., Riaño, D. & Hunt, E.R., 2012. Estimating canopy water content from

- spectroscopy. *Israel Journal of Plant Sciences*, 60(1), pp.9–23.
- Vaiphasa, C., 2006. Consideration of smoothing techniques for hyperspectral remote sensing. *ISPRS Journal of Photogrammetry and Remote*, 60(2), pp.91–99.
- van Aardt, J.A.N. & Wynne, R.H., 2007. Examining pine spectral separability using hyperspectral data from an airborne sensor: An extension of field-based results. *International Journal of Remote Sensing*, 28(2), pp.431–436.
- Venables, W.N. & Ripley, B.D., 2002. *Modern applied statistics with S* 4th ed., New York: Springer.
- Walter, J. & Platt, R., 2013. Multi-temporal analysis reveals that predictors of mountain pine beetle infestation change during outbreak cycles. *Forest Ecology and Management*, 302, pp.308–318.
- Wang, L. & Sousa, W.P., 2009. Distinguishing mangrove species with laboratory measurements of hyperspectral leaf reflectance. *International Journal of Remote Sensing*, 30(5), pp.1267–1281.
- Wang, Z., Skidmore, A.K., Wang, T., Darvishzadeh, R. & Hearne, J., 2015. Applicability of the PROSPECT model for estimating protein and cellulose+lignin in fresh leaves. *Remote Sensing of Environment*, 168, pp.205–218.
- Waser, L., Küchler, M., Jütte, K. & Stampfer, T., 2014. Evaluating the Potential of WorldView-2 Data to Classify Tree Species and Different Levels of Ash Mortality. *Remote Sensing*, 6(5), pp.4515–4545.

- White, J., Wulder, M., Brooks, D., Reich, R. & Wheate, R., 2005. Detection of red attack stage mountain pine beetle infestation with high spatial resolution satellite imagery. *Remote Sensing of Environment*, 96(3), pp.340–351.
- White, J., Wulder, M. & Grills, D., 2006. Detecting and mapping mountain pine beetle red-attack damage with SPOT-5 10-m multispectral imagery. *BC Journal of Ecosystems and Management*, 7(2), pp.105–118.
- White, J.C., Coops, N.C., Hilker, T., Wulder, M.A. & Carroll, A.L., 2007. Detecting mountain pine beetle red attack damage with EO1 Hyperion moisture indices. *International Journal of Remote Sensing*, 28(10), pp.2111–2121.
- Wulder, M.A., White, J.C., Carroll, A.L. & Coops, N.C., 2009. Challenges for the operational detection of mountain pine beetle green attack with remote sensing. *The Forestry Chronicle*, 85(1), pp.32–38.
- Wulder, M.A., Dymond, C.C., White, J.C., Leckie, D.G. & Carroll, A.L., 2006. Surveying mountain pine beetle damage of forests: A review of remote sensing opportunities. *Forest Ecology and Management*, 221(1), pp.27–41.
- Yu, Q. et al., 2006. Object-based Detailed Vegetation Classification with Airborne High Spatial Resolution Remote Sensing Imagery. *Photogrammetric Engineering & Remote Sensing*, 72(7), pp.799–811.
- Zhang, Q., Li, Q. & Zhang, G., 2012. Rapid Determination of Leaf Water Content Using VIS/NIR Spectroscopy Analysis with Wavelength Selection. *Spectroscopy: An International Journal*, 27(2), pp.93–105.

Zygielbaum, A.I., Gitelson, A.A., Arkebauer, T.J. & Rundquist, D.C., 2009. Non-destructive detection of water stress and estimation of relative water content in maize. *Papers in Natural Resources*, 36(12).

Appendix A. Historic winter monthly lows for weather. National Weather Service stations located at Custer, SD (NWS ID CUSS2), Mt. Rushmore National Monument (NWS ID RMNS2), Lead, SD (NWS ID LEAS2), and Pactola Dam (NWS ID RAPS2).

Year	Custer, SD			Mt. Rushmore National Monument			Lead, SD			Pactola Dam, SD		
	Jan.	Feb.	Dec.	Jan.	Feb.	Dec.	Jan.	Feb.	Dec.	Jan.	Feb.	Dec.
2016	3	5	NR	-2	14	NR	-3	14	NR	-8	6	NR
2015	-11	-12	1	-4	-5	3	-6	-5	0	-8	-12	-6
2014	-18	-21	-13	-12	-16	-9	-15	-14	-14	-16	-26	-12
2013	-4	4	-18	-2	4	-18	-4	2	-17	-6	-9	-21
2012	-6	-11	-3	-11	-5	1	-8	-8	-4	-11	-15	-7
2011	-9	-19	-9	-17	-17	0	-18	-24	-4	-17	-21	-7
2010	-19	-9	-4	-10	-2	-2	-13	-7	-9	-17	-15	-5
2009	-10	1	-17	-7	-2	-10	-8	1	-12	-17	-2	-16
2008	-8	NR	-23	-8	-9	-18	-9	-10	-22	-15	-7	-21
2007	-11	-18	2	-14	-9	6	-13	-12	2	-13	-20	-6
2006	9	-26	0	20	-20	5	15	-22	3	10	-30	-5
2005	-8	7	-16	-13	4	-8	-11	8	-12	-13	4	-16
2004	-14	-8	-14	-14	0	-9	-16	-7	-13	-17	-12	-14
2003	-6	-26	2	-7	-17	8	-7	-16	7	-12	-23	0
2002	-3	-10	7	0	-5	10	-1	-10	9	-9	-6	0
2001	0	-17	-5	7	-3	3	5	-10	1	-5	-22	-8
2000	1	9	-16	10	5	-7	5	7	-13	-4	0	-17
1999	-14	9	-2	-3	12	4	-7	9	1	-11	9	1
1998	-10	13	-25	-11	15	-17	-12	11	-18	-13	8	-23
1997	-18	-2	-3	-14	3	10	-20	-6	6	-22	-6	-2
1996	-18	-31	-15	-19	-21	-10	-21	-24	-12	-23	-34	-20
1995	-15	-8	-13	-4	-8	-7	-6	-12	-8	-10	-11	-9
1994	-9	-24	5	-8	-17	2	-11	-19	0	-10	-24	-6
1993	-16	-23	5	-4	-15	10	-8	-14	8	-15	-24	2
1992	-8	9	-9	-4	4	-14	-9	7	-15	-15	2	-15
1991	-15	4	9	-10	14	8	-13	7	7	-20	-1	-2
1990	5	-6	-30	14	-4	-27	7	-7	-29	4	-11	-28
1989	-14	-27	-28	-5	-29	-23	-9	-32	-24	-9	-29	-34
1988	-13	-11	-5	-10	-12	-5	-9	-13	-9	-19	-14	-6
1987	-6	9	-14	0	12	0	-5	10	-4	-6	6	-11
1986	3	-20	-8	0	-9	0	9	-12	-2	7	-21	-4
1985	-19	-21	-10	-15	-15	-12	-23	-15	-15	-18	-23	-24

<b>1984</b>	-24	-1	-12	-15	7	-9	-14	2	-9	-18	-7	-16
<b>1983</b>	NR	NR	-34	10	6	-31	10	5	-33	5	1	-35
<b>1982</b>	-23	-30	NR	-19	-17	3	-22	-20	1	-23	-28	-5
<b>1981</b>	-5	-21	-8	9	-18	-3	8	-23	3	-1	-19	-5
<b>1980</b>	-22	-13	-9	-18	-4	-6	-19	-5	-10	-26	-18	-6
<b>1979</b>	-22	-16	-17	-20	-15	-6	-16	-16	-10	-28	-17	-17
<b>1978</b>	-15	-12	-28	-8	-5	-17	-11	-8	-19	NR	NR	-28
<b>1977</b>	-17	10	-25	-14	11	-17	-14	14	-20	NR	4	NR
<b>1976</b>	-20	-22	-10	-16	-8	-10	-13	-9	-12	-21	-21	NR
<b>1975</b>	-14	-16	-12	-12	-11	-6	-17	-12	-2	-13	-15	-8
<b>1974</b>	-24	-8	-4	-17	-1	0	-21	-3	-5	-28	-11	-9
<b>1973</b>	-23	-8	-8	-15	0	-8	-16	0	-12	-24	-8	4
<b>1972</b>	-26	-12	-27	-23	-4	-20	-23	-12	-22	-24	-14	-27
<b>1971</b>	-22	-20	-6	-12	-14	-4	-11	-15	-7	-15	-23	-6
<b>1970</b>	-24	-2	-16	-14	-1	-6	-14	-1	-3	-20	-4	-12
<b>1969</b>	-11	-5	-18	-14	10	7	-15	7	5	-17	-1	-7
<b>1968</b>	-26	-7	-22	-20	0	-25	-20	-6	-27	-25	-7	-26
<b>1967</b>	-9	-11	-16	-10	-2	-15	-10	-2	-12	-12	-9	-23
<b>1966</b>	-27	-15	-15	-15	-8	0	-14	-3	-2	-22	-12	-6
<b>1965</b>	NR	-16	-9	0	-13	0	3	-20	1	-3	-20	-3
<b>1964</b>	-26	-2	-37	-1	3	-24	-3	-1	-25	-18	-7	-24
<b>1963</b>	-43	-15	-15	-38	-8	-7	-25	-5	-11	-34	-15	-18
<b>1962</b>	-32	-34	-22	NR	-15	-2	-18	-15	-3	-27	-23	-7
<b>1961</b>	-12	-3	-21	NR	NR	NR	-6	9	-12	-13	2	-21
<b>1960</b>	-20	-28	-19	NR	NR	NR	-4	-12	-1	-12	-24	-9
<b>1959</b>	-31	-15	1	NR	NR	NR	-20	-2	11	-26	-10	2
<b>1958</b>	-8	-19	-15	NR	NR	NR	12	-7	-10	-2	-17	-16
<b>1957</b>	-30	-17	-9	NR	NR	NR	-19	-14	10	-27	-18	2
<b>1956</b>	-9	-22	-15	NR	NR	NR	-6	-14	-12	-12	-18	-13
<b>1955</b>	-11	-22	-11	NR	NR	NR	-5	-15	-10	NR	NR	NR
<b>1954</b>	-18	2	-18	NR	NR	NR	-19	7	6	NR	NR	NR
<b>1953</b>	NR	-5	-4	NR	NR	NR	-11	-2	-3	NR	NR	NR
<b>1952</b>	-24	-8	-7	NR	NR	NR	-19	3	8	NR	NR	NR
<b>1951</b>	-36	-24	-25	NR	NR	NR	-23	-14	-20	NR	NR	NR
<b>1950</b>	-24	-14	-18	NR	NR	NR	-27	-6	-10	NR	NR	NR
<b>1949</b>	NR	-17	-8	NR	NR	NR	-21	-19	-11	NR	NR	NR
<b>1948</b>	-26	-24	-8	NR	NR	NR	-12	-15	2	NR	NR	NR
<b>1947</b>	-22	-16	-6	NR	NR	NR	-7	NR	-1	NR	NR	NR

1946	-20	-5	-24	NR	NR	NR	-8	3	-13	NR	NR	NR
1945	-16	-9	-25	NR	NR	NR	1	-3	-10	NR	NR	NR
1944	-16	-27	-26	NR	NR	NR	7	-9	-9	NR	NR	NR
1943	-31	-1	-7	NR	NR	NR	-30	-8	0	NR	NR	NR
1942	NR	NR	NR	NR	NR	NR	-18	-19	-1	NR	NR	NR
1941	NR	NR	NR	NR	NR	NR	-4	3	-11	NR	NR	NR
1940	NR	NR	NR	NR	NR	NR	-25	0	-2	NR	NR	NR
1939	NR	NR	NR	NR	NR	NR	0	-26	7	NR	NR	NR
1938	NR	NR	NR	NR	NR	NR	-19	-11	-8	NR	NR	NR
1937	NR	NR	NR	NR	NR	NR	-21	-7	-13	NR	NR	NR
1936	NR	NR	NR	NR	NR	NR	-7	-40	-14	NR	NR	NR
1935	NR	NR	NR	NR	NR	NR	-32	-8	-12	NR	NR	NR
1934	NR	NR	NR	NR	NR	NR	5	-13	-16	NR	NR	NR
1933	NR	NR	NR	NR	NR	NR	-10	-34	-16	NR	NR	NR
1932	NR	NR	NR	NR	NR	NR	-18	-10	-25	NR	NR	NR
1931	NR	NR	NR	NR	NR	NR	-5	14	6	NR	NR	NR
1930	NR	NR	NR	NR	NR	NR	-32	1	15	NR	NR	NR
1929	NR	NR	NR	NR	NR	NR	-18	-15	-9	NR	NR	NR
1928	NR	NR	NR	NR	NR	NR	-25	-12	-2	NR	NR	NR
1927	NR	NR	NR	NR	NR	NR	-22	-12	-27	NR	NR	NR
1926	NR	NR	NR	NR	NR	NR	-4	5	-22	NR	NR	NR
1925	NR	NR	NR	NR	NR	NR	-5	0	-16	NR	NR	NR
1924	NR	NR	NR	NR	NR	NR	-19	-12	-29	NR	NR	NR
1923	NR	NR	NR	NR	NR	NR	0	-25	-25	NR	NR	NR
1922	NR	NR	NR	NR	NR	NR	-19	-20	-14	NR	NR	NR
1921	NR	NR	NR	NR	NR	NR	2	-1	-14	NR	NR	NR
1920	NR	NR	NR	NR	NR	NR	-15	-2	-9	NR	NR	NR
1919	NR	NR	NR	NR	NR	NR	-19	-20	-29	NR	NR	NR
1918	NR	NR	NR	NR	NR	NR	-30	-24	-16	NR	NR	NR
1917	NR	NR	NR	NR	NR	NR	-25	-29	-27	NR	NR	NR
1916	NR	NR	NR	NR	NR	NR	-29	-12	-22	NR	NR	NR
1915	NR	NR	NR	NR	NR	NR	-18	3	-10	NR	NR	NR
1914	NR	NR	NR	NR	NR	NR	2	-29	-11	NR	NR	NR
1913	NR	NR	NR	NR	NR	NR	-23	-19	2	NR	NR	NR
1912	NR	NR	NR	NR	NR	NR	-22	-20	3	NR	NR	NR
1911	NR	NR	NR	NR	NR	NR	-25	-4	-21	NR	NR	NR
1910	NR	NR	NR	NR	NR	NR	-13	-26	10	NR	NR	NR

Appendix B. Shapiro-Wilk test of normality for each WV-2 spectral variable.

WV-2 Variable	Group	Shapiro-Wilk Test		
		Statistic	df	Sig.
<b>Coastal</b>	NA	0.945	414	0.000
	GA	0.892	291	0.000
<b>Blue</b>	NA	0.933	414	0.000
	GA	0.908	291	0.000
<b>Green</b>	NA	0.984	414	0.000
	GA	0.942	291	0.000
<b>Yellow</b>	NA	0.953	414	0.000
	GA	0.957	291	0.000
<b>Red</b>	NA	0.95	414	0.000
	GA	0.94	291	0.000
<b>Red - Edge</b>	NA	0.979	414	0.000
	GA	0.994	291	0.248
<b>NIR1</b>	NA	0.983	414	0.000
	GA	0.991	291	0.086
<b>NIR2</b>	NA	0.985	414	0.000
	GA	0.986	291	0.006
<b>Coastal-Blue</b>	NA	0.997	414	0.573
	GA	0.985	291	0.005
<b>Coastal -Green</b>	NA	0.951	414	0.000
	GA	0.99	291	0.039
<b>Coastal/Yellow</b>	NA	0.986	414	0.001
	GA	0.983	291	0.001
<b>Coastal/Red</b>	NA	0.993	414	0.038
	GA	0.975	291	0.000
<b>Coastal/Red Edge</b>	NA	0.962	414	0.000
	GA	0.954	291	0.000
<b>Coastal/NIR 1</b>	NA	0.953	414	0.000
	GA	0.94	291	0.000
<b>Coastal/NIR 2</b>	NA	0.952	414	0.000
	GA	0.949	291	0.000
<b>Blue/Green</b>	NA	0.988	414	0.002
	GA	0.996	291	0.628
<b>Blue/Yellow</b>	NA	0.96	414	0.000
	GA	0.977	291	0.000
<b>Blue/Red</b>	NA	0.994	414	0.109

	GA	0.988	291	0.019
<b>Blue/Red Edge</b>	NA	0.941	414	0.000
	GA	0.974	291	0.000
<b>Blue/NIR 1</b>	NA	0.951	414	0.000
	GA	0.956	291	0.000
<b>Blue/NIR 2</b>	NA	0.939	414	0.000
	GA	0.959	291	0.000
<b>Green/Yellow</b>	NA	0.989	414	0.004
	GA	0.995	291	0.397
<b>Green/Red</b>	NA	0.988	414	0.002
	GA	0.962	291	0.000
<b>Green/Red Edge</b>	NA	0.988	414	0.002
	GA	0.962	291	0.000
<b>Green/NIR 1</b>	NA	0.981	414	0.000
	GA	0.978	291	0.000
<b>Green/NIR 2</b>	NA	0.99	414	0.005
	GA	0.971	291	0.000
<b>Yellow/Red</b>	NA	0.995	414	0.162
	GA	0.996	291	0.588
<b>Yellow/Red Edge</b>	NA	0.96	414	0.000
	GA	0.977	291	0.000
<b>Yellow/NIR 1</b>	NA	0.97	414	0.000
	GA	0.974	291	0.000
<b>Yellow/NIR 2</b>	NA	0.938	414	0.000
	GA	0.987	291	0.009
<b>Red/Red Edge</b>	NA	0.946	414	0.000
	GA	0.982	291	0.001
<b>Red/NIR 1</b>	NA	0.952	414	0.000
	GA	0.981	291	0.001
<b>Red/NIR 2</b>	NA	0.958	414	0.000
	GA	0.975	291	0.000
<b>Red Edge/NIR 1</b>	NA	0.763	414	0.000
	GA	0.978	291	0.000
<b>Red Edge/NIR 2</b>	NA	0.975	414	0.000
	GA	0.985	291	0.004
<b>NIR 1/NIR 2</b>	NA	0.976	414	0.000
	GA	0.989	291	0.026

Appendix C. Correlation coefficients between all 36 WV-2 spectral variables.

	<b>Coastal</b>	<b>Blue</b>	<b>Green</b>	<b>Yellow</b>	<b>Red</b>	<b>Red Edge</b>	<b>NIR 1</b>	<b>NIR 2</b>
<b>Coastal</b>	1.000	0.360	0.824	0.385	0.361	0.227	0.112	0.173
<b>Blue</b>	0.360	1.000	0.368	0.669	0.289	0.285	0.160	0.057
<b>Green</b>	0.824	0.368	1.000	0.362	0.347	0.222	0.163	0.367
<b>Yellow</b>	0.385	0.669	0.362	1.000	0.302	0.393	0.232	0.071
<b>Red</b>	0.361	0.289	0.347	0.302	1.000	0.171	0.092	0.097
<b>Red Edge</b>	0.227	0.285	0.222	0.393	0.171	1.000	0.824	0.223
<b>NIR 1</b>	0.112	0.160	0.163	0.232	0.092	0.824	1.000	0.302
<b>NIR 2</b>	0.173	0.057	0.367	0.071	0.097	0.223	0.302	1.000
<b>Coastal-Blue</b>	0.691	0.358	0.503	0.124	0.101	0.006	0.021	0.127
<b>Coastal-Green</b>	0.715	0.169	0.250	0.212	0.179	0.147	0.038	0.077
<b>Coastal-Yellow</b>	0.763	0.050	0.584	0.238	0.147	0.032	0.037	0.141
<b>Coastal-Red</b>	0.743	0.157	0.571	0.165	0.303	0.091	0.057	0.124
<b>Coastal-Red Edge</b>	0.856	0.207	0.687	0.172	0.248	0.253	0.264	0.087
<b>Coastal-NIR 1</b>	0.881	0.250	0.695	0.238	0.288	0.153	0.318	0.056
<b>Coastal-NIR 2</b>	0.898	0.318	0.635	0.342	0.304	0.136	0.004	0.229
<b>Blue-Green</b>	0.280	0.630	0.441	0.348	0.019	0.123	0.045	0.249
<b>Blue-Yellow</b>	0.071	0.575	0.100	0.183	0.068	0.040	0.024	0.015
<b>Blue-Red</b>	0.057	0.644	0.074	0.356	0.497	0.120	0.090	0.017
<b>Blue-Red Edge</b>	0.205	0.787	0.219	0.407	0.180	0.328	0.318	0.058
<b>Blue-NIR 1</b>	0.263	0.824	0.243	0.483	0.225	0.194	0.389	0.097
<b>Blue-NIR 2</b>	0.213	0.843	0.116	0.559	0.207	0.153	0.013	0.451
<b>Green-Yellow</b>	0.366	0.234	0.564	0.529	0.032	0.166	0.069	0.280
<b>Green-Red</b>	0.359	0.058	0.538	0.031	0.575	0.011	0.054	0.236
<b>Green-Red Edge</b>	0.359	0.058	0.538	0.031	0.575	0.011	0.054	0.236
<b>Green-NIR 1</b>	0.621	0.193	0.750	0.141	0.231	0.358	0.499	0.163

<b>Green-NIR 2</b>	0.704	0.331	0.761	0.319	0.278	0.080	0.019	0.296
<b>Yellow-Red</b>	0.011	0.281	0.004	0.537	0.607	0.167	0.119	0.030
<b>Yellow-Red Edge</b>	0.190	0.430	0.177	0.681	0.166	0.373	0.381	0.083
<b>Yellow-NIR 1</b>	0.252	0.473	0.201	0.731	0.207	0.210	0.461	0.130
<b>Yellow-NIR 2</b>	0.190	0.502	0.050	0.779	0.183	0.205	0.031	0.539
<b>Red-Red Edge</b>	0.147	0.062	0.142	0.007	0.756	0.484	0.440	0.042
<b>Red-NIR 1</b>	0.211	0.124	0.170	0.094	0.776	0.361	0.524	0.088
<b>Red-NIR 2</b>	0.186	0.205	0.055	0.219	0.796	0.031	0.085	0.492
<b>Red Edge-NIR 1</b>	0.173	0.174	0.079	0.244	0.122	0.308	0.270	0.131
<b>Red Edge-NIR 2</b>	0.034	0.169	0.123	0.255	0.050	0.640	0.438	0.586
<b>NIR 1-NIR 2</b>	0.049	0.096	0.165	0.151	0.006	0.537	0.613	0.550

	<b>Coastal-Blue</b>	<b>Coastal-Green</b>	<b>Coastal-Yellow</b>	<b>Coastal-Red</b>	<b>Coastal-Red Edge</b>	<b>Coastal-NIR 1</b>	<b>Coastal-NIR 2</b>	<b>Blue-Green</b>
<b>Coastal</b>	0.691	0.715	0.763	0.743	0.856	0.881	0.898	0.280
<b>Blue</b>	0.358	0.169	0.050	0.157	0.207	0.250	0.318	0.630
<b>Green</b>	0.503	0.250	0.584	0.571	0.687	0.695	0.635	0.441
<b>Yellow</b>	0.124	0.212	0.238	0.165	0.172	0.238	0.342	0.348
<b>Red</b>	0.101	0.179	0.147	0.303	0.248	0.288	0.304	0.019
<b>Red Edge</b>	0.006	0.147	0.032	0.091	0.253	0.153	0.136	0.123
<b>NIR 1</b>	0.021	0.038	0.037	0.057	0.264	0.318	0.004	0.045
<b>NIR 2</b>	0.127	0.077	0.141	0.124	0.087	0.056	0.229	0.249
<b>Coastal-Blue</b>	1.000	0.647	0.838	0.666	0.715	0.695	0.654	0.746
<b>Coastal-Green</b>	0.647	1.000	0.677	0.656	0.676	0.691	0.783	0.015
<b>Coastal-Yellow</b>	0.838	0.677	1.000	0.711	0.803	0.770	0.717	0.506
<b>Coastal-Red</b>	0.666	0.656	0.711	1.000	0.723	0.701	0.703	0.298
<b>Coastal-</b>	0.715	0.676	0.803	0.723	1.000	0.959	0.818	0.342

<b>Red Edge</b>								
<b>Coastal-NIR 1</b>	0.695	0.691	0.770	0.701	0.959	1.000	0.847	0.303
<b>Coastal-NIR 2</b>	0.654	0.783	0.717	0.703	0.818	0.847	1.000	0.175
<b>Blue-Green</b>	0.746	0.015	0.506	0.298	0.342	0.303	0.175	1.000
<b>Blue-Yellow</b>	0.349	0.012	0.212	0.036	0.099	0.078	0.060	0.477
<b>Blue-Red</b>	0.407	0.020	0.152	0.402	0.008	0.006	0.060	0.562
<b>Blue-Red Edge</b>	0.361	0.082	0.032	0.099	0.372	0.336	0.218	0.563
<b>Blue-NIR 1</b>	0.333	0.140	0.031	0.108	0.349	0.415	0.286	0.577
<b>Blue-NIR 2</b>	0.405	0.194	0.136	0.064	0.121	0.172	0.395	0.718
<b>Green-Yellow</b>	0.545	0.000	0.728	0.359	0.456	0.398	0.244	0.716
<b>Green-Red</b>	0.331	0.024	0.364	0.761	0.366	0.326	0.254	0.410
<b>Green-Red Edge</b>	0.331	0.024	0.364	0.761	0.366	0.326	0.254	0.410
<b>Green-NIR 1</b>	0.468	0.188	0.545	0.461	0.788	0.822	0.528	0.442
<b>Green-NIR 2</b>	0.433	0.302	0.503	0.505	0.639	0.662	0.811	0.298
<b>Yellow-Red</b>	0.189	0.018	0.330	0.420	0.067	0.052	0.022	0.267
<b>Yellow-Red Edge</b>	0.129	0.095	0.236	0.085	0.370	0.347	0.216	0.261
<b>Yellow-NIR 1</b>	0.103	0.161	0.212	0.099	0.337	0.433	0.290	0.285
<b>Yellow-NIR 2</b>	0.196	0.223	0.311	0.048	0.064	0.138	0.412	0.460
<b>Red-Red Edge</b>	0.088	0.059	0.141	0.349	0.377	0.343	0.157	0.061
<b>Red-NIR 1</b>	0.100	0.126	0.144	0.314	0.369	0.433	0.233	0.018
<b>Red-NIR 2</b>	0.004	0.207	0.028	0.358	0.141	0.194	0.388	0.178
<b>Red Edge-NIR 1</b>	0.031	0.175	0.001	0.044	0.013	0.259	0.207	0.115

<b>Red Edge-NIR 2</b>	0.111	0.176	0.150	0.029	0.302	0.191	0.280	0.299
<b>NIR 1-NIR 2</b>	0.135	0.098	0.160	0.053	0.320	0.338	0.191	0.260

	<b>Green-NIR 1</b>	<b>Green-NIR 2</b>	<b>Yellow-Red</b>	<b>Yellow-Red Edge</b>	<b>Yellow-NIR 1</b>	<b>Yellow-NIR 2</b>
<b>Coastal</b>	0.621	0.704	0.011	0.190	0.252	0.190
<b>Blue</b>	0.193	0.331	0.281	0.430	0.473	0.502
<b>Green</b>	0.750	0.761	0.004	0.177	0.201	0.050
<b>Yellow</b>	0.141	0.319	0.537	0.681	0.731	0.779
<b>Red</b>	0.231	0.278	0.607	0.166	0.207	0.183
<b>Red Edge</b>	0.358	0.080	0.167	0.373	0.210	0.205
<b>NIR 1</b>	0.499	0.019	0.119	0.381	0.461	0.031
<b>NIR 2</b>	0.163	0.296	0.030	0.083	0.130	0.539
<b>Coastal-Blue</b>	0.468	0.433	0.189	0.129	0.103	0.196
<b>Coastal-Green</b>	0.188	0.302	0.018	0.095	0.161	0.223
<b>Coastal-Yellow</b>	0.545	0.503	0.330	0.236	0.212	0.311
<b>Coastal-Red</b>	0.461	0.505	0.420	0.085	0.099	0.048
<b>Coastal-Red Edge</b>	0.788	0.639	0.067	0.370	0.337	0.064
<b>Coastal-NIR 1</b>	0.822	0.662	0.052	0.347	0.433	0.138
<b>Coastal-NIR 2</b>	0.528	0.811	0.022	0.216	0.290	0.412
<b>Blue-Green</b>	0.442	0.298	0.267	0.261	0.285	0.460
<b>Blue-Yellow</b>	0.097	0.089	0.221	0.173	0.176	0.181
<b>Blue-Red</b>	0.010	0.088	0.747	0.262	0.252	0.307
<b>Blue-Red Edge</b>	0.401	0.258	0.178	0.672	0.590	0.358
<b>Blue-NIR 1</b>	0.460	0.304	0.193	0.629	0.707	0.444
<b>Blue-NIR 2</b>	0.055	0.433	0.275	0.425	0.481	0.747
<b>Green-Yellow</b>	0.562	0.401	0.470	0.426	0.455	0.646
<b>Green-Red</b>	0.443	0.404	0.549	0.013	0.020	0.138
<b>Green-Red Edge</b>	0.443	0.404	0.549	0.013	0.020	0.138
<b>Green-NIR 1</b>	1.000	0.652	0.088	0.410	0.471	0.017

<b>Green-NIR 2</b>	0.652	1.000	0.028	0.233	0.283	0.427
<b>Yellow-Red</b>	0.088	0.028	1.000	0.422	0.415	0.481
<b>Yellow-Red Edge</b>	0.410	0.233	0.422	1.000	0.903	0.614
<b>Yellow-NIR 1</b>	0.471	0.283	0.415	0.903	1.000	0.684
<b>Yellow-NIR 2</b>	0.017	0.427	0.481	0.614	0.684	1.000
<b>Red-Red Edge</b>	0.432	0.167	0.661	0.396	0.321	0.016
<b>Red-NIR 1</b>	0.500	0.220	0.610	0.374	0.457	0.117
<b>Red-NIR 2</b>	0.075	0.395	0.517	0.186	0.254	0.492
<b>Red Edge-NIR 1</b>	0.212	0.150	0.073	0.028	0.401	0.283
<b>Red Edge-NIR 2</b>	0.447	0.283	0.168	0.260	0.083	0.596
<b>NIR 1-NIR 2</b>	0.587	0.224	0.143	0.271	0.296	0.487

	<b>Red-Red Edge</b>	<b>Red-NIR 1</b>	<b>Red-NIR 2</b>	<b>Red Edge-NIR 1</b>	<b>Red Edge-NIR 2</b>	<b>NIR 1-NIR 2</b>
<b>Coastal</b>	0.147	0.211	0.186	0.173	0.034	0.049
<b>Blue</b>	0.062	0.124	0.205	0.174	0.169	0.096
<b>Green</b>	0.142	0.170	0.055	0.079	0.123	0.165
<b>Yellow</b>	0.007	0.094	0.219	0.244	0.255	0.151
<b>Red</b>	0.756	0.776	0.796	0.122	0.050	0.006
<b>Red Edge</b>	0.484	0.361	0.031	0.308	0.640	0.537
<b>NIR 1</b>	0.440	0.524	0.085	0.270	0.438	0.613
<b>NIR 2</b>	0.042	0.088	0.492	0.131	0.586	0.550
<b>Coastal-Blue</b>	0.088	0.100	0.004	0.031	0.111	0.135
<b>Coastal-Green</b>	0.059	0.126	0.207	0.175	0.176	0.098
<b>Coastal-Yellow</b>	0.141	0.144	0.028	0.001	0.150	0.160
<b>Coastal-Red</b>	0.349	0.314	0.358	0.044	0.029	0.053
<b>Coastal-Red Edge</b>	0.377	0.369	0.141	0.013	0.302	0.320
<b>Coastal-NIR 1</b>	0.343	0.433	0.194	0.259	0.191	0.338
<b>Coastal-NIR 2</b>	0.157	0.233	0.388	0.207	0.280	0.191
<b>Blue-Green</b>	0.061	0.018	0.178	0.115	0.299	0.260
<b>Blue-Yellow</b>	0.078	0.062	0.038	0.051	0.056	0.032

<b>Blue-Red</b>	0.537	0.505	0.438	0.027	0.110	0.105
<b>Blue-Red Edge</b>	0.372	0.340	0.175	0.067	0.248	0.236
<b>Blue-NIR 1</b>	0.321	0.422	0.240	0.295	0.103	0.262
<b>Blue-NIR 2</b>	0.068	0.144	0.450	0.210	0.475	0.396
<b>Green-Yellow</b>	0.128	0.068	0.162	0.165	0.367	0.307
<b>Green-Red</b>	0.539	0.545	0.671	0.082	0.182	0.150
<b>Green-Red Edge</b>	0.539	0.545	0.671	0.082	0.182	0.150
<b>Green-NIR 1</b>	0.432	0.500	0.075	0.212	0.447	0.587
<b>Green-NIR 2</b>	0.167	0.220	0.395	0.150	0.283	0.224
<b>Yellow-Red</b>	0.661	0.610	0.517	0.073	0.168	0.143
<b>Yellow-Red Edge</b>	0.396	0.374	0.186	0.028	0.260	0.271
<b>Yellow-NIR 1</b>	0.321	0.457	0.254	0.401	0.083	0.296
<b>Yellow-NIR 2</b>	0.016	0.117	0.492	0.283	0.596	0.487
<b>Red-Red Edge</b>	1.000	0.932	0.677	0.098	0.387	0.370
<b>Red-NIR 1</b>	0.932	1.000	0.725	0.263	0.246	0.400
<b>Red-NIR 2</b>	0.677	0.725	1.000	0.192	0.408	0.333
<b>Red Edge-NIR 1</b>	0.098	0.263	0.192	1.000	0.364	0.112
<b>Red Edge-NIR 2</b>	0.387	0.246	0.408	0.364	1.000	0.884
<b>NIR 1-NIR 2</b>	0.370	0.400	0.333	0.112	0.884	1.000

Appendix D. Cross-Validated classification accuracies for each classifier and predictor variable grouping.

<b>Variable Grouping</b>	<b>Classifier</b>	<b>Overall Accuracy (%)</b>	<b>Kappa</b>	<b>GA User's Accuracy (%)</b>	<b>NA User's Accuracy (%)</b>	<b>GA Producer's Accuracy (%)</b>	<b>NA Producer's Accuracy (%)</b>
Grouping 1	LR	75.96	0.494	74.25	76.9	63.92	84.42
	LDA	68.94	0.3462	55.67	78.26	64.29	78.26
	RF	73.19	0.434	59.79	82.61	70.73	74.51
Grouping 2	LR	69.79	0.353	67.81	70.68	51.03	82.97
	LDA	67.45	0.3001	46.91	81.88	64.54	68.69
	RF	72.13	0.412	58.76	81.52	69.09	73.77
Grouping 3	LR	72.34	0.416	69.51	73.86	58.76	81.88
	LDA	69.57	0.35	51.55	82.25	67.11	70.72
	RF	70	0.3681	56.7	79.35	65.87	72.28
Grouping 4	LR	69.15	0.345	65.61	70.93	53.09	80.43
	LDA	67.45	0.3056	49.48	80.07	63.58	69.28
	RF	65.32	0.2695	51.03	75.36	59.28	68.65
Grouping 5	LR	72.34	0.4095	71.33	72.81	55.15	84.42
	LDA	71.28	0.3824	51.55	85.14	70.92	71.43
	RF	72.13	0.4138	59.79	80.8	68.64	74.09

Appendix E. Classification accuracies tested using an independent dataset for each classifier and predictor variable grouping.

<b>Variable Grouping</b>	<b>Classifier</b>	<b>Overall Accuracy (%)</b>	<b>Kappa</b>	<b>GA User's Accuracy (%)</b>	<b>NA User's Accuracy (%)</b>	<b>GA Producer's Accuracy (%)</b>	<b>NA Producer's Accuracy (%)</b>
Grouping 1	LR	69.79	0.3601	66.25	71.61	54.64	80.43
	LDA	69.36	0.3439	50.52	82.61	67.12	70.37
	RF	68.51	0.3464	59.79	74.64	62.37	72.54
Grouping 2	LR	66.38	0.2766	62.86	67.88	45.36	81.16
	LDA	67.76	0.2985	44.33	84.06	66.15	68.24
	RF	70.64	0.3859	59.79	78.26	65.91	73.47
Grouping 3	LR	67.23	0.3125	61.63	70.47	54.64	76.09
	LDA	67.66	0.3118	50.52	79.71	63.64	69.62
	RF	65.53	0.2654	47.42	78.26	60.53	67.92
Grouping 4	LR	64.68	0.2472	59.21	67.3	46.39	77.54
	LDA	63.83	0.2266	44.33	77.54	58.11	66.46
	RF	65.96	0.2756	48.45	78.26	61.04	68.35
Grouping 5	LR	66.81	0.2915	62.67	68.75	48.45	62.67
	LDA	67.23	0.295	46.39	81.88	64.29	68.48
	RF	70.21	0.376	58.76	78.26	65.52	72.97